

Southern Methodist University

SMU Scholar

---

Civil and Environmental Engineering Theses and  
Dissertations

Civil Engineering and Environmental  
Engineering

---

Summer 8-4-2020

## A Modeling Framework for Urban Growth Prediction using Remote Sensing and Video Prediction Technologies: A Time-Dependent Convolutional Encoder-Decoder Architecture

Ahmed Hassan Jaad

*Southern Methodist University*, [ajaad@smu.edu](mailto:ajaad@smu.edu)

Follow this and additional works at: [https://scholar.smu.edu/engineering\\_civil\\_etds](https://scholar.smu.edu/engineering_civil_etds)



Part of the [Artificial Intelligence and Robotics Commons](#), [Other Architecture Commons](#), [Other Civil and Environmental Engineering Commons](#), [Remote Sensing Commons](#), [Urban, Community and Regional Planning Commons](#), [Urban Studies Commons](#), and the [Urban Studies and Planning Commons](#)

---

### Recommended Citation

Jaad, Ahmed Hassan, "A Modeling Framework for Urban Growth Prediction using Remote Sensing and Video Prediction Technologies: A Time-Dependent Convolutional Encoder-Decoder Architecture" (2020). *Civil and Environmental Engineering Theses and Dissertations*. 12.  
[https://scholar.smu.edu/engineering\\_civil\\_etds/12](https://scholar.smu.edu/engineering_civil_etds/12)

This Dissertation is brought to you for free and open access by the Civil Engineering and Environmental Engineering at SMU Scholar. It has been accepted for inclusion in Civil and Environmental Engineering Theses and Dissertations by an authorized administrator of SMU Scholar. For more information, please visit <http://digitalrepository.smu.edu>.

A MODELING FRAMEWORK FOR URBAN GROWTH PREDICTION USING  
REMOTE SENSING AND VIDEO PREDICTION TECHNOLOGIES: A TIME-  
DEPENDENT CONVOLUTIONAL ENCODER-DECODER ARCHITECTURE

Dissertation Committee:

Dr. Khaled Abdelghany (Advisor)

Dr. Barbara Minsker

Dr. Brett Story

Dr. Janille Smith-Colin

Dr. Mohammad Khodayar

A MODELING FRAMEWORK FOR URBAN GROWTH PREDICTION USING  
REMOTE SENSING AND VIDEO PREDICTION TECHNOLOGIES: A TIME-  
DEPENDENT CONVOLUTIONAL ENCODER-DECODER ARCHITECTURE

A Dissertation Presented to the Graduate Faculty of

Lyle School of Engineering

Southern Methodist University

in

Partial Fulfillment of the Requirements

for the degree of

Doctor of Philosophy

with a

Major in Civil and Environmental Engineering

by

Ahmed Jaad

B.Sc., Umm Al-Qura University, Mecca, Saudi Arabia, 2007

M.Sc., Vanderbilt University, Nashville, Tennessee, 2011

August 4, 2020

Copyright (2020)

Ahmed Jaad

All Rights Reserved

## ACKNOWLEDGMENTS

First and foremost, my deepest thanks and gratitude goes to God for providing me the opportunity and perseverance to complete my Ph.D. journey. I would like to express my sincere gratitude to my supervisor, Professor Khaled Abdelghany for his guidance, encouragement, advice, and invaluable help. I am most grateful for his open-door policy and willingness to make himself available to me whenever I needed assistance. I also appreciate the valuable comments and suggestions of my advisory committee members, Professor Barbara Minsker, Professor Brett Story and Professor Janille Smith-Colin, and Professor Mohammad Khodayar.

I am greatly indebted to my parents who show patience and support during my study. Also, my sincerest appreciation goes to my wife Reem Mahrous, and to my lovely daughters Jumana and Juwana for their patience, love, and faith in my ability.

Jaad, Ahmed

B.Sc., Umm Al-Qura University, Mecca, Saudi Arabia, 2007  
M.Sc., Vanderbilt University, Nashville, Tennessee, 2011

A Modeling Framework for Urban Growth Prediction using Remote Sensing and Video Prediction Technologies: A Time-Dependent Convolutional Encoder-Decoder Architecture

Advisor: Professor Khaled Abdelghany

Doctor of Philosophy conferred August 4, 2020

Dissertation completed May 20, 2020

Studying the growth pattern of cities/urban areas has received considerable attention during the past few decades. The goal is to identify directions and locations of potential growth, assess infrastructure and public service requirements, and ensure the integration of the new developments with the existing city structure. This dissertation presents a novel model for urban growth prediction using a novel machine learning model. The model treats successive historical satellite images of the urban area under consideration as a video for which future frames are predicted. A time-dependent convolutional encoder-decoder architecture is adopted. The model considers as an input a satellite image for the base year and the prediction horizon. It constructs an image that predicts the growth of the urban area for any given target year within the specified horizon. A sensitivity analysis is performed to determine the best combination of parameters to obtain the highest prediction performance. As a case study, the model is used to predict the urban growth pattern for the Dallas-Fort Worth (DFW) area in Texas, with focus on two of its counties that observed significant growth over the past decade. In addition, the model is applied to predict the growth pattern of five cities in the Middle East and North Africa

(MENA) region. These cities vary in terms of their size, population, historical heritage, level of control applied to their growth, geographical locations, complexity of their structure, and socio-economic characteristics. The model is shown to produce results that are consistent with other growth prediction studies conducted for these cities.

## TABLE OF CONTENTS

TABLE OF CONTENTS .....	vii
LIST OF TABLES .....	xii
LIST OF FIGURES .....	xiv
Chapter 1 .....	1
INTRODUCTION .....	1
1-1. Background .....	1
1-2. Main Theories for Studying Urban Growth.....	1
1-3. Challenges of Developing Urban Growth Prediction Models .....	2
1-4. Emerging Technologies for Developing Urban Growth Prediction Models .....	3
1-5. Research Approach .....	4
1-6. Research Contributions .....	6
1-7. Dissertation Organization .....	6
Chapter 2 .....	8
BACKGROUND REVIEW .....	8
2-1. Introduction.....	8
2-2. Urban Growth Prediction Models .....	8
2-2-1. Cellular Automata (CA) Models.....	9



2-2-2. Artificial Neural Network (ANN) Models.....	10
2-2-3. Linear/Logistic Regression (LR) Models .....	11
2-2-4. Agent-Based Models (ABM) Models .....	12
2-2-5. Decision Trees (DT) Models.....	12
2-2-6. Fractals Geometry (FG) Model.....	13
2-3. Video Prediction Techniques .....	14
2-3-1. Transformation Approach .....	15
2-3-2. Action-Conditional Approach.....	17
2-3-3. Predicting from Static Images Approach .....	18
2-4. Summary .....	20
Chapter 3 .....	21
MAIN CONCEPTS AND PRELIMINARIES USED TO DEVELOP THE MODEL .....	21
3-1. Introduction.....	21
3-2. Convolutional Networks and Auto-Encoders (CAEs).....	21
3-3. Transfer Learning.....	24
3-4. Image Similarity Measures .....	25
3-5. Loss and Accuracy Measures.....	27
3-6. Earth Observation Satellite Images.....	28
3-7. Summary .....	30
Chapter 4 .....	32

MODEL ARCHITECTURE AND DATA REQUIREMENT .....	32
4-1. Introduction.....	32
4-2. Overview of Video Prediction (VP) Approach.....	32
4-3. Time-Dependent Encoder-Decoder (TDED) .....	33
Chapter 5 .....	37
DATA COLLECTION AND PREPARATION.....	37
5-1. Introduction.....	37
5-2. Study Area.....	37
5-3. Data Structure for Training and Validating the Model .....	39
5-4. Data Preparation.....	40
5-5. Computational Platform.....	42
5-6. Summery .....	42
Chapter 6 .....	43
SENSITIVITY ANALYSIS AND RESULTS.....	43
6-1. Introduction.....	43
6-2. Values of Hyper-Parameters .....	43
6-3. Effect of Number of Epochs .....	45
6-4. Effect of Batch Size .....	47
6-5. Examining the Performance of Different Optimizers .....	49
6-6. Effect of Data Size for Model Training .....	51

6-7. Effect of Different Model Structures .....	52
6-8. Summary .....	60
Chapter 7 .....	61
MODEL APPLICATION FOR THE DALLAS-FORT WORTH REGION .....	61
7-1. Introduction .....	61
7-2. Model Development for Collin County and Denton County .....	62
7-3. Validation the Model Result with North Central Texas Council of Government (NCTCOG) .....	69
7-4. Model Limitations .....	71
7-5. Summary .....	73
Chapter 8 .....	75
MODEL APPLICATION FOR THE MIDDLE EAST AND NORTH AFRICA (MENA) REGION .....	75
8-1. Introduction .....	75
8-2. Urban Growth Acceleration in the MENA Region .....	76
8-3. Overview of the Selected Cities .....	78
8-3-1. Dubai, UAE .....	79
8-3-2. Cairo, Egypt .....	81
8-3-3. Doha, Qatar .....	82
8-3-4. Casablanca, Morocco .....	83

8-3-5. Riyadh, KSA .....	84
8-4. A Review of Urban Growth Studies Conducted for the Selected MENA Cities.	86
8-5. Urban Growth Prediction for the Selected MENA Cities: Model Application ...	90
8-5-1. Dubai, UAE.....	99
8-5-2. Cairo, Egypt .....	101
8-5-3. Doha, Qatar .....	103
8-5-4. Casablanca, Morocco .....	106
8-5-5. Riyadh, KSA .....	107
8-6. Discussion and Conclusion .....	109
Chapter 9 .....	113
SUMMARY AND FUTURE WORK .....	113
9-1. Summary .....	113
9-2. Further Research Extensions.....	114
BIBLIOGRAPHY .....	116

## LIST OF TABLES

Table 3- 1: Landsat 5 and Landsat 7 spectral band description.....	29
Table 3- 2: Landsat 8 spectral band description.....	30
Table 3- 3: Number of available images for the DFW area for the different years.....	30
Table 4- 1: The dimensions of the different layers of the encoder-decoder architecture..	35
Table 5- 1: The longitude and latitude for the three study areas .....	38
Table 5- 2: Data structure for model training and validation .....	40
Table 6- 1: Values considered for the model parameters .....	44
Table 6- 2: The model performance for different number of epochs .....	46
Table 6- 3: The model prediction performance for different numbers of epochs. ....	47
Table 6- 4: The model performance for different batch sizes .....	48
Table 6- 5: The model prediction performance for different batch sizes. ....	49
Table 6- 6: The model performance for different optimizers.....	50
Table 6- 7: The model performance for different data sizes .....	52
Table 6- 8: Summary of five model structures with different number of layers.....	53
Table 6- 9: The performance of different model structures.....	54

Table 6- 10: Model 1 dimensions of the different layers of the encoder-decoder architecture .....	55
Table 6- 11: Model 2 dimensions of the different layers of the encoder-decoder architecture .....	56
Table 6- 12: Model 3 dimensions of the different layers of the encoder-decoder architecture .....	57
Table 6- 13: Model 4 dimensions of the different layers of the encoder-decoder architecture .....	58
Table 7- 1: The accuracy and loss recorded at the start and the end of the training process .....	62
Table 7- 2: The prediction performance of the three developed models.....	63
Table 8- 1: The Statistical information for the five MENA cities.....	85
Table 8- 2: The model prediction performance for the five MENA cities .....	91

## LIST OF FIGURES

Figure 3- 1: The biological neuron ( <a href="https://www.cs.toronto.edu">https://www.cs.toronto.edu</a> ).....	22
Figure 3- 2: The Convolutional Auto-Encoder structure. ....	23
Figure 3- 3: Transfer learning observations (Torrey & Shavlik, 2010).....	25
Figure 3- 4: Diagram of structural similarity index measurement system (Wang et al., 2004).....	27
Figure 3- 5: Image quality using SSIM technique.....	27
Figure 3- 6: Landsat missions ( <a href="https://landsat.usgs.gov">landsat.usgs.gov</a> ). ....	29
Figure 4- 1: Applying the video prediction paradigm for urban growth prediction modeling. ....	33
Figure 4- 2: The overall structure of the time-conditioned encoder-decoder architecture for UGPM.....	34
Figure 4- 3: Flowchart of the proposed model. ....	36
Figure 5- 1: Satellite images of the study areas showing their growth between 1985 and 2018. ....	39
Figure 6- 1: The convergence pattern of the model accuracy (left) and the loss (right) measures for 2000 epochs. ....	46

Figure 6- 2: The convergence pattern of the model accuracy (left) loss (right) for 64 batch size.....	48
Figure 6- 3: The convergence pattern of the model accuracy (left) and loss (right) for the RMSprop optimizer. ....	50
Figure 6- 4: The convergence pattern of the model accuracy (left) and loss (right) using dataset III. ....	52
Figure 6- 5: Comparison between the actual image and the predicted (constructed) images for different prediction horizons considering year 1985 as the base year. ....	59
Figure 7- 1: Urban growth prediction for the DFW area after three, five, and seven years considering 2018 as the base year. ....	66
Figure 7- 2: Urban growth prediction for Collin County after three, five, and seven years considering 2018 as the base year. ....	67
Figure 7- 3: Urban growth prediction for Denton County after three, five, and seven years considering 2018 as the base year. ....	68
Figure 7- 4: Model validation for Collin County by comparing the predicted urban growth with NCTCOG’s population growth prediction. ....	70
Figure 7- 5: Model validation for Denton County by comparing the predicted urban growth with NCTCOG’s population growth prediction. ....	71
Figure 8- 1: The five MENA cities considered in this study.....	79



Figure 8- 2: The convergence pattern of the accuracy (left) and loss functions (right) for the model’s training and validation processes for the five MENA cities considered in this study. ....	92
Figure 8- 3: Predicted urban growth of the city of Dubai for year 2026.....	93
Figure 8- 4: Predicted urban growth of the city of Cairo for year 2026.....	94
Figure 8- 5: Predicted urban growth of the city of Doha for year 2026.....	95
Figure 8- 6: Predicted urban growth of the city of Casablanca for year 2026. ....	96
Figure 8- 7: Predicted urban growth of the city of Riyadh for year 2026. ....	97
Figure 8- 8: Model validation and urban expansion of the city of Dubai. ....	101
Figure 8- 9: Model validation and urban expansion of the city of Cairo. ....	103
Figure 8- 10: Model validation and urban expansion of the city of Doha. ....	105
Figure 8- 11: Model validation and urban expansion of the city of Casablanca. ....	107
Figure 8- 12: Model validation and urban expansion of the city of Riyadh.....	109

## Chapter 1

### INTRODUCTION

#### 1-1. Background

Cities have historically created vast economic opportunities and provided the required services to their citizens efficiently and conveniently. They evolved from small concentrations around sources of fresh water to a dense fabric in the form of multiple interconnected centers. Studying the growth pattern of cities/urban areas has received considerable attention during the past few decades (Triantakonstantis and Mountrakis, 2012). The goal is to identify directions and locations of potential growth, assess infrastructure and public service requirements, and ensure the integration of the new developments with the existing city structure. In addition, urban growth has been studied for the purpose of deriving effective policies that help achieve sustainable and economically-sound growth patterns.

#### 1-2. Main Theories for Studying Urban Growth

Two main theories have been generally considered for studying urban growth: the ecological theory (Alberti et al., 2003; Wu, 2014) and the machine theory (Lubell et al., 2009). The ecological theory models urban areas as ecological systems that naturally adopt to alterations in biophysical and socio-economic activities. On the contrary, the machine

theory views growth as the outcome of a deliberate planning process defined by the interactions among different stakeholders including policy makers, city planners, land developers and residents. While the machine theory is widely accepted as it explains many of the growth phenomena observed in urban areas, advocates of the ecological theory view the machine theory as one phase of the natural process that shapes the long-term urban growth.

### **1-3. Challenges of Developing Urban Growth Prediction Models**

Several challenges and complexities characterize the urban growth prediction problem. For example, urban growth is a dynamic non-linear process in both time and space that is difficult to represent in a closed analytical form (Cheng, 2003; Triantakonstantis and Mountrakis, 2012). Therefore, most successful urban growth prediction models (UGPMs) have adopted simulation-based techniques that require considerable effort for model specification, calibration and validation (Chan and Chiu, 2000; Waddell, 2002; Leao et al., 2004; Li et al., 2014; Xia et al., 2019). Furthermore, urban growth prediction is normally impacted by many biophysical, socioeconomic and political variables that are in return difficult to obtain and/or predict (Cheng, 2003; Liberati et al., 2009). Thus, the results obtained by UGPMs usually require careful interpretation, considering the limitation and/or uncertainty of their input data. Also, urban growth involves complex interactions among policy makers, urban planners and developers (Cheng et al., 2003). Predicting the interest and decisions of the different stakeholders and capturing their interactions are nontrivial tasks.

#### **1-4. Emerging Technologies for Developing Urban Growth Prediction Models**

Two important technologies have significantly benefited the ongoing effort for UGPM development: (I) satellite imagery and (II) machine learning. Satellite imagery has been widely used as a reliable data source for UGPM development. They provide information on land cover change over time, which can be used to retrieve reliable information on the time-varying growth pattern in urban areas. However, the usage of these images has been limited mostly to manual data extraction for the purpose of model calibration and validation. The increased richness and quality of the satellite imagery datasets open the doors for more comprehensive usage of these images to develop the next-generation UGPMs.

Computer vision technologies have observed significant advancements during the past decade. Taking advantage of the growing data sizes and the enhanced computational capabilities, more accurate models for object recognition and classification are continuously developed ([Simonyan and Zisserman, 2014](#); [He et al. 2016](#)). Considering their fast advancements, machine learning techniques are increasingly adopted for developing UGPMs ([Berling-Wolff and Wu, 2004](#); [Triantakonstantis and Mountrakis, 2012](#)). In particular, artificial neural networks (ANN) have been adopted to overcome known limitations of regression-based models that are significantly impacted by the input data relationships (e.g., auto-correlation and multi-collinearity). In addition, deep learning (DL) has been introduced over the past decade as an extension of the traditional (shallow) machine learning methodologies. DL takes advantage of available large datasets and improved computational capabilities to build learning models in the form of many interconnected layers of nonlinear processing units for efficient feature extraction and

transformation. These layers systematically reduce the dimensionality of the problem in order to discover complex patterns and relationships in the data sets (LeCun et al., 2015; Schmidhuber, 2015). DL has shown great success in solving many complex problems that traditional learning methodologies failed to solve including computer vision, speech recognition, drug discovery, social network filtering (Deng et al, 2013; Black et al, 2020; Izbassarova et al, 2020; Zhavoronkov et al, 2020; Stokes et al, 2020; Roy et al, 2020), bio informatics and face recognition (Wang and Bai, 2018), medical (Kaur and Khosla, 2020; Black et al, 2020; Kalinin et al, 2020), defense (Husodo et al, 2019; Qiu et al, 2019; Ye et al, 2020), emergency response (Li et al, 2019; Cho et al, 2019), driverless vehicles (Chen et al, 2020; Thakurdesai and Aghav, 2020; Joubert et al, 2020), traffic network reliability analysis and real-time management (Hashemi and Abdelghany, 2018; Nabian and Meidani, 2018), vehicle type detection and classification (Molina-Cabello et al., 2018), traffic frequency crash analysis (Zhang et al., 2019), crowd counting (Shen et al., 2019), and infrastructure health monitoring (Acharya et al, 2018; Bang et al., 2019; Cha et al., 2018; Gao and Mosalam, 2018; Kang and Cha, 2018; Li et al., 2019; Maeda et al., 2018; Rafiei and Adeli, 2017, 2018; Rafiei et al., 2017; Xue and Li, 2018; Yang et al., 2018).

## **1-5. Research Approach**

This research presents a novel UGPM that builds on recent advances of these two technologies. An UGPM is developed in the form of a time-dependent encoder-decoder (TDED) with embedded convolutional neural networks (CNNs). The model treats successive satellite images taken for an urban area over an extended horizon as a video and aims at predicting future frames of that video based on the temporal and spatial features

learned from its past frames. A trained model considers as an input (a) a base-year satellite image of a pre-defined resolution for the urban area under study; and (b) the length of the prediction horizon of interest (i.e., target year). It generates an image that predicts the growth pattern for the urban area for the target year at the same resolution. The model can also generate an image that shows the growth pattern predicted for any time along the given horizon.

A dataset of a considerable size is used for model training and validation. Each record in this dataset consists of two different satellite images for the study area along with the time difference between these two images. The model is trained to learn the spatiotemporal growth features from the satellite images, which enables it to predict the growth pattern in the urban area for any given future year. We present the application of the new model through a case study in which the model is used to predict the urban growth pattern for the Dallas-Fort Worth, Texas (DFW) area with focus on Collin County and Denton County, which observed significant growth over the past decade. In addition, the model is applied to predict the growth pattern of five cities in the Middle East and North Africa (MENA) region. These cities vary in terms of their size, population, historical heritage, level of control applied to their growth, geographical locations, complexity of their structure, and socio-economic characteristics. The results of the case studies show that, despite their limited data requirements compared to other approaches adopted in the literature, the model is able to produce high-fidelity prediction results that are consistent with the results of other growth studies conducted for the urban areas considered in this study.

## **1-6. Research Contributions**

This problem contributes to the existing literature in several ways. To the author's knowledge, this research is among the first attempts to develop a DL-based model for urban growth prediction. The model is capable of extracting the temporal and spatial growth patterns from satellite images through adopting a TDED with embedded CNNs. Furthermore, the model deviates from most current practices that require intensive biophysical and socioeconomic data for model development. It proposes a new approach that extracts growth information from a series of satellite imagery that indirectly encapsulates such data. Developing UGPMs with reduced data requirements is highly desirable, considering the extensive effort that is typically associated with collecting data needed to develop most existing UGPMs. The research presents the results of a real-world case study that illustrates the application of the model and its ability to predict at high fidelity the growth pattern in two counties in the DFW area. In addition, we applied the model to five MENA cities including Dubai (United Arab Emirates (UAE)), Cairo (Egypt), Doha (Qatar), Casablanca (Morocco), and Riyadh (Kingdom of Saudi Arabia (KSA)). We present a framework to validate the model by comparing its results with data collected from other urban growth studies conducted for these cities. Finally, based on the obtained results and their analysis, the research provides recommendations for sustainable urban growth in the MENA region.

## **1-7. Dissertation Organization**

The dissertation is organized as follows. Chapter 2 presents a review of the literature and summarizes main approaches used for modeling urban growth prediction as

well as machine learning models for video prediction applications. Chapter 3 describes main concepts and preliminaries used to develop the model. Chapter 4 provides the model architecture and the data requirement for its training and validation. Chapter 5 describes the efforts of data collection and preparation. Chapter 6 presents a set of experiments that illustrates the sensitivity of the model with respect to the values assumed for its hyper-parameters. Chapter 7 presents a real-world case study that illustrates the application of the model to predict the growth pattern for the DFW area. Chapter 8 presents the model application for several cities in the MENA region along with their validation results. Finally, Chapter 9 provides a summary and presents research extensions.



## **BACKGROUND REVIEW**

### **2-1. Introduction**

This chapter reviews the literature of two topics related to urban growth prediction models (UGPMs) and video prediction (VP) models that are based on machine learning techniques. The chapter starts with section 2-2 that provides a review of the different modeling approaches used to develop urban growth prediction models. These approaches include Cellular Automata (CA), Artificial Neural Network (ANN), Linear/Logistic Regression (LR), Agent-Based Models (ABM), Decision Trees (DT) and Fractals Geometry (FG). Section 2-3 reviews previous research work focusing on video prediction (VP) methodologies and applications. The transformation approach, the action-conditional approach, and the predicting from static images approach are the main approaches used for developing most VP methodologies. Finally, section 2-4 concludes the review and summarizes the contribution of the proposed research with respect to the existing literature.

### **2-2. Urban Growth Prediction Models**

Previous studies have resulted in numerous UGPMs that differ in their underlying theory, data requirements, and scope of application. According to [Triantakoustantis and Mountrakis \(2012\)](#), the main objective of UGPMs is to capture the fundamental relationships of spatial and temporal complexities associated with urban growth prediction.

Spatial complexity pertains to the large number of socioeconomic and biophysical factors that affect urban growth along with their complicated interactions (Albeverio et al., 2007; Batty, 2013). Temporal complexity arises from the challenge of capturing how these factors change and interact over time to shape the future growth (Engelen, 1988).

Several modeling approaches have been proposed in the literature for developing UGPMs including Cellular Automata (CA), Artificial Neural Network (ANN), Linear/Logistic Regression (LR), Agent-Based Models (ABM), Decision Trees (DT) and Fractals Geometry (FG). According to a review study conducted by Triantakonstantis and Mountrakis (2012), CA, ANN and LR models are the most popular among these approaches as they demonstrated a superior performance in capturing the complex relationships of parameters relevant to predicting urban growth.

### **2-2-1. Cellular Automata (CA) Models**

Considering its relative simplicity, CA is widely used to develop UGPMs (Wu and Webster, 1998; He et al., 2006). CA represents complex dynamic environments in the form of a discrete system comprising of a grid of cells that interact with each other according to a set of pre-defined rules. A typical CA-based model for urban growth prediction consists of three main building blocks, which are (1) the grid/neighborhood of the study area; (2) the states defined for each cell; and (3) the transition rules that define the mechanism by which cells change their states (Stanilov and Batty, 2011).

The area under study is typically divided into cells of adequate sizes such that each cell represents a parcel of a homogenous land use type. A set of feasible states are then defined for each cell (e.g., developed or undeveloped). A cell transits from a current state

to another state according to pre-defined transition rules. Deriving accurate transition rules is the most critical task for developing CA-based UGPM as it significantly affects the model's prediction performance (Debnath and Amin, 2015; D'Autilia and Hetman, 2018).

These rules are typically extracted from historical growth pattern for the urban area under study or for other similar urban areas. Examples of case studies that illustrate the application of CA-based UGPM can be found in Clarke and Gaydos, (1998), Van Vliet et al. (2009), Chaudhuri and Clarke (2013), and Ke et al. (2016). A widely known CA-based UGPM is the SLEUTH (slope, land cover, excluded, urban, transportation, and hill-shade) model (Chaudhuri and Clarke, 2013). While the SLEUTH model has shown successes in explaining the growth phenomena observed in many cities around the world, the considerable effort and the large amount of data required for its calibration and validation remain to be obstacles for its adoption.

### **2-2-2. Artificial Neural Network (ANN) Models**

The ANN model is a popular machine learning technique, which is used effectively to model land use change and urban growth prediction (e.g., Pijanowski et al., 2002; Lin et al., 2011; Tayyebi and Pijanowski, 2014; Shafizadeh-Moghadam et al., 2017). One advantage of ANN over traditional regression analysis is that it does not require making assumptions regarding spatial autocorrelation that might be presented in the input data.

As indicated by Tayyebi et al. (2014), the multi-layer-perceptron (MLP) neural network is one of the most commonly ANN forms that is widely applied for modeling land use change and urban growth. This MLP model consists of at least three layers of nodes, which are the input layer, one or more hidden layers, and the output layer. The MPL model

is trained using the back-propagation algorithm, which follows an iterative procedure to determine the optimal weight that minimizes the difference between the training data and the estimated output (Chauvin and Rumelhart, 2013; Zhang and Goh, 2016).

The enhanced computational capabilities during the past few decades have enabled the development of rigorous ANN-based models with rich socioeconomic and environment input data for studying complex urban growth patterns (Berling-Wolff and Wu, 2004). For example, Liu and Seto (2008) and Thapa and Murayama (2009) developed an ANN-based models with input data that includes topology, land use, and roadway network extracted from satellite images to predict city boundaries and developed areas within these boundaries.

Tayyebi et al. (2011) developed a similar model to evaluate the complex geometry of cities and boundaries of future growth by considering variables such as green spaces, built areas, distances from roads, service stations, etc. ANN models have also been integrated with GIS tools to provide a platform to forecast and visualize changes in land use (Pijanowski et al., 2005).

### **2-2-3. Linear/Logistic Regression (LR) Models**

Several LR-based models are proposed for developing UGPMs (Hu and Lo, 2007; Yang et al., 2011; Kang, 2014; Gerasimovic et al., 2016; Han and Jia, 2017). LR is useful for driving a relationship that explains urban change in terms of different explanatory variables. For example, Yang et al. (2011) and Han and Jia (2017) developed UGPMs in the form of LR that combine variables such as socioeconomic, land topology, land zoning, and accessibility to the city center.

In these models, a binary output variable is used to indicate land use change. LR models have also been developed to study land use change with focus on retail and commercial location modeling. For instance, the LR model developed by [Mustafa et al. \(2017\)](#) is shown to present the growth in commercial developments as a function of the evolution of the road network and changes in property taxes.

#### **2-2-4. Agent-Based Models (ABM) Models**

ABM has been also used to understand and predict different urban growth scenarios ([Brown and Duh, 2004](#)). A simplest ABM consists of two components, which are (1) a system of agents (e.g., people, organizations, etc.); and (2) the rules that govern the interactions between these agents ([Bonabeau, 2002](#)). An agent is an autonomous unit that is assumed to be able to interact with other agents in the system and take actions following the predefined rules. As such, the behavior of the agents permits the effect of human decision making to be incorporated into the model.

The pioneer work of [Sanders et al. \(1997\)](#) is an example of adopting ABM to model urban growth. [Zhang et al. \(2010\)](#) presents another example of using ABM to simulate the interactions among government agencies, farmers, and residents to predict urban growth. However, one drawback of ABM-based UGPMs is that they might produce highly variable results depending on the rules defined for agent interactions and decision making ([Couclelis, 2002](#)).

#### **2-2-5. Decision Trees (DT) Models**

The DT technique presents a simple model structure that is used to derive rules for optimal data segmentation. The construction of most DTs for urban growth prediction

involves three stages following an iterative procedure: a primary stage in which nodes are split recursively, an optional pruning stage to lower the tree complexity, and a final stage to select the optimal tree that gives the least testing error (Giovanis, 2012).

Most work that adopted the TD technique focused on developing tools for the classification of remote sensing images (Friedl et al., 1999; Hansen et al., 2000; Chan et al., 2001; Schneider et al., 2003; Li and Yeh, 2004; Tooke et al., 2009). For example, Li and Yeh (2004) and Tooke et al. (2009) developed DT-based models to classify the land in remotely sensed imagery in terms of its type (e.g., urban development, vegetation cover, etc.). Two challenges face the development of DT-based models for land use classification. First, similar to other models such as ANN, DT can create overfitting structures which prevent their generalization, Second, spatial autocorrelation might cause these models to underperform compared to other classification techniques.

#### **2-2-6. Fractals Geometry (FG) Model**

Witten and Sander (1981) and Mandelbrot (1983) are among the first to adopt FG for studying urban growth, assuming that urban growth follows a spatial self-organization characteristic. FG is shown to generate a more accurate descriptions for spatiotemporal growth patterns compared to those obtained using the classical Euclidean geometry (Frankhauser, 2008).

The diffusion-limited aggregation (DLA) method, developed by Witten and Sander (1981), is an example of the FG approach. DLA is defined as a process where a structure grows through the aggregation of units which spread over space until they arrived to a certain point (Fotheringham et al., 1989). This point is classified as ‘developed’ compared

to the rest of the urban area which is classified as ‘undeveloped’. [Batty et al. \(1989\)](#) proposed the DLA method to represent the urban structures in the form of tree-like, which manifesting self-similarity of the form across different scales. Several algorithms are used in the literature to calculate fractal dimensions.

As reported by [Myint \(2003\)](#), different results may occur for the same urban area when using different approaches of fractal dimension measurement. Thus, one should carefully choose the fractional dimension measurement that produces urban growth pattern that is consistent to what is historically observed in the urban area under study.

### **2-3. Video Prediction Techniques**

The main goal of video prediction (VP) is to obtain future frames of any video by producing a possible trajectory for it based on a sequence of frames that have already been seen ([Ge, 2017](#)). In other words, it aims to infer future frames from a series of earlier frames while minimizing the reconstruction error that may occur between the actual future frame and the future frame that is generated.

As described hereafter, most VP models are built on top of an encoder-decoder system that consists of at least three basic components: (1) convolutional encoders, (2) a set of convolutional layers or fully connected layers, and (3) deconvolutional decoders ([Oh et al., 2015](#); [Ge, 2017](#); [Vukotić et al., 2017](#)). Convolutional encoders extract main features of the input images which are transformed into latent variables through the fully connected layers. These latent variables are decoded back to an image by the deconvolutional decoders.

Three main approaches are considered for developing most VP methodologies presented in the literature, which are the transformation approach, the action-conditional approach, and the predicting from static images approach.

### **2-3-1. Transformation Approach**

The idea of the transformation-based approach is to predict a change that maps the input sequence of frames to the next frame as opposed to generating pixels of the next frame directly. Therefore, the approach is shown to be more suitable for natural videos in which there is a smooth and continuous motion of objects. However, it does not work well for videos in which objects may move in and out of the scenes. Another advantage of the transformation-based approach is that it can generate sharper images using small-size models as it focuses on predicting the change rather than the entire image ([Van Amersfoort et al., 2017](#)).

Numerous VP models that are based on transformation-based approach have been reported in the literature. For example, [Patraucean et al. \(2015\)](#) proposed a model that adopts a convolutional – long short-term memory (LSTM) – deconvolutional architecture for optical flow prediction. The architecture encompasses a sampling module and a grid generator to build the subsequent image based on the optic flow. One strength of this model is that the predicted optical flow could be integrated with another model such as a semantic segmentation model to implement video segmentation.

[Van Amersfoort et al. \(2017\)](#) developed a convolutional model to predict the local affine transformations for overlapping patches. An affine transformer is defined as a function that maps an affine space to itself or similar objects in the space. It preserves the



dimension of any affine subspaces and also preserves the ratio of the lengths of parallel line segments. An affine transformation does not necessarily preserve angles between lines or distances between points. However, it preserves ratios of distances between points lying on a straight line. Consider an example of tree leaves, an affine transformer can be developed to map these leaves to each other even they have different angles and sizes. The model involves devising an affine transform extractor that identifies the set of affine transforms which is essential in constructing a frame with minimum MSE loss function. The resulting affine mappings from this procedure were utilized in the convolutional model as inputs and used for training as ground truth. While the model is shown to attain superior outcomes in terms of the accuracy of a standard classifier on the future frames, it shares the limitation of not being able to generate new objects that are not represented in input frames due to the preservation of lines and points by affine transformations.

[Liu et al. \(2017\)](#) introduced the deep voxel flow (DVF) model which adopts a multi-scale convolutional architecture for predicting voxel flow. Similar to a pixel in a 2D bitmap, a voxel represents a single data point on a three-dimensional grid that is regularly spaced. This data point can consist of a single piece of data, such as an opacity, or multiple pieces of data, such as a color and opacity. The DVF model can be implemented and used in different tasks such as action recognition, flow estimation, and video extrapolation. The DVF model is shown to be capable of generating sharp frames utilizing a small model consisting of three deconvolutional and convolutional layers. However, it has been argued that the model may fail in instances where the scenes have repetitive patterns (e.g., Parks) ([Liu et al. 2017](#)).

### 2-3-2. Action-Conditional Approach

The action-conditional approach solves the VP problem by recognizing that future frames do not rely only on the sequence of previous frames, but also on the action taken at the current time step (Kalchbrenner et al., 2017). The action-conditional is used as the basis for developing several VP models (Oh et al., 2015; Srivastava et al., 2015; Xue et al., 2016; Chiappa et al., 2017).

For example, Watter et al. (2015) developed the embed-to-control (E2C) model, which is used to learn and control a non-linear dynamical system from historical images. The model produces image trajectories from a latent space to simplify the system from non-linear to be locally linear. The model allows long-term predictions of image sequences to be accomplished without degrading the representations quality.

Oh et al. (2015) proposed a deep action-conditional model to predict future image-frames of the Atari game through the combination of controller variables (or action) at the existing frame. A multi-phase training based on time steps is used to ensure that the model is learning how to make a longer sequence of accurate predictions as suggested by Michalski et al. (2014). Two encoding variants were examined, which are feedforward and recurrent encoding. The feedforward encoding takes a fixed number of past frames as an input, while the recurrent encoding takes one frame for each time step as an input and used LSTM to memorize the information about the past frames. The model is shown to be able to predict realistic frames and also control future frames in several domains of Atari games.

Finn et al. (2016) developed an action-conditioned video prediction model that learns to predict a transformation by connecting the present frame to the following one. An

architecture that contains multiple LSTM cells is proposed, which divides the image into a background layer and a foreground layer. A transformation to the foreground is then applied and combined again with the background layer to form the predicted image. The model is tested using datasets representing real-world interactive agents. The model is shown to produce high quality video predictions both qualitatively and quantitatively.

### **2-3-3. Predicting from Static Images Approach**

The prediction from static images approach is utilized as a foundation for several VP models (Pintea et al., 2014; Chao et al., 2017). The idea is to use a series of past successive static images to learn the movement pattern (e.g., direction and speed) and extrapolate this pattern for a given future time. The approach has shown to be useful for applications such as automated animation and visual analogy-making (Xue et al., 2016).

For example, Sohn et al. (2015) developed a model called conditional variational auto-encoder (CVAE) that is an extension of the variational autoencoder (VAE). CVAE is a conditional directed graphical model, in which the outputs are generated as the input observation modulates and the prior on latent variables. Yan et al. (2016) used CVAE to model the conditional distribution of future frames, where it is used to maximize the reconstruction log-likelihood of the input under a condition. Walker et al. (2016) proposed a CVAE architecture consisting of fourteen convolutional layers for extracting visual representations from the image used by the decoder and encoder.

Xue et al. (2016) proposed a convolutional network to synthesize the movement of an object by encoding the image information as feature maps and the motion information as convolutional kernels. This network is designed by introducing a cross convolutional

layer into a CVAE model. This layer considers the fact that different semantic segments that exist in an image are having different distributions over all possible motions (e.g., a building is often static, but a waterfall flows). While the model produces good results for synthetic data (e.g., animated game and 2D shapes), the model could generate superficial artifacts when seeking to simulate large movements.

[Vondrick et al. \(2016\)](#) proposed a generative adversarial network (GAN) model for video prediction using spatiotemporal convolutional architecture. The architecture consists of two independent streams: (1) a pathway for generating a static background; and (2) a pathway for generating a dynamic foreground. The two pathways are then combined to generate the future video. A limitation of using this model is that it sometimes predicts a reasonable future but is incorrect. For example, the generated video could have a similar scene to the input image but not identical as some objects are dropped or some colors are altered.

Regardless of the phenomenal improvement in VP methodologies over the past decade, several challenges are still to be addressed by the research community. For example, developing frameworks that can learn spatiotemporal information would usually require evaluating the effectiveness of various non-trivial options in terms of model structure and parameter values. Another challenge is related to the high computation expenses associated with evaluating these options ([Tran et al., 2017](#)). In addition, most methodologies are deficient in capturing long contexts ([Simonyan and Zisserman, 2014](#)). As the prediction horizon increases, the prediction error tends to increase effecting the reliability of the obtained prediction. Thus, one should be careful on selecting the proper application for VP tools and interpreting their results.

Finally, [Karpathy et al. \(2014\)](#) reveal that the lack of a standard benchmark slows the development of VP methodologies. As videos are significantly more difficult to collect, annotate and store, comprehensive datasets that cover different applications are needed to be established.

#### **2-4. Summary**

The chapter discussed several approaches considered for urban growth prediction modeling. These approaches aim at capturing the complex relationships of main variables that affect urban growth such as socio-economic, biophysical, and political variables. Numerous publications focused on studying the complexity of the UGPMs, which showed that urban growth is a dynamic non-linear process in both time and space, which is difficult to represent in a closed analytical form. Most of the effective UGPMs have adopted simulation-based techniques which require considerable effort for model specification, calibration and validation. The chapter also reviewed VP techniques which proposed to infer future frames from a series of earlier frames while minimizing the reconstruction error that may occur between the actual future frame and the future frame that is generated. The transformation approach, the action-conditional approach, and the predicting from static images approach are the main three VP techniques that have been widely used in the literature.

## Chapter 3

### **MAIN CONCEPTS AND PRELIMINARIES USED TO DEVELOP THE MODEL**

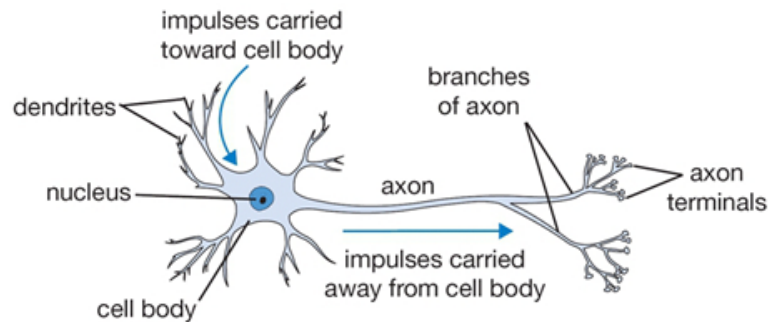
#### **3-1. Introduction**

This chapter presents the preliminaries and concept required for developing and validating the proposed UGPM. The chapter is organized as follows. Section 3.2 formally describes the concepts of CNNs and convolutional auto-encoders (CAEs) which represent the foundation for our UGPM. Section 3.3 presents the concept of transfer learning (TL) which focuses on adapting knowledge from a source task to a target task to build a target prediction model with good performance. Section 3.4 illustrates the measures that have been proposed in the literature to evaluate the similarity between two images for the purpose of validating the developed UGPM. Section 3.5 presents measures that are commonly used to evaluate the training and validation processes of neural networks such as the loss function and accuracy. Section 3.6 presents historical overview of the use of civilian satellites for Earth observation. Finally, Section 3.7 gives a summary of the chapter.

#### **3-2. Convolutional Networks and Auto-Encoders (CAEs)**

CNN, In the past, known as Neocognitron and inspired by biological processes where neurons are connected to resemble the organization of the mammal's visual cortex ([Fukushima, 1980](#); [Hubel & Wiesel, 1968](#)). The neurons consist of three sections, the

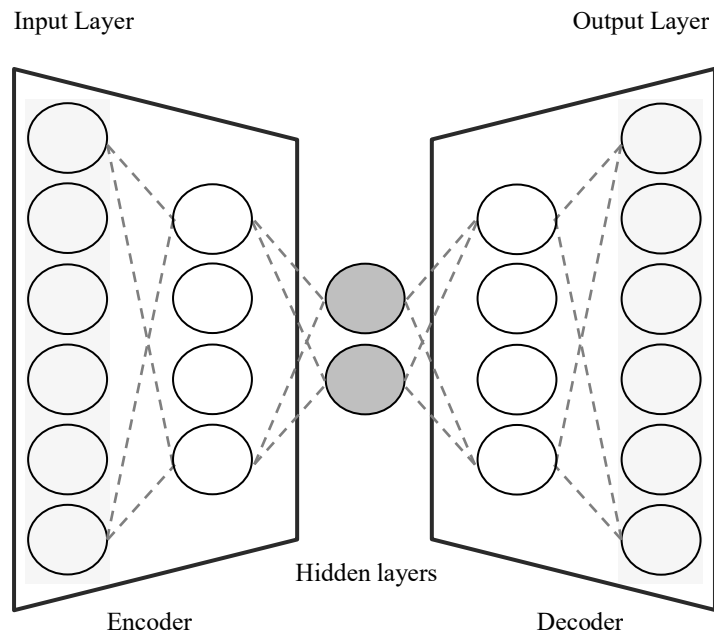
dendrites to receive the (input), cell nucleus (processor), and an axon (output) as shown in Figure 3-1.



**Figure 3- 1: The biological neuron (<https://www.cs.toronto.edu>).**

CNNs or ConvNets is a category of deep neural networks that are intensively used to classifying visual imagery (Zafar et al., 2018). A Typical CNN consists of a sequence of convolution and pooling operations that are followed by several fully connected layers. Every CNN contains four layers or blocks: The Convolution Layer, the Non-Linearity (ReLU activation) Layer, the Pooling Layer, and the Fully-Connected (FC) Layer (Zhou et al., 2017).

The job of the convolutional layer is to detect the important characteristics in the image pixels. The Rectified Linear Unit (ReLU) is a powerful non-linearity operation. It replaces all the pixels that have negative values in the feature map with zero. The result is then passed from the convolution layer through an ReLU activation function to the following layer. The pooling layer is used to reduce each dimension of the feature map, which helps to reduce the number of parameters and computation processes in the network. Finally, the FC layers use the high-level features from the convolution and pooling layers for classifying the input image into different classes determined by the training data.



**Figure 3- 2: The Convolutional Auto-Encoder structure.**

CAEs can be viewed as a type of CNN (Lintas et al., 2017). While CNNs are trained end-to-end to combine features and learn filters in order to classify the input, CAEs, by contrast, are only trained to learn filters, which extract features that can then be used for reconstruction of the input (Zhou et al., 2017). As illustrated in Figure 3-2, a typical CAE consists of two parts: the encoder and the decoder. Both the encoder and the decoder consist of a series of convolutional layers as described above. In the encoder part, the convolutional layers are used to decrease the complexity of the model by gradually reducing the number of hidden units (filters or the resolution of the output).

Two common approaches are used to down-scaling a layer, which are employing convolutions with strides and using a small window as a pooling value. The decoder works as reverse version of the encoder part. Its layers gradually up-scale the low-dimension



image that comes from the encoder. The process of up-scaling the layers is typically referred to as deconvolution, which is repeated until the size of the original image is obtained.

### **3-3. Transfer Learning**

While TL was originally proposed under the name ‘transfer of practice’ by [Woodworth and Thorndike \(1901\)](#), the earliest cited work on adopting TL for machine learning is [Pratt \(1993\)](#). TL focuses on adapting knowledge from a source task to a target task with little or no label information to build a target prediction model with good performance. As shown in the Figure 3-3, two main possible observations are usually associated with adopting TL. First, the use of transferred knowledge provides a higher starting and end performances in the target task compared to those obtained without any transferred knowledge. Second, adopting TL usually results in a steeper learning rate which reduces the amount of time required to allow the target task to be fully learned ([Torrey and Shavlik, 2010](#)).

In some cases, the model performance decreases when TL is used, implying that negative transfer has occurred. The effectiveness of the TL method depends on the relation between the source task and the target task. For example, if we transfer knowledge from a model that has certain data to a different model with a different structure of data, that might decrease the performance of the target task. Thus, for TL to succeed, one should ensure that there is a strong relationship between the source task and the target task in terms of the model structure and the data to achieve a higher performance.

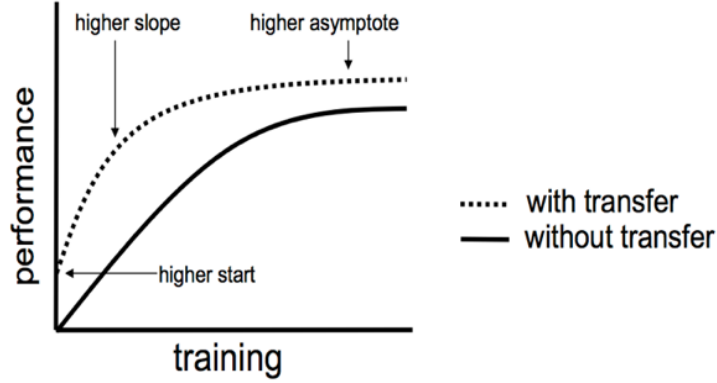


Figure 3- 3: Transfer learning observations (Torrey & Shavlik, 2010).

### 3-4. Image Similarity Measures

Validating the developed UGPM requires comparing its output images with the ground truth images. Two main measures are commonly used for measuring image similarity that are adopted in this research, which are (a) the Mean Square Error (MSE) and (b) the Structural Similarity Index (SSIM). The objective of the MSE measure is to compare two data streams or signals representing the observed and predicted values. It provides information on the degree of similarity or alternatively finds the level of distortion that exists between the two signals (Wang and Bovik, 2009). The general form of the MSE equation is given as follows:

$$MSE(Y, \hat{Y}) = \frac{1}{n} \sum_{i=1}^n (y_i - \hat{y}_i)^2 \quad (1)$$

where  $MSE(Y, \hat{Y}) \geq 0$ , and  $Y = \{y_i | i = 1, 2, \dots, n\}$  and  $\hat{Y} = \{\hat{y}_i | i = 1, 2, \dots, n\}$  are two discrete, finite-length signals (e.g., visual images),  $n$  is the number of signal samples (if the signals are images, then these will be pixels), and  $y_i$  and  $\hat{y}_i$  are the values of the  $i$ -th

samples in  $Y$  and  $\hat{Y}$ , respectively. A smaller MSE value implies that the two signals are more similar.

The SSIM index is designed specifically for calculating the similarity existing between two images to quantify their visual similarity (Wang et al., 2004). As shown in the Figure 3-4, the SSIM first computes the correlations between two images  $X$  and  $Y$  in three terms luminance, structure, and contrast at the local level. Then, these quantities are averaged over the whole image (Renieblas et al., 2017). The values of the SSIM index ranges from zero (completely different images) to one (identical patches). Equations (2) to (4) give the computation of the luminance, contrast, and structure comparisons, while Equation (5) shows how these comparisons are used to compute the SSIM.

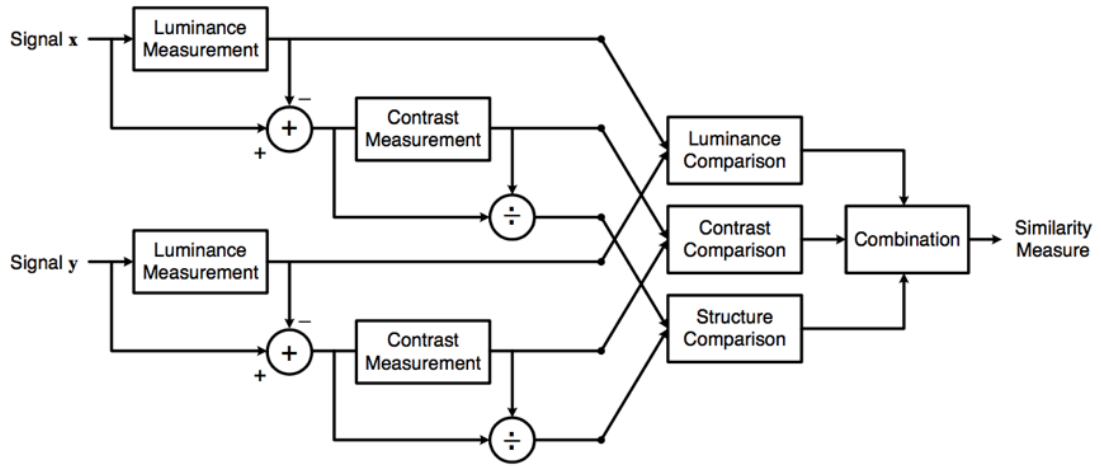
$$\text{Luminance comparison: } l(x, y) = \frac{(2\mu_x\mu_y+c1)}{(\mu_x^2+\mu_y^2+c1)} \quad (2)$$

$$\text{Contrast comparison: } c(x, y) = \frac{(2\sigma_x\sigma_y+c2)}{(\sigma_x^2+\sigma_y^2+c2)} \quad (3)$$

$$\text{Structure comparison: } s(x, y) = \frac{(\sigma_{xy}+c3)}{(\sigma_x\sigma_y+c3)} \quad (4)$$

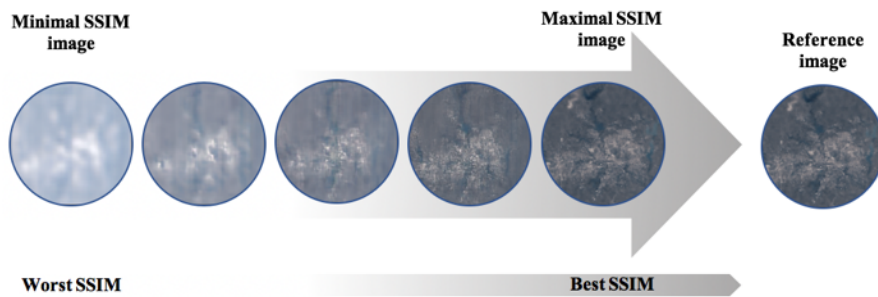
$$SSIM(x, y) = [l(x, y)]^\alpha \cdot [c(x, y)]^\beta \cdot [s(x, y)]^\gamma \quad (5)$$

where  $\mu_x$ ,  $\mu_y$ ,  $\sigma_x$ ,  $\sigma_y$ , and  $\sigma_{xy}$  are the local means between the two images, the standard deviations of the signals, the covariance for images  $X$  and  $Y$ , respectively. The user-defined constants  $c1$ ,  $c2$ ,  $c3$  are introduced if the local means and variances are close to zero. The overall index is created via a multiplicative combination of the three terms presented in equation (5), where  $\alpha$ ,  $\beta$ , and  $\gamma$  are parameters defining the relative importance of the three components.



**Figure 3- 4: Diagram of structural similarity index measurement system (Wang et al., 2004).**

Figure 3-5 illustrates the minimal/maximal SSIM images. These images are assumed to be equal in MSE values but extremely different quality to the reference image. As long the image far away from the reference image, it has the worst SSIM. On the other hand, if the image close to the reference image, it has the best SSIM.



**Figure 3- 5: Image quality using SSIM technique.**

### 3-5. Loss and Accuracy Measures

Two measures are commonly used to evaluate the training and validation processes of neural networks which are the value of the loss function and the accuracy measure

(Capelo, 2018). In case the prediction results are very different from the actual results, the loss function produces a very large number. Loss functions can be categorized into two different types which are Regression losses (e.g., MSE, root mean squared error (RMSE), etc.) and Classification losses (e.g., binary cross-entropy, categorical cross-entropy, etc.). The purpose of using the accuracy measure is to evaluate how the prediction accuracy of the model (Pelánek, 2015). The general form of the accuracy is presented in the equation (6):

$$Accuracy = \frac{\text{Number of correct predictions}}{\text{Total number of prediction}} \quad (6)$$

The other form that can calculate the accuracy is binary classification in terms of positive and negative classes, which is presented in the equation (7):

$$Accuracy = \frac{TP + TN}{TP + TN + FP + FN} \quad (7)$$

Where  $TP, TN, FP$  and  $FN$  are true positives, true negatives, false positives, and false negatives.

### 3-6. Earth Observation Satellite Images

The first civilian Earth observation satellite (ERTS-1), later named as Landsat 1, was launched in 1972. This effort was then followed by launching satellites Landsat 2, Landsat 3, and Landsat 4 in 1975, 1978, and 1982, respectively. These early-launched satellites provided low-resolution images, which limited their application for urban growth studies. Newer satellites, Landsat 5, Landsat 7, and Landsat 8, which were launched in 1984, 1999, and 2013, respectively, provided higher resolution images of 30 meters per pixel as shown in the Table 3-1 and 3-2. Obtaining such high-resolution images opened the

doors for their wide use in land use and urban growth studies (Longley and Mesev, 2000; Masek et al., 2000; Bagan and Yamagata, 2015; El Garouani et al., 2017).

Figure 3-6 shows the timeframe covered by all satellites. Each satellite provided a number of images per year that might vary from year to year depending on the study area under consideration. Some of the downloaded images could be unclear in cases where they were recorded on a cloudy day. Table 3-3 gives the number of images downloaded from year 1984 to 2018 for the Dallas-Fort Worth (DFW) area which its growth pattern is studied as part of this research work. The table shows the number of downloaded clear images in each year and the satellite used to obtain these images.



**Figure 3- 6: Landsat missions ([landsat.usgs.gov](https://landsat.usgs.gov)).**

**Table 3- 1: Landsat 5 and Landsat 7 spectral band description**

Bands	Wavelength (µm)	Resolution (m)
Band 1: Blue	(0.45 - 0.52)	30
Band 2: Green	(0.52 - 0.60)	30
Band 3: Red	(0.63 - 0.69)	30
Band 4: Near Infrared	(0.76 - 0.90)	30
Band 5: Short-wave Infrared 1	(1.55 - 1.75)	30
Band 6: Thermal	(10.40 - 12.50)	120, 60 * (30)
Band 7: Short-wave Infrared 2	(2.08 - 2.35)	30
Band 8 - Panchromatic (Landsat 7 only)	(0.52 - 0.90)	15

**Table 3- 2: Landsat 8 spectral band description**

<b>Bands</b>	<b>Wavelength (µm)</b>	<b>Resolution (m)</b>
Band 1: Ultra-Blue (coastal/aerosol)	(0.435 - 0.451)	30
Band 2: Blue	(0.452 - 0.512)	30
Band 3: Green	(0.533 - 0.590)	30
Band 4: Red	(0.636 - 0.673)	30
Band 5: Near Infrared	(0.851 - 0.879)	30
Band 6: Short-wave Infrared 1	(1.566 - 1.651)	30
Band 7: Short-wave Infrared 2	(2.107 - 2.294)	30
Band 8: Panchromatic	(0.503 - 0.676)	15
Band 9: Cirrus	(1.363 - 1.384)	30
Band 10: Thermal Infrared 1	(10.60 - 11.19)	100 * (30)
Band 11: Thermal Infrared 2	(11.50 - 12.51)	100 * (30)

**Table 3- 3: Number of available images for the DFW area for the different years**

<b>Year</b>	<b>1985</b>	<b>1986</b>	<b>1987</b>	<b>1988</b>	<b>1989</b>	<b>1990</b>	<b>1991</b>	<b>1992</b>	<b>1993</b>	<b>1994</b>	<b>1995</b>	<b>1996</b>
<b>No. of downloaded images</b>	9	12	12	12	12	10	12	12	12	12	12	12
<b>No. of clear images</b>	3	4	4	6	2	2	4	4	3	3	4	3
<b>Satellite ID</b>	Landsat 5											
<b>Year</b>	<b>1997</b>	<b>1998</b>	<b>1999</b>	<b>2000</b>	<b>2001</b>	<b>2002</b>	<b>2003</b>	<b>2004</b>	<b>2005</b>	<b>2006</b>	<b>2007</b>	<b>2008</b>
<b>No. of downloaded images</b>	12	12	12	12	12	11	12	12	11	12	10	11
<b>No. of clear images</b>	3	4	9	4	5	5	4	3	5	3	2	5
<b>Satellite ID</b>	Landsat 5											
<b>Year</b>	<b>2009</b>	<b>2010</b>	<b>2011</b>	<b>2012</b>	<b>2013</b>	<b>2014</b>	<b>2015</b>	<b>2016</b>	<b>2017</b>	<b>2018</b> up to the study starting date		
<b>No. of downloaded images</b>	12	12	11	12	10	12	12	12	12	3		
<b>No. of clear images</b>	6	6	7	2	2	4	4	7	4	2		
<b>Satellite ID</b>	Landsat 5			Land-sat 7	Landsat 8							

### 3-7. Summary

This chapter introduced preliminaries based on which the proposed UGPM are developed. The chapter described the concept of convolutional neural networks and auto-encoders which is mostly used in visual imagery classification. Then, the concept of

transfer learning is then described. The chapter also provided a review of similarity measures (SSIM and MSE) used to compare images. Finally, the chapter described the history of launching satellites for civilian applications and the effort to obtain images from model development and validation.



## Chapter 4

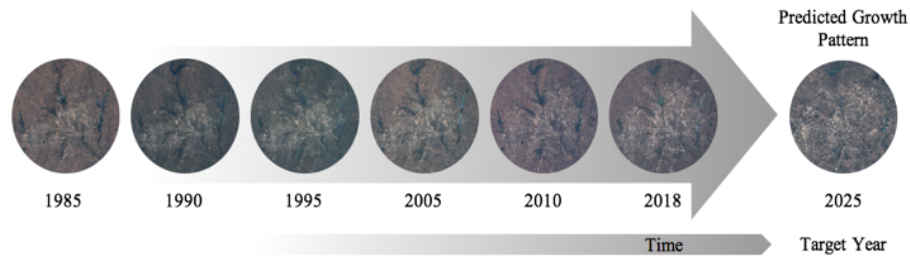
### MODEL ARCHITECTURE AND DATA REQUIREMENT

#### 4-1. Introduction

This chapter presents a novel solution methodology for urban growth prediction that adopts a VP technology. The VP technology allows the model to predict urban growth in a target year by learning the growth in previous years. A TDED with embedded CNN is developed. This Chapter is organized as follows. Section 4.2 presents an overview of the Video Prediction (VP) technique. Section 4.3 gives the details of the developed model which is in the form of a TDED with embedded CNN.

#### 4-2. Overview of Video Prediction (VP) Approach

In this section, we describe the structure of a novel ML-based model for UGPM. As illustrated in Figure 4-1, the model adopts a VP approach as it treats successive satellite images recorded for an urban area over an extended past horizon as a video. The model is trained using these historical satellite images to learn the spatiotemporal growth pattern (i.e., direction and rate of growth over time). The model obtains input an image  $x$  representing the urban area in base year  $t_0$  and a pre-defined prediction horizon ( $\Delta t, \Delta t \in I^+$ ). It constructs an image  $y$  that predicts the urban area for future year  $t_0 + \Delta t$ , using the learned historical growth pattern.



**Figure 4- 1: Applying the video prediction paradigm for urban growth prediction modeling.**

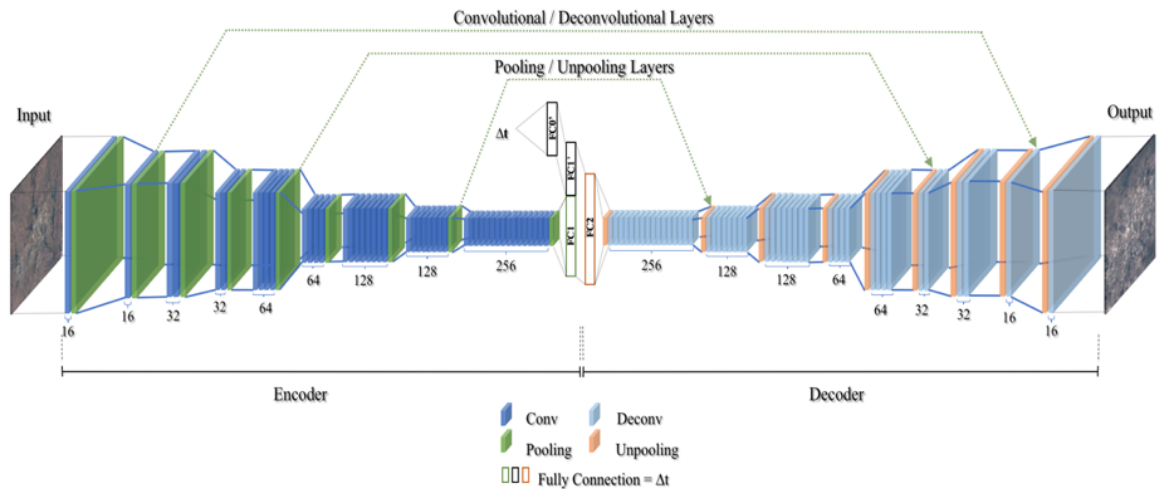
### 4-3. Time-Dependent Encoder-Decoder (TDED)

The model adopts a structure similar to the ones presented in [Tatarchenko et al. \(2016\)](#) and [Vukotić et al. \(2017\)](#), respectively, for general-purpose video prediction. It implements a TDED with embedded convolutional neural networks. Figure 4-2 illustrates the overall configuration of the model. As shown in the figure, the model is composed of two main parts; an encoder and a decoder.

The encoder receives two input elements. The first input is the base-year satellite image for the urban area under study with a pre-defined resolution. The second input is the length of the prediction horizon of interest  $\Delta t$  (i.e., desired temporal movement). As shown in the Figure 4-3, the input image is encoded through a series of convolutional and pooling layers. The first convolutional layer defines the resolution of the input image (height, width, and color channels). The last layer is connected with a fully connected neural network, FC1, that encodes the image information. The time horizon input is directly encoded into two consecutive fully connected networks, FC0' and FC1', respectively. The two fully connected networks FC1 and FC1' are concatenated forming one fully connect network, FC2, that combines the image and the time horizon information. The decoder is responsible for decoding the information in FC2 to generate the predicted image for the

specified time horizon. As shown in the figure, the decoder follows a reverse structure of the encoder through implementing a series of de-convolutional and up-sampling (unpooling) layers to construct an image for the target year with the same resolution as that of the input image.

Table 4-1 provides more details on the different layers used to construct the encoder and the decoder, respectively. In the current implementation, a colored image with 512x512x3 resolution is processed using five convolutional layers with 1x1 strides in each layer and five maximum pooling layers. These layers transform the input tensor to a tensor of 16x16x256. This tensor is processed through a dense network of dimension 16x16x256. The time horizon is encoded into another tensor with dimensions 16x16x1. Thus, a concatenated tensor with dimensions 16x16x257 is obtained, which is considered as the input for the decoder. The decoder consists of five deconvolution layers and five unpooling layers which gradually decode the concatenated input tensor to produce the predicted image with 512x512x3 resolution.



**Figure 4- 2: The overall structure of the time-conditioned encoder-decoder architecture for**

**UGPM.**

**Table 4- 1: The dimensions of the different layers of the encoder-decoder architecture**

Layer ID	Layer type/ Activation	Kernel size	Strides	Filter	Spatial input size
<b>Encoder</b>					
<b>Input 1 (512x512) RGB image</b>					
CL1	Conv2D-ReLU	3x3	1x1	16	512x512
MaxPooling2D					
CL2	Conv2D-ReLU	3x3	1x1	32	256x256
MaxPooling2D					
CL3	Conv2D-ReLU	3x3	1x1	64	128x128
MaxPooling2D					
CL4	Conv2D-ReLU	3x3	1x1	128	64x64
MaxPooling2D					
CL5	Conv2D-ReLU	3x3	1x1	256	32x32
MaxPooling2D					
FC1					
<b>Input 2 (Time)</b>					
FC0' (time)					
FC1' (time)					
Concatenate (FC1, FC1' (time))					
FC2					
<b>Decoder</b>					
DL5	Deconv2D-ReLU	3x3	1x1	256	16x16
UpSampling2D					
DL4	Deconv2D-ReLU	3x3	1x1	128	32x32
UpSampling2D					
DL3	Deconv2D-ReLU	3x3	1x1	64	64x64
UpSampling2D					
DL2	Deconv2D-ReLU	3x3	1x1	32	128x128
UpSampling2D					
DL1	Deconv2D-ReLU	3x3	1x1	16	256x256
UpSampling2D					
<b>Output (512x512) RGB image</b>					

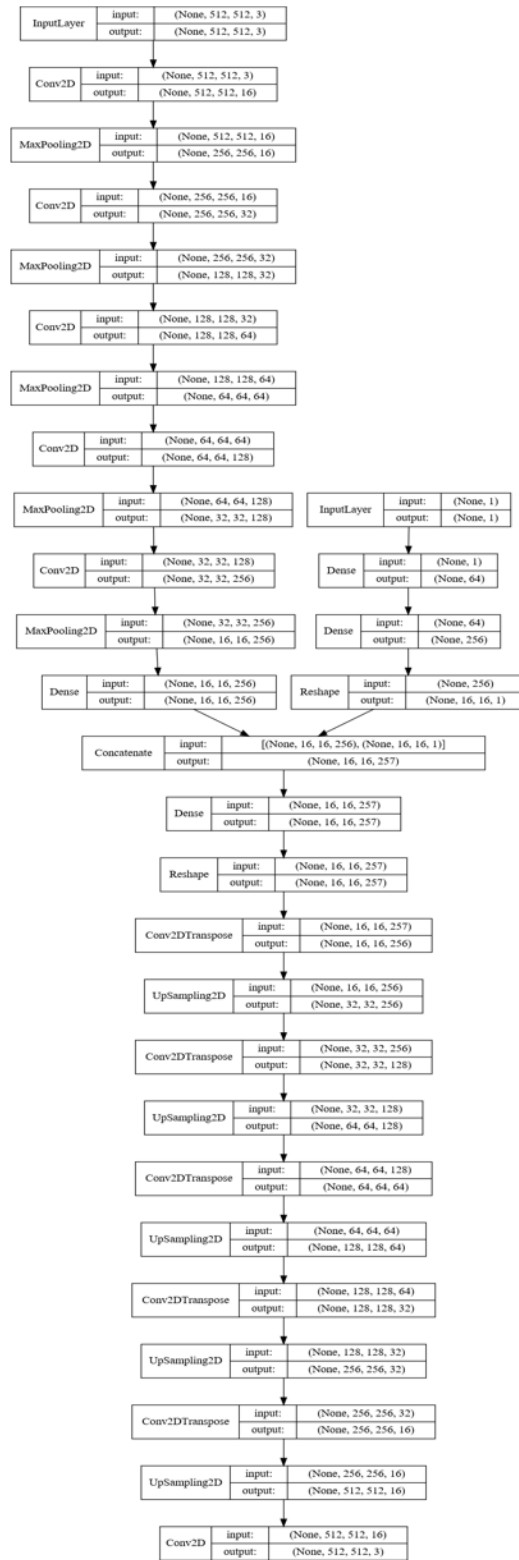


Figure 4- 3: Flowchart of the proposed model.

## **DATA COLLECTION AND PREPARATION**

### **5-1. Introduction**

This chapter describes the data collection and preparation processes for testing the developed UGPM model, considering three urban areas: the Dallas/Fort Worth (DFW) and two of its fast-growing counties, Collin and Denton. Each data set is in the form of a series of historical satellite images that were obtained from three different landsats as mentioned earlier in Chapter 3. This Chapter is organized as follows. Section 5-2 presents a brief description of the study areas. Section 5-3 illustrates the data structure used for training and validating the UGPM. Section 5-4 presents the preparation of the dataset that are used for model development. Finally, Section 5-5 describes the computation platform used in this study.

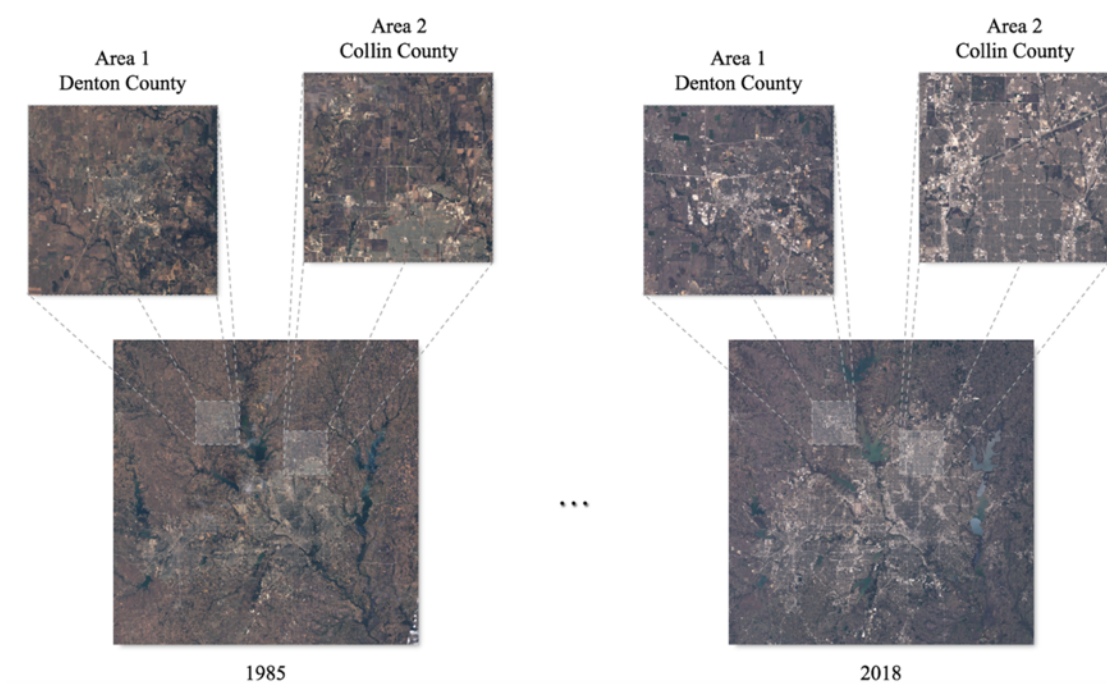
### **5-2. Study Area**

The model described in chapter 4 is applied to study the urban growth pattern for the entire DFW area and two of its fast-growing counties, Collin and Denton. Ranked among the five largest metropolitan areas in the U.S., DFW is also one of the fastest growing areas ([US Census Bureau, 2018](#)). Table 5-1 illustrates the Longitude and Latitude of the three study areas.

A population growth of more than one million people per decade has been reported for the past three decades for the DFW area. This growth is expected to continue as the area gained more new residents in 2018 than any other metropolitan area in the nation. According to recent U.S. Census Bureau data, the city's population, now more than 7.5 million, grew by nearly 132,000 people from 2017 to 2018, marking a 1.8 % increase. Located in the North Central Plains of Texas, DFW is largely flat with no mountains that restrict its growth from any direction. The region includes multiple lakes that cover about 10% of the area of DFW. Figure 5-1 shows satellite images for the study areas in 1985 and 2018, respectively, which depict the growth of these areas during that period.

**Table 5- 1: The longitude and latitude for the three study areas**

Study area		NW	NE	SW	SE	Area (mi <sup>2</sup> )
<b>DFW</b>	<b>Longitude Latitude</b>	97°29'34.40"W 33°30'34.39"N	96°23'4.54"W 33°30'34.39"N	97°29'34.40"W 32°24'18.58"N	96°23'4.54"W 32°24'18.58"N	4,896
<b>Collin County</b>	<b>Longitude Latitude</b>	96°53'43.03"W 33°13'50.29"N	96°34'8.57"W 33°13'50.29"N	96°53'43.03"W 32°54'18.17"N	96°34'8.57"W 32°54'18.17"N	425
<b>Denton County</b>	<b>Longitude Latitude</b>	97°23'2.77"W 33°30'42.71"N	96°50'24.50"W 33°30'42.71"N	97°23'2.77"W 32°58'6.37"N	96°50'24.50"W 32°58'6.37"N	1,179



**Figure 5- 1: Satellite images of the study areas showing their growth between 1985 and 2018.**








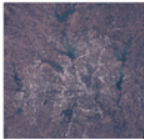
### **5-3. Data Structure for Training and Validating the Model**

Table 5-2 illustrates the structure used to store the data required for training and validating the UGPM described above. A separate dataset is prepared for each study area (i.e., DFW, Collin County and Denton County). Each data record, demonstrated as one column in the table, is defined in terms of the triplet  $I_x$ ,  $I_y$  and  $\Delta t$ , where  $I_x$  represents the input satellite image at time  $t_0$ ,  $I_y$  represents the output image at time  $t_0 + \Delta t$ , and  $\Delta t$  is the time difference in years between the two images. The two images  $I_x$  and  $I_y$  have the same resolution. Once the model is trained and validated, it can be used to construct the predicted image  $I_y$  for a given input pair  $I_x$  and  $\Delta t$ .



For the purpose of applying the model to predict the growth pattern for a given urban area,  $I_x$  is typically taken as the image of the current year. For the purpose of model validation and testing,  $I_x$  could be any image with time index  $t_0$  such that a subsequent image  $I_y$  with time index  $t_0 + \Delta t$  exists in the dataset. The image constructed by the model,  $\hat{I}_y$ , is then compared to the ground truth image,  $I_y$ , and their similarity measures (i.e., MSE and SSIM) are reported.

**Table 5- 2: Data structure for model training and validation**

<b>Image <math>I_x</math></b>	 1985	 1986	 1987	...	 Year $t_0$
<b>Image <math>I_y</math></b>	 1987	 1991	 1995	...	 Year $t_0 + \Delta_t$
<b>Horizon</b>	2 years	5 years	8 years	...	$\Delta_t$

#### 5-4. Data Preparation

To prepare this dataset, a series of historical satellite images for each study area is first collected. As mentioned earlier, high resolution images become available in year 1985 with the launching of Landsat 5. Thus, a past horizon that extends from 1985 to 2018 is considered. The clearest image in each quarter of each year is obtained. In cases where there are no clear images available for the quarter, an image from the next or previous quarters is borrowed for that quarter. Thus, four different streams of satellite images are obtained for each area. Each stream includes 34 images that represent the area's year-to-

year growth. Each stream resulted in 594 data records (combinations of  $I_x$ ,  $I_y$ ,  $\Delta t$ ). Combining the four streams together, a total of 2376 data records are obtained for each study area.

Two strategies are implemented to enlarge the size of this dataset. First, the above steps are repeated after rotating all images in the four stream  $180^\circ$  around the y-axis resulting in 4752 data points. Second, for each data stream, the data record in which  $I_x$  and  $I_y$  are both the images of the base year (i.e., year 2018 with  $\Delta t = 0$ ) is copied 100 times. The reason for replicating the data point representing the base year is to help the model learn the features of the base year as it is only included once in the original dataset. Adding the base year data records for all streams increases the size of the dataset to 5152. A random shuffling operation is then applied to ensure that images of the same year are not all falling in one training batch.

A split percentage of 80%-20% is used to obtain the training and validation datasets, respectively. While a limited theory exists on the data size requirements for developing a successful deep learning model, one should expect that the data size to depend on the application domain, which defines the number and complexity of the instances to be learned (Beleites et al., 2013). For example, a general-purpose video prediction model might require thousands or even millions of training instances to capture all possible objects and contexts. However, other applications such as predicting urban growth from satellite images are expected to require less data to train a CAE model and obtain a reasonable prediction accuracy.

## **5-5. Computational Platform**

A high-performance computing (HPC) cluster with graphics processing capabilities is used to train the model. The cluster includes 36 cores of NVIDIA P100 GPUs with 256 GB memory. It is worth mentioning that the resolution of the downloaded satellite images is in the range of 15,000x12,000. However, these high-resolution images cannot be used considering the limited memory of the used HPC platform.

After several trials to examine the highest resolution that can be used, the resolution of the original images was reduced to 512x512, which is the highest resolution that can be accommodated by the HPC platform. As this research focuses primarily on presenting a proof-of-concept of the idea of adopting VP technology for UGPM, the use of the reduced-resolution images is considered adequate. Of course, better results are expected if images with higher resolution are used, which could be achieved as a more advanced computing platform becomes available.

## **5-6. Summery**

This chapter describes the datasets that were collected and prepared for the purpose of training and validating the UGPM for three study areas: DFW, Collin County, and Denton County. The chapter presented a brief description of the study areas. It also described the data structure used for training and validating the developed UGPM.

## Chapter 6

### SENSITIVITY ANALYSIS AND RESULTS

#### 6-1. Introduction

In this chapter, we present a summary of the results of a sensitivity analysis that is conducted to determine the optimal values for the model parameters. The model described in chapter 4 is implemented using the Keras/TensorFlow platform. Keras is an open-source neural-network library that is written in Python and runs on top of TensorFlow, which is also an open-source software library that enables fast implementation of neural network models. The model is trained using different parameters, which are (a) number of epochs, (b) batch sizes, (c) optimizers, (d) data sizes, and (e) number of convolution/deconvolution layers in the CAE architecture.

#### 6-2. Values of Hyper-Parameters

This section shows the values that tested for each parameter as shown in Table 6-1. For example, number of epochs of 500, 1,000, 2,000, and 5,000 are considered. The number of batch sizes varies from 8 to 256. Six common optimizers including the Stochastic Gradient Decent (SGD), Adadelata, Adamax, Nadam, Adam, and Root Mean Square Propagation (RMSprop) are examined. Four datasets of different sizes are used for model training and validation with 80%-20% split. These datasets are: (I) basic dataset

resulting from combining the 35 images for each quarter for each year (2,376 data points); (II) the basic dataset in (I) plus the dataset obtained after rotating all images 180° around the y-axis (4,752 data points); (III) the basic dataset in (I) after adding 400 data points for the base year (2,776 data points); and (IV) the dataset in (II) after adding 400 data points for the base year (5,152 data points). Finally, different number of convolution and deconvolution layers are considered. We examined a model structure with 3, 4 and 5 layers in the encoder and the decoder, respectively. Larger number of layers are not considered as it is expected to result in an overfitting model considering the size of the available data.

**Table 6- 1: Values considered for the model parameters**

No. of epochs	500	1,000	2,000	5,000	
Batch size	8	16	32	64	128 256
Optimizer	SGD	Adadelata	Adamax	Nadam	Adam RMSprop
Dataset sizes	2,376	4,752	2,776	5,152	(80% training and 20% validation)
No. of CNN layers	3	4	5		

To evaluate the model prediction performance, the similarity between the predicted images and their corresponding ground truth images is examined. Considering year 1985 to be the base year, the model is used to predict the urban growth for years 1985 ( $\Delta t = 0$ ), 1990 ( $\Delta t = 5$ ), 1995 ( $\Delta t = 10$ ), and 2015 ( $\Delta t = 30$ ), respectively. For each target year, the similarity measures, MSE and SSIM, between the image constructed by the model and its corresponding actual image are reported. As mentioned earlier, while the SSIM is a normalized measure between zero and one, the MSE gives the total error between the two images.

### **6-3. Effect of Number of Epochs**

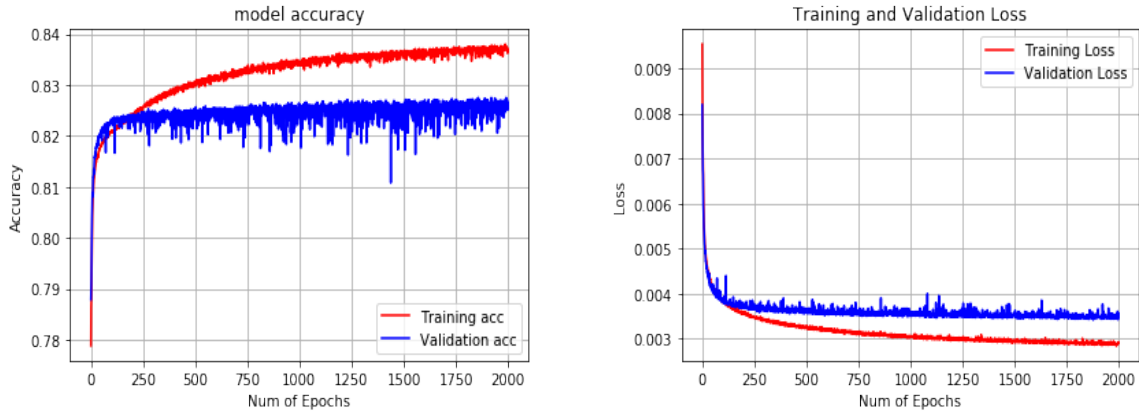
The first experiment examines the effect of the number of epochs on the model performance. In this experiment, the Adam optimizer is used for dataset IV with a batch size that is fixed at 32. The model accuracy and loss functions along with the run time in hours for each case are reported in Table 6-2. As shown in the table, increasing the number of epochs improves the model accuracy measure and reduces the value of loss function. For example, at 500 epochs, an accuracy of 0.8301 and a loss of 0.0033 are recorded after training. As the number of epochs is increased to 5,000, the accuracy improves to 0.8404 and the loss reduces to 0.0028. One can also notice that a lower accuracy and a higher loss are recorded when the model is validated.

The improvement in the model accuracy with the increase in the number of epochs comes with a substantial increase in the execution time, which jumped from 11.80 hours for 500 epochs to 109.72 hours for 5,000 epochs. Considering the trade-off between model accuracy and execution time, the case in which 2,000 epochs is adopted for all following experiments, which generally provides a good level of accuracy in a reasonable execution time.

Figure 6-1 shows the convergence pattern for the accuracy and loss measures during model training and validation, respectively, for the 2000 epoch case. As shown in the figures, the accuracy and the loss measures systematically improve with the increase in the number of epochs. As expected, the training results are better than those obtained during the validation of the model.

**Table 6- 2: The model performance for different number of epochs**

Number of Epochs	Training		Validation		Run Time (hrs.)
	Accuracy	Loss	Accuracy	Loss	
500	0.8301	0.0033	0.8239	0.0036	11.80
1,000	0.8350	0.0030	0.8266	0.0035	21.94
<b>2,000</b>	<b>0.8370</b>	<b>0.0029</b>	<b>0.8263</b>	<b>0.0035</b>	<b>43.33</b>
5,000	0.8404	0.0028	0.8254	0.0034	109.72



**Figure 6- 1: The convergence pattern of the model accuracy (left) and the loss (right) measures for 2000 epochs.**

The results of the model’s prediction performance are summarized in Table 6-3. The table gives the SSIM and the MSE for the four prediction scenarios mentioned above for different number of epochs. Several observations can be made based on the results in this table. First, a good level of similarity is recorded between the constructed and the actual images as the SSIM measure ranges from about 73% to 82% for the tested cases. Second, the SSIM measure tends to increase with increasing the number of epochs, while no clear pattern is observed for the MSE measure. Finally, there is no clear correlation pattern between the SSIM and the MSE measures as high SSIM values could be associated with low MSE, and vice versa. Thus, reporting both measures is critical to better evaluate the model’s prediction fidelity.

**Table 6- 3: The model prediction performance for different numbers of epochs.**

Compared Images	No. of Epochs							
	500 Epochs		1,000 Epochs		2,000 Epochs		5,000 Epochs	
	SSIM	MSE	SSIM	MSE	SSIM	MSE	SSIM	MSE
Actual (1985) Predicted @ $\Delta t = 0$	0.778	83,996	0.786	82,436	0.779	85,750	0.773	89,464
Actual (1990) Predicted @ $\Delta t = 5$	0.732	87,293	0.752	81,836	0.759	81,897	0.754	85,391
Actual (1995) Predicted @ $\Delta t = 10$	0.795	93,075	0.805	91,156	0.807	90,478	0.805	96,532
Actual (2015) Predicted @ $\Delta t = 30$	0.802	87,725	0.816	89,829	0.820	86,700	0.818	86,558

**6-4. Effect of Batch Size**

In the second experiment, we investigated the effect of the batch size on the performance of the model. The batch size was changed from 8 to 256, while the number of epochs was fixed at 2,000. In addition, the Adam optimizer and dataset IV are used. As shown in Table 6-4, the accuracy and loss values do not significantly vary as the batch size increases.

A batch size of 64 gives the highest accuracy value of 83.83% and the lowest loss value of 0.0029, compared to the other batch sizes. As for the run time, up to a batch size of 64, a run time of about 44 hours is required for model training. An increase in the run time is recorded with increasing the batch size. For example, using a batch size of 256, the run time jumps to about 49 hours. Based on these results, a batch size of 64 for model training is considered for the following experiments as it provides the highest accuracy and lowest loss within a reasonable run time.

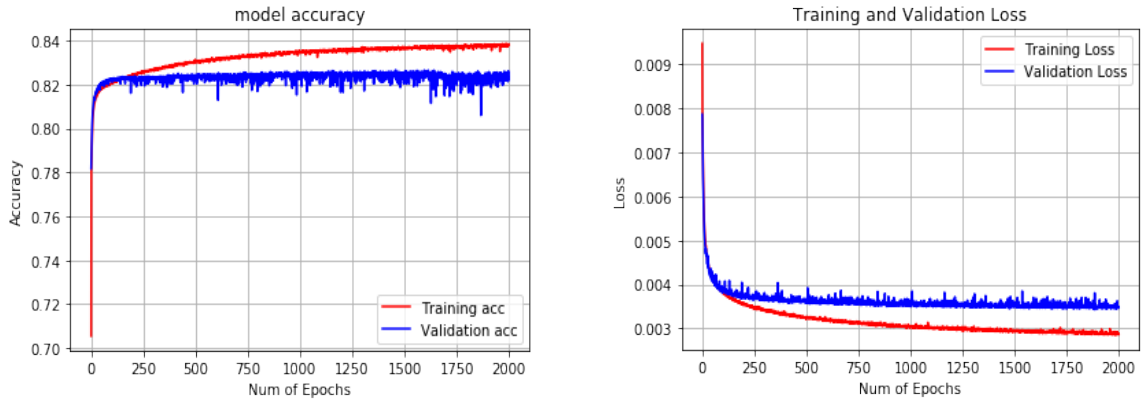
Figure 6-2 gives the convergence pattern for the accuracy and loss measures for the model training and validation, respectively, using a batch size of 64. Again, a lower



performance is recorded for model validation compared to that recorded during the model training.

**Table 6- 4: The model performance for different batch sizes**

Batch Size	Training		Validation		Run Time (hrs.)
	Accuracy	Loss	Accuracy	Loss	
8	0.8369	0.0029	0.8272	0.0035	43.78
16	0.8354	0.0030	0.8255	0.0035	43.80
32	0.8364	0.0030	0.8221	0.0035	43.61
<b>64</b>	<b>0.8383</b>	<b>0.0029</b>	<b>0.8231</b>	<b>0.0035</b>	<b>43.99</b>
128	0.8381	0.0029	0.8175	0.0037	43.81
256	0.8369	0.0029	0.8256	0.0036	49.02



**Figure 6- 2: The convergence pattern of the model accuracy (left) loss (right) for 64 batch size.**

Table 6-5 summarizes the results related to examining the model prediction performance considering different batch sizes. The SSIM and MSE resulting from comparing the actual and constructed images for the four different years mentioned above are given for all tested batch sizes. As shown in the table, consistent with the accuracy results presented above, high SSIM values, ranging from about 75% to 82%, are obtained for all years at a batch size of 64. Based on these results, we conclude that no clear pattern for the effect of the batch size on the MSE can be derived.

**Table 6- 5: The model prediction performance for different batch sizes.**

Compared Images	Batch Size					
	8		16		32	
	SSIM	MSE	SSIM	MSE	SSIM	MSE
Actual (1985) Predicted @ $\Delta t = 0$	0.784	82,363	0.778	84,931	0.779	84,390
Actual (1990) Predicted @ $\Delta t = 5$	0.753	81,474	0.750	81,094	0.748	86,446
Actual (1995) Predicted @ $\Delta t = 10$	0.804	92,845	0.803	93,631	0.798	97,539
Actual (2015) Predicted @ $\Delta t = 30$	0.817	86,138	0.812	89,945	0.819	88,605
Compared Images	64		128		256	
	SSIM	MSE	SSIM	MSE	SSIM	MSE
	Actual (1985) Predicted @ $\Delta t = 0$	0.778	86,815	0.781	86,534	0.782
Actual (1990) Predicted @ $\Delta t = 5$	0.754	84,554	0.744	87,722	0.754	80,788
Actual (1995) Predicted @ $\Delta t = 10$	0.806	94,881	0.796	98,539	0.805	93,649
Actual (2015) Predicted @ $\Delta t = 30$	0.819	88,519	0.814	91,864	0.816	88,012

**6-5. Examining the Performance of Different Optimizers**

As mentioned earlier, the model performance is examined considering several widely-used optimizers for the CAE's parameter estimation. In this set of experiments, dataset IV is used for model training and validation. In addition, the number of epochs and the batch size are set to be equal to 2,000 and 64, respectively. Table 6-6 provides a summary of the model performance results. As shown in the table, the Adamax optimizer recorded the highest accuracy value, 84.16%, and the lowest loss value, 0.0027.

On the other hand, the SGD optimizer recorded the lowest accuracy value, 78.69%, and the highest loss value, 0.0070. For the run time, all optimizers recorded close run times with the exception of RMSprop, which recorded a relatively higher run time. Although Adamax, Nadam and Adam are among the highest performing optimizers in terms of

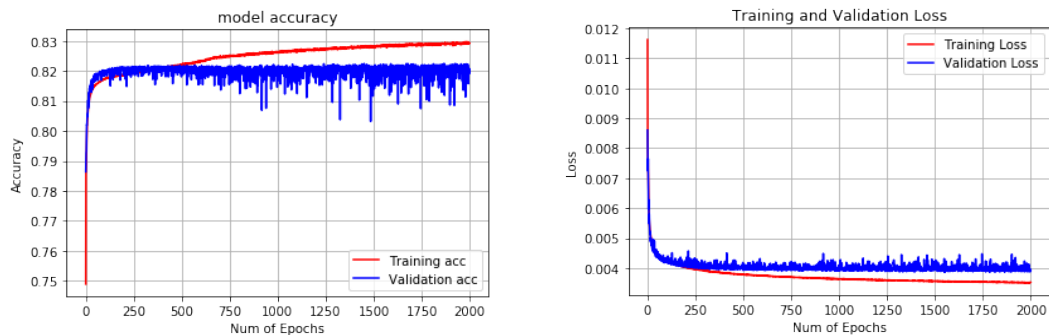
accuracy and loss values, their constructed images for the four prediction horizons mentioned above were found to include unexplained black spots. The size and number of these spots generally increases with the increase in the prediction horizon.

Visually examining the constructed images using the RMSprop optimizer shows that they do not include such spots. As RMSprop gives the highest accuracy and the lowest loss after those of Adamax, Nadam and Adam, the RMSprop is adopted for model development.

Figure 6-3 shows the convergence pattern for the accuracy and loss measures for the model training and validation, respectively, using the RMSprop optimizer. As shown in the figure, the accuracy systematically increases while the loss systematically decreases with the number of epochs. As expected, the validation performance is lower than that of the training performance.

**Table 6- 6: The model performance for different optimizers**

Optimizer	Training		Validation		Run Time (hrs.)
	Accuracy	Loss	Accuracy	Loss	
SGD	0.7869	0.0070	0.7886	0.0069	43.79
Adadelta	0.8164	0.0046	0.8181	0.0046	43.91
Adamax	0.8416	0.0027	0.8274	0.0033	43.74
Nadam	0.8300	0.0034	0.8227	0.0038	43.98
Adam	0.8390	0.0029	0.8286	0.0034	43.49
<b>RMSprop</b>	<b>0.8292</b>	<b>0.0035</b>	<b>0.8192</b>	<b>0.0039</b>	<b>46.14</b>



**Figure 6- 3: The convergence pattern of the model accuracy (left) and loss (right) for the**

**RMSprop optimizer.**

## 6-6. Effect of Data Size for Model Training

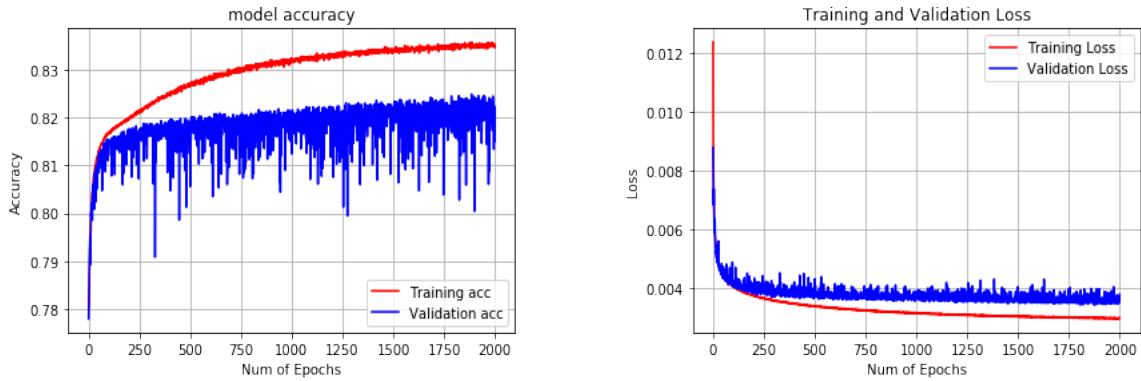
In this set of experiment, we examine the effect of the training data size on the performance of the model. As mentioned earlier, four datasets with different sizes are considered. These experiments are performed using the RMSprop optimizer while fixing the number of epochs and the batch size at 2,000 and 64, respectively.

Table 6-7 provides a summary of the performance measures for these experiments. As shown in the table, the model trained with dataset III produced the highest performance in terms of accuracy and loss values. For example, using the training data, an accuracy of 83.47% and a loss of 0.003 are recorded using this dataset. Despite being the smallest, dataset I (basic dataset) is also shown to produce a model with comparable performance to the other datasets.

Thus, while enlarging the data size by rotating the original images is a common practice used for training computer vision models ([Stallkamp et al., 2012](#); [Defferrard et al., 2016](#); [Masi et al., 2016](#)), such practice does not seem to benefit the UGPM as no improvements in the model performance are recorded. One can also observe the increase in the run time associated with increasing the size of the used dataset. For example, run times of 20.30 hrs. and 23.60 hrs. are recorded for datasets I and III, respectively. The run time jumped to 40.00 hrs. and 46.14 hrs. using dataset II and IV, respectively. Based on these results, dataset III is used to develop the model. Figure 6-4 gives the convergence pattern for the accuracy and loss measures using dataset III. The convergence pattern is similar to those of the previous experiments presented above.

**Table 6- 7: The model performance for different data sizes**

Dataset (size)	Training		Validation		Run Time (hrs.)
	Accuracy	Loss	Accuracy	Loss	
I – (2,376)	0.8269	0.0030	0.8127	0.0038	20.30
II – (4,752)	0.8268	0.0035	0.8040	0.0042	40.00
<b>III – (2,776)</b>	<b>0.8347</b>	<b>0.0030</b>	<b>0.8151</b>	<b>0.0038</b>	<b>23.60</b>
IV – (5,152)	0.8292	0.0035	0.8192	0.0039	46.14



**Figure 6- 4: The convergence pattern of the model accuracy (left) and loss (right) using dataset III.**

### 6-7. Effect of Different Model Structures

In this set of experiment, we investigated the performance of different model structures with respect to the number of convolution and deconvolution layers in the CAE architecture. Five model structures are compared as described in Table 6-8. As shown in the table, the base model has five convolution and five deconvolution layers (see Table 4-1) with a total number of parameters that is equal to 1,526,213. For both Model 1 and Model 2, four convolution and four deconvolution layers are considered (see Table 6-10 and 6-11). Compared to the base model, CL5 and DL5 are eliminated in Model 1 resulting in 607,045 parameters, and CL1 and DL1 are eliminated in Model 2 resulting in 1,517,829 parameters. Model 3 and Model 4 are constructed using three convolution layers and three

deconvolution layers (see Table 6-12 and 6-13). Model 3 includes convolution layers CL1, CL2 and CL3 and deconvolution layers DL1, DL2 and DL3 with a total number of parameters that is equal to 294,917. Model 4 includes convolution layers CL1, CL3 and CL5 and deconvolution layers DL1, DL3 and DL5 with a total number of parameters that is equal to 1,055,877.

These experiments are performed using the RMSprop optimizer for dataset III while fixing the number of epochs and the batch size at 2,000 and 64, respectively. The results of this set of experiments are given in Table 6-9. As shown in the table, despite the increase in the running time, increasing the number of layers significantly improves the model performance.

The base model (Model 0) gives the highest performance with accuracy and loss measures of 0.8347 and 0.0030, respectively. The lowest performance is recorded for Model 3, which has 0.8186 accuracy and 0.0031 loss values. Model 4 recorded a good performance in terms of accuracy and loss values compared to the base model. However, examining the images constructed by both models, the base model produced images with higher quality than those produced by Model 4.

**Table 6- 8: Summary of five model structures with different number of layers**

Model	No. of layers (E-D)	Used layer (kept)		No. of parameters
		Encoder (Conv.)	Decoder (Deconv.)	
Model 0 Base Model	5	See Table 4- 1		1,526,213
Model 1	4	CL1, CL2, CL3, CL4	DL1, DL2, DL3, DL4	607,045
Model 2	4	CL2, CL3, CL4, CL5	DL2, DL3, DL4, DL5	1,517,829
Model 3	3	CL1, CL2, CL3	DL1, DL2, DL3	294,917
Model 4	3	CL1, CL3, CL5	DL1, DL3, DL5	1,055,877

**Table 6- 9: The performance of different model structures**

Model	Training		Validation		Run Time (Hrs.)
	Accuracy	Loss	Accuracy	Loss	
<b>Model 0</b>	<b>0.8347</b>	<b>0.0030</b>	<b>0.8151</b>	<b>0.0038</b>	<b>23.60</b>
<b>Base Model</b>					
Model 1	0.8194	0.0033	0.8061	0.0038	05.56
Model 2	0.8324	0.0023	0.8198	0.0028	07.22
Model 3	0.8186	0.0031	0.8135	0.0036	01.40
Model 4	0.8319	0.0021	0.8235	0.0024	01.41

Based on the results of the sensitivity analysis presented above, the best performance of the UGPM is achieved for the model when an architecture with five convolution layers and five deconvolution layers is considered. This model is trained using dataset III and the RMSprop optimizer with 2,000 epochs and 64 batch size. Figure 6-5 shows the constructed images for the four prediction horizons mentioned above and compares them with their corresponding actual ones.

Assuming year 1985 as the base year, the model constructed images for horizons that are equal to zero, 5, 10 and 30 years, respectively. For each pair of images, the SSIM and the MSE similarity measures are given. The values of the SSIM, which are greater than 70% for all tested cases, suggest that the model is able to construct images that are close to the actual ones. Also, visually examining the constructed images, they capture the main features of their corresponding ground-truth ones.

**Table 6- 10: Model 1 dimensions of the different layers of the encoder-decoder architecture**

Layer ID	Layer type/ Activation	Kernel size	Strides	Filter	Spatial input size
<b>Encoder</b>					
<b>Input 1 (512x512) RGB image</b>					
CL1	Conv2D-ReLU	3x3	1x1	16	512x512
MaxPooling2D					
CL2	Conv2D-ReLU	3x3	1x1	32	256x256
MaxPooling2D					
CL3	Conv2D-ReLU	3x3	1x1	64	128x128
MaxPooling2D					
CL4	Conv2D-ReLU	3x3	1x1	128	64x64
MaxPooling2D					
FC1					
<b>Input 2 (Time)</b>					
FC0' (time)					
FC1' (time)					
Concatenate (FC1, FC1' (time))					
FC2					
<b>Decoder</b>					
DL4	Deconv2D-ReLU	3x3	1x1	128	32x32
UpSampling2D					
DL3	Deconv2D-ReLU	3x3	1x1	64	64x64
UpSampling2D					
DL2	Deconv2D-ReLU	3x3	1x1	32	128x128
UpSampling2D					
DL1	Deconv2D-ReLU	3x3	1x1	16	256x256
UpSampling2D					
<b>Output (512x512) RGB image</b>					



**Table 6- 11: Model 2 dimensions of the different layers of the encoder-decoder architecture**

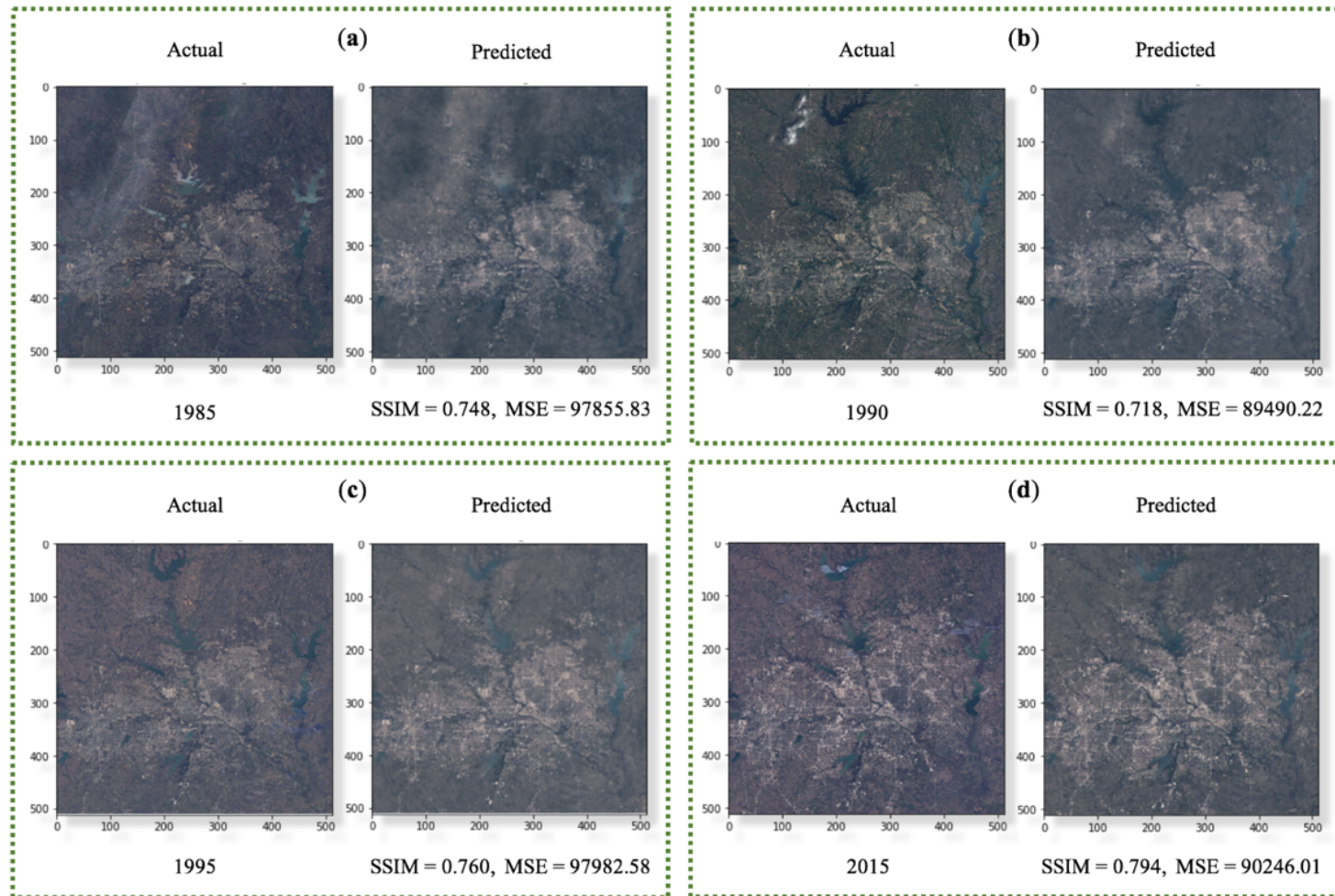
Layer ID	Layer type/ Activation	Kernel size	Strides	Filter	Spatial input size
<b>Encoder</b>					
<b>Input 1 (512x512) RGB image</b>					
CL2	Conv2D-ReLU	3x3	1x1	32	256x256
MaxPooling2D					
CL3	Conv2D-ReLU	3x3	1x1	64	128x128
MaxPooling2D					
CL4	Conv2D-ReLU	3x3	1x1	128	64x64
MaxPooling2D					
CL5	Conv2D-ReLU	3x3	1x1	256	32x32
MaxPooling2D					
FC1					
<b>Input 2 (Time)</b>					
FC0' (time)					
FC1' (time)					
Concatenate (FC1, FC1' (time))					
FC2					
<b>Decoder</b>					
DL5	Deconv2D-ReLU	3x3	1x1	256	16x16
UpSampling2D					
DL4	Deconv2D-ReLU	3x3	1x1	128	32x32
UpSampling2D					
DL3	Deconv2D-ReLU	3x3	1x1	64	64x64
UpSampling2D					
DL2	Deconv2D-ReLU	3x3	1x1	32	128x128
UpSampling2D					
<b>Output (512x512) RGB image</b>					

**Table 6- 12: Model 3 dimensions of the different layers of the encoder-decoder architecture**

Layer ID	Layer type/ Activation	Kernel size	Strides	Filter	Spatial input size
<b>Encoder</b>					
<b>Input_1 (512x512) RGB image</b>					
CL1	Conv2D-ReLU	3x3	1x1	16	512x512
MaxPooling2D					
CL2	Conv2D-ReLU	3x3	1x1	32	256x256
MaxPooling2D					
CL3	Conv2D-ReLU	3x3	1x1	64	128x128
MaxPooling2D					
FC1					
<b>Input_2 (Time)</b>					
FC0' (time)					
FC1' (time)					
Concatenate (FC1, FC1' (time))					
FC2					
<b>Decoder</b>					
DL3	Deconv2D-ReLU	3x3	1x1	64	64x64
UpSampling2D					
DL2	Deconv2D-ReLU	3x3	1x1	32	128x128
UpSampling2D					
DL1	Deconv2D-ReLU	3x3	1x1	16	256x256
UpSampling2D					
<b>Output (512x512) RGB image</b>					

**Table 6- 13: Model 4 dimensions of the different layers of the encoder-decoder architecture**

Layer ID	Layer type/ Activation	Kernel size	Strides	Filter	Spatial input size
<b>Encoder</b>					
<b>Input_1 (512x512) RGB image</b>					
CL1	Conv2D-ReLU	3x3	1x1	16	512x512
MaxPooling2D					
CL3	Conv2D-ReLU	3x3	1x1	64	128x128
MaxPooling2D					
CL5	Conv2D-ReLU	3x3	1x1	256	32x32
MaxPooling2D					
FC1					
<b>Input_2 (Time)</b>					
FC0' (time)					
FC1' (time)					
Concatenate (FC1, FC1' (time))					
FC2					
<b>Decoder</b>					
DL5	Deconv2D-ReLU	3x3	1x1	256	16x16
UpSampling2D					
DL3	Deconv2D-ReLU	3x3	1x1	64	64x64
UpSampling2D					
DL1	Deconv2D-ReLU	3x3	1x1	16	256x256
UpSampling2D					
<b>Output (512x512) RGB image</b>					



**Figure 6- 5: Comparison between the actual image and the predicted (constructed) images for different prediction horizons considering year 1985 as the base year.**

## **6-8. Summary**

Based on the results of the sensitivity analysis presented in this chapter, the best performance of the UGPM is achieved for the model when an architecture with five convolution layers and five deconvolution layers is considered. This model is trained using dataset III and the RMSprop optimizer with 2,000 epochs and 64 batch size. The values of the SSIM, which are greater than 70% for all tested cases, suggesting that the model is able to construct images that are close to the actual ones. Also, visually examining the constructed images, they capture the main features of their corresponding ground-truth ones.

## **MODEL APPLICATION FOR THE DALLAS-FORT WORTH REGION**

### **7-1. Introduction**

In this chapter, we present the results of applying the model presented above to study urban growth in the DFW area and two of its fast-growing counties (Colling County and Denton County). In addition to developing a model for the entire DFW (i.e., using the satellite images for the entire DFW area for model training and validation), two other models are developed. The first model covers the southwest part of Collin County while the second model covers most of Denton County. These two models are developed using the settings defined in chapter 6 (CAE model with five convolution and five deconvolution layers, RMSprop optimizer, dataset III, 2000 epochs and 64 batch size). Also, they were investigated more by using two cases: (1) with Transfer Learning (TL) and (2) without Transfer Learning (TL). In addition, these models are used to predict the urban growth pattern in their corresponding areas. We validated the output of growth pattern predicted through the developed models, by comparing it against the growth pattern predicted by the North Central Texas Council of Government (NCTCOG).

This chapter is organized as follows. Section 7-2 describes the model development effort for Collin County model and Denton County model. Section 7-3 presents the validation of the result of the UGPM with North Central Texas Council of Government (NCTCOG). Finally, Section 7.4 gives a summary of the chapter.

## 7-2. Model Development for Collin County and Denton County

Two cases are considered for developing these two modes: (I) with TL and (II) without TL. In the first case, the parameter values obtained for the DFW model are used as the initial values for the parameters of the models developed for Collin County and Denton County, respectively. In addition, the parameter values obtained for the Collin County model are used as the initial values for the parameters of the models developed for Denton County, and vice versa. In the second case, the model parameters are initialized randomly.

**Table 7- 1: The accuracy and loss recorded at the start and the end of the training process**

Area	Model	Model							
		Collin County				Denton County			
		At the start of the training process		At the end of the training process		At the start of the training process		At the end of the training process	
		Accuracy	Loss	Accuracy	Loss	Accuracy	Loss	Accuracy	Loss
Collin	Without TL	--	--	--	--	0.6248	0.0126	0.7996	0.0027
	With TL	--	--	--	--	0.7215	0.0073	0.7955	0.0098
Denton	Without TL	0.5941	0.0147	0.7656	0.0042	--	--	--	--
	With TL	0.6360	0.0117	0.7540	0.0049	--	--	--	--
DFW	Without TL	0.5941	0.0147	0.7656	0.0042	0.6248	0.0126	0.7996	0.0027
	With TL	0.6484	0.0112	0.7592	0.0046	0.7212	0.0069	0.7953	0.0028

Table 7-1 gives the values of the accuracy and loss measures recorded at the start and at the end of the training process with and without TL for the Collin County model and the Denton County model, respectively. As shown in the table, the adopted TL strategy has not improved the performance of the models developed for the two counties. While the transferred parameters resulted in a higher accuracy and less loss at the beginning of the training process for both models, these initial improvements are diminished by the end of the training process. The case without TL resulted in a slightly higher accuracy and less loss compared to those obtained in the case with transfer learning. This exercise is an example of negative transfer in which the model performance decreases when TL is used.

Hence, the models developed without TL are applied for predicting the growth in their corresponding counties.

Similar to the DFW model evaluation presented above, the performance of these two models are evaluated by comparing their constructed images with the corresponding actual images for different past years. Table 7-2 gives the SSIM and the MSE values resulting from comparing the actual images with their corresponding constructed images using the DFW model, the Collin County model and the Denton County model, respectively. The results are given for years 1985, 1990 and 2015. As shown in the table, all models recorded SSIM values that are greater than 70%. In addition, the model for Denton County recorded a relatively higher SSIM values that are greater than 80%.

**Table 7- 2: The prediction performance of the three developed models**

Compared Images	DFW		Collin County		Denton County	
	SSIM	MSE	SSIM	MSE	SSIM	MSE
Actual (1985)	0.748	97,855	0.753	81,061	0.814	91,800
Predicted @ $\Delta t = 0$						
Actual (1990)	0.718	89,490	0.707	82,425	0.807	70,595
Predicted @ $\Delta t = 5$						
Actual (1995)	0.760	97,982	0.768	91,698	0.822	85,212
Predicted @ $\Delta t = 10$						
Actual (2015)	0.794	90,246	0.764	97,153	0.825	85,076
Predicted @ $\Delta t = 30$						

These three models are used to predict the urban growth pattern in their corresponding areas. Considering year 2018 as the base year, the urban growth patterns for target years 2021, 2023, and 2025, respectively, are obtained by constructing an image for each target year. While the model can cover longer horizons, the dataset prepared for model training (combinations of  $I_x, I_y, \Delta t$ ) is expected to have more observations with small  $\Delta t$  values compared to those obtained for large  $\Delta t$  values. Thus, we select a prediction horizon

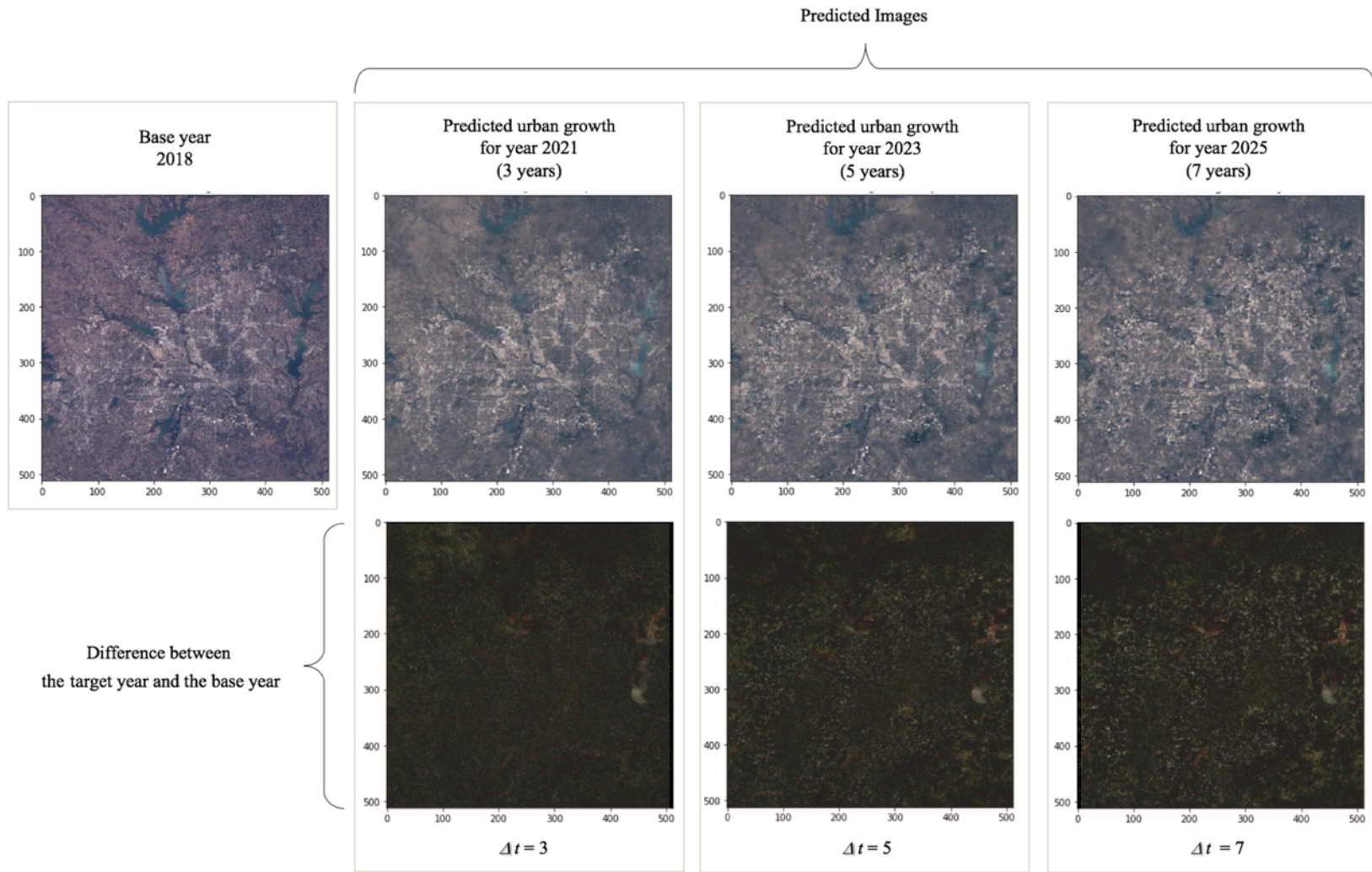


$\Delta t = 7$  is considered as it captures the tradeoff between using longer prediction horizons and having enough observations in the data to adequately learn the growth pattern for that horizon. Figures 7-1 to 7-3 show the constructed images for the three considered target years for DFW, Collin County and Denton County, respectively. In addition, to illustrate the growth in each area, the figures depict the difference between each constructed image and the image of the base year. These images give the locations of the growth predicted by the model for each target year.

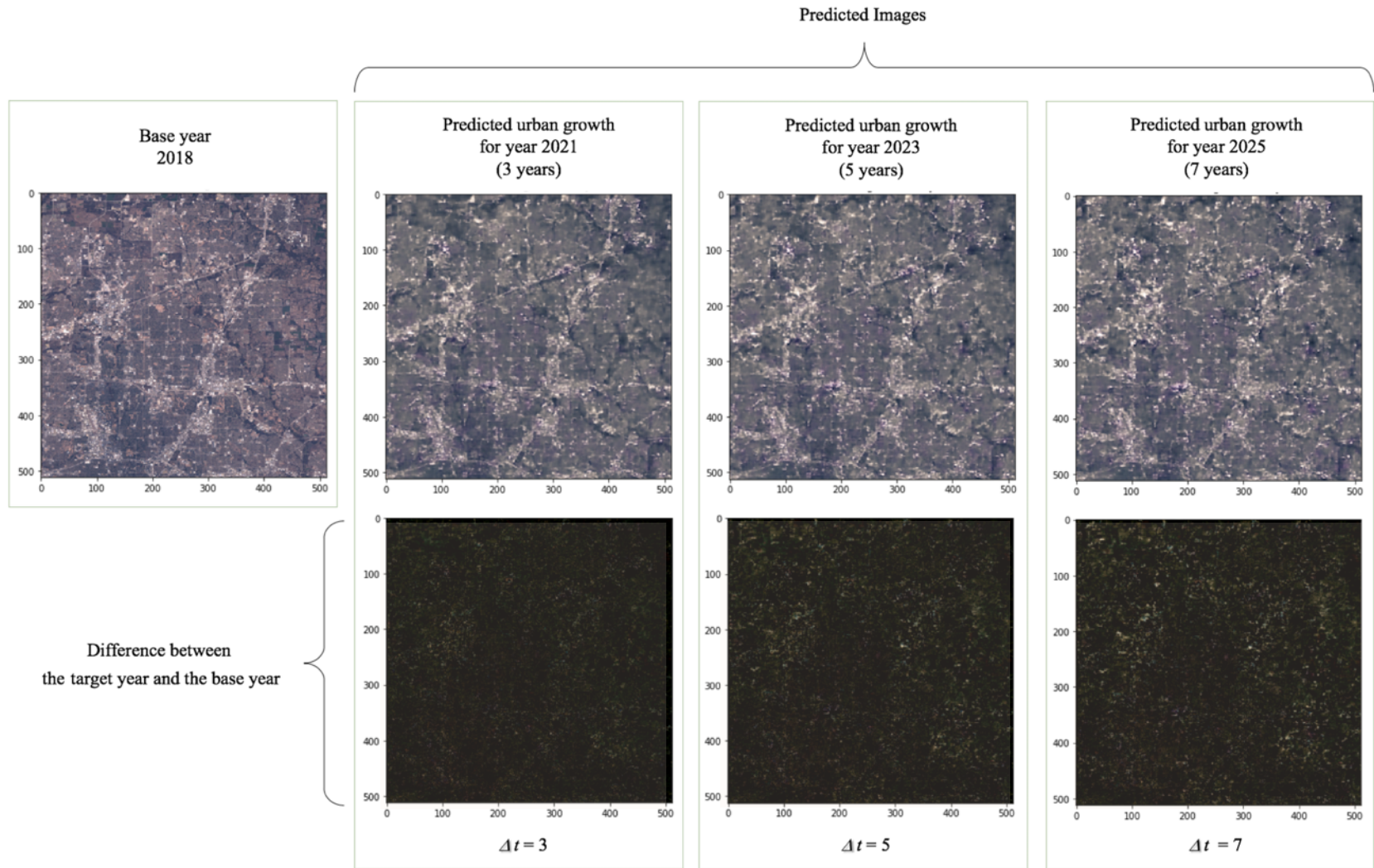
Several observations can be made based on the obtained predictions. First, the amount of growth is proportional to the length of the prediction horizon. As the length of the prediction horizon increases, more growth is depicted compared to the base year. This pattern is observed for all three studied areas, which indicates that they will be subject to a steady growth during the next few years. Second, the models are able to determine the boundaries of the developed region(s) within each studied area, and hence the growth is predicted to occur mostly outside these core regions. In addition, the models are able to identify areas that are naturally ineligible for development such as lakes. For the DFW area, all lakes are identified as no-growth areas. Third, each study area has its unique growth pattern. For example, for the entire DFW area, more growth is observed to occur on the north side and northeast sides compared to that occurring in the south side of the region. One can expect this predicted growth pattern considering the very slow development historically observed in the area south of the Trinity River.

For Collin County, it falls on the northern borders of the City of Dallas (just northeast of Dallas County), where most of its southeast corner (i.e., the border with Dallas County) is well-developed. Thus, the growth is predicted to occur mostly in the north and

northeast directions. Finally, Denton County is located northwest of Dallas County. The growth for Denton County is predicted to occur in the south and the east sides of the county. The growth direction tends to connect the developed area in Denton County with those in Dallas County to the southwest corner of Collin County, respectively.



**Figure 7- 1: Urban growth prediction for the DFW area after three, five, and seven years considering 2018 as the base year.**



**Figure 7- 2: Urban growth prediction for Collin County after three, five, and seven years considering 2018 as the base year.**

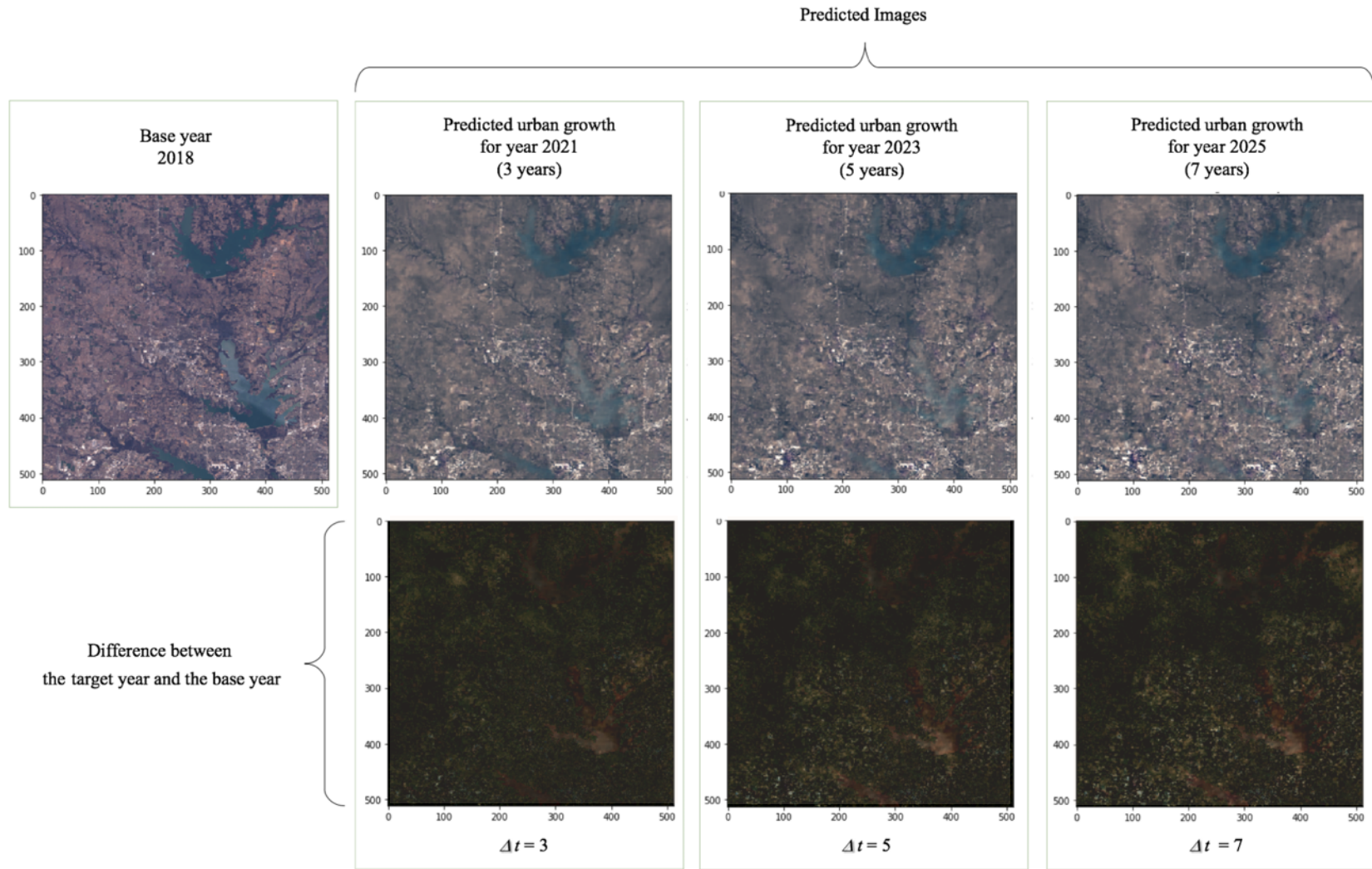


Figure 7- 3: Urban growth prediction for Denton County after three, five, and seven years considering 2018 as the base year.

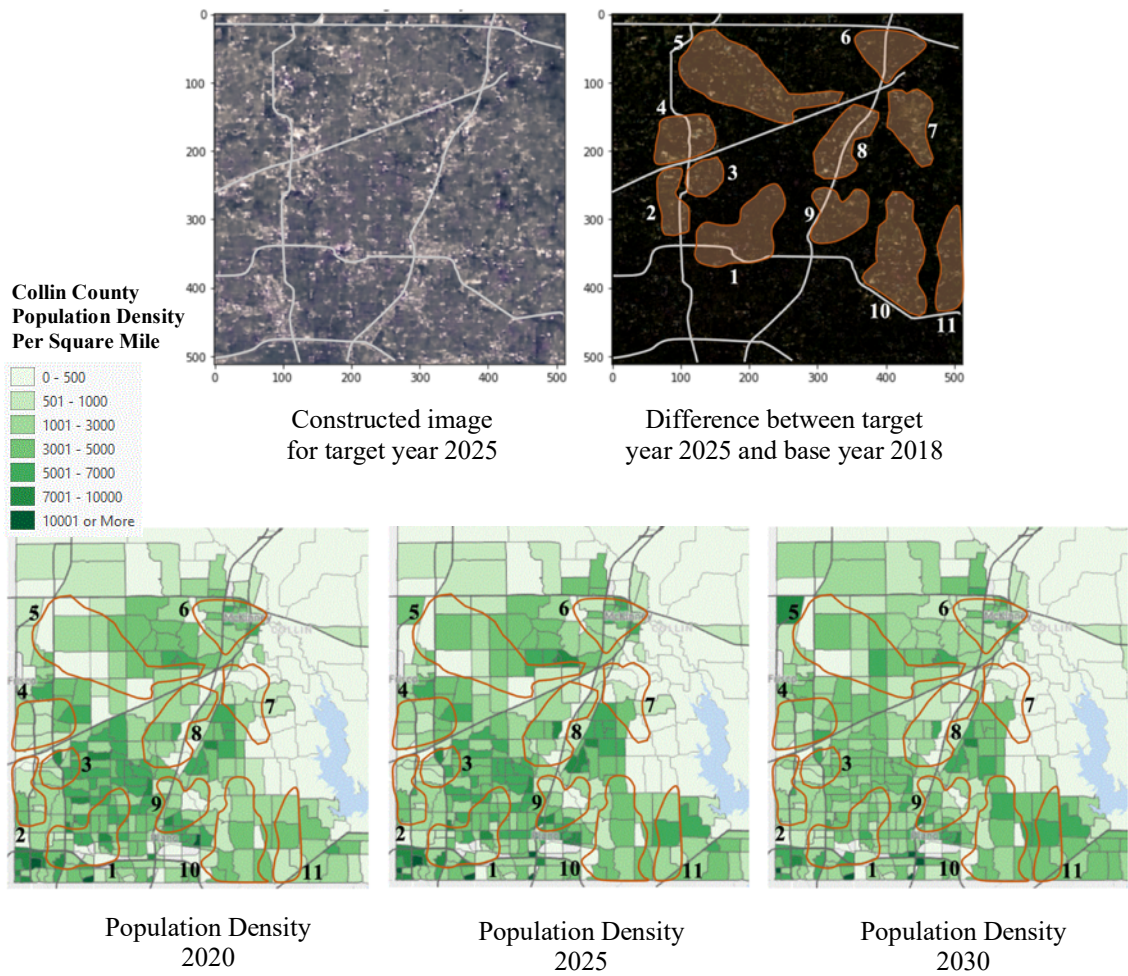
### **7-3. Validation the Model Result with North Central Texas Council of Government (NCTCOG)**

To further validate the accuracy of the growth pattern predicted using the developed models, their output is compared against the growth pattern predicted by North Central Texas Council of Government (NCTCOG), the metropolitan planning organization for the DFW area. The prediction provided by NCTCOG is in the form of population density maps. Figure 7-4 presents the results of this comparison for Collin County, while Figure 7-5 presents the results for Denton County.

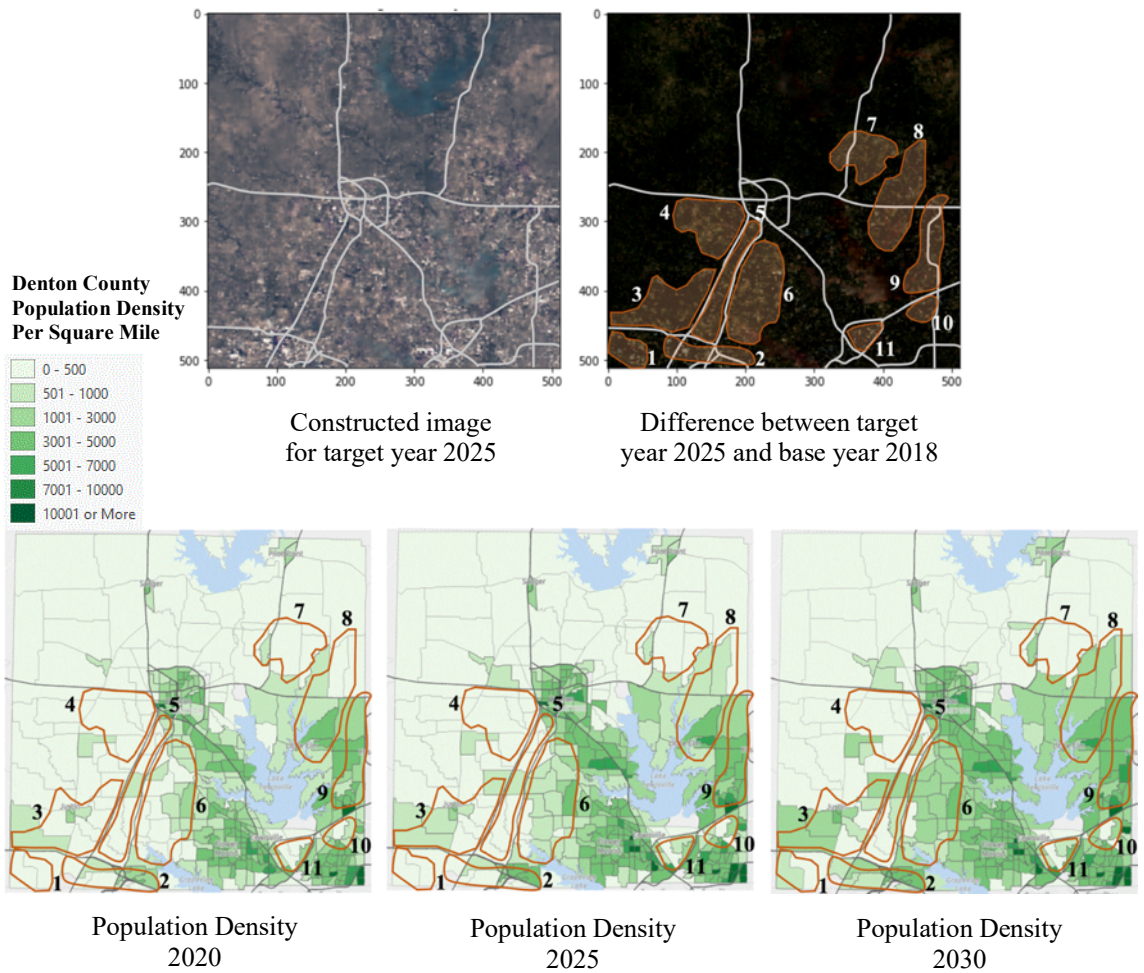
To perform this comparison, we first identify the zones in both counties that are predicted to experience growth in target year 2025. These zones are then superimposed on the corresponding population density map obtained from NCTCOG. If the superimposed zones are characterized by a significant change in the population density, it implies that the developed UGPM models are producing consistent results with NCTCOG growth prediction. Of course, one should not expect perfect match between the prediction pattern produced by the model and those obtained from NCTCOG, which themselves need to be verified.

For example, eleven zones with notable growth are identified for Collin County. Superimposing these zones on the population density maps of Collin County shows that most of these zones (4, 5, 7, 8, 10 and 11) are falling in areas that are predicted to also have a growth in their population densities. Similarly, for Denton County, eleven zones with significant growth are identified based on the results of the developed UGPM. Several of these zones (2, 3, 5, 6, 8, 9, and 10) have shown a predicted growth pattern that consistent with NCTCOG's growth prediction. These results illustrate that the approach introduced

in this research is an effective approach to develop UGPMs with high fidelity as it overcomes limitations of most existing approaches that require intensive data and model specification effort to obtain good results.



**Figure 7- 4: Model validation for Collin County by comparing the predicted urban growth with NCTCOG’s population growth prediction.**



**Figure 7- 5: Model validation for Denton County by comparing the predicted urban growth with NCTCOG’s population growth prediction.**

#### **7-4. Model Limitations**

Several limitations could be identified for the model based on its application results presented above. First, the value of the results depends mainly on the quality of the satellite images that are used to cover the horizon of interest. For example, the satellite image should



be clear to show the contrast between the undeveloped and developed areas. Failing to clearly present that contrast could affect the quality of the prediction. In addition, we have noticed inconsistency in the color pattern of the satellite images recorded in different periods (e.g., two consecutive month). This could be due to the time of day and/or the prevailing weather conditions at which the satellite image was recorded. This inconsistency in the pixel colors could negatively impact the model's ability to learn the land cover change. Of course, one expects these issues to be addresses with advancement in high resolution cameras used for satellite imaging and the availability of high-quality aerial photos.

Second, the variety of the color of the pixels in a monthly satellite image. This variety of the color from image to image, effect on the prediction results. For example, when downloading the satellite images for monthly bases with RGB color, some of the images have different pixel colors. This depends on the time that the satellite recorded the images (in the early morning or in the evening). In addition, some of these images are not only diverse in pixel color, but they are considered unclear in cases where they were recorded on a cloudy day.

Third, similar to most image processing applications, there is a trade off between the resolution of the images used to train model and the quality of the results. The use of high-resolution images is expected to provide superior prediction quality. However, using the high-resolution images would require high computational resources, which might not be available. In our study, we started using the original satellite images with a resolution of  $15,000 \times 12,000$ . However, these high-resolution images could not be used directly considering the limited memory of the used HPC platform. Thus, the resolution of these

satellite images was gradually reduced to a resolution of  $512 \times 512$ . The computational platform was able to process these images with a training time of repetitive use of process about two days.

Finally, the quality of the prediction is expected to be higher for shorter horizons compared to that of longer horizons. The reason is that the dataset includes more training examples for short horizons than for long horizons. Based on our analysis, the best prediction results are obtained for horizons that are in the range of one quarter to one third of the time difference between the oldest and the most recent image in the training data set. For instance, the images in the dataset used in the application described above are recorded between 1985 and 2018. For this case and based on the conducted validation, the highest quality prediction results are obtained when a horizon in the range of 7 years is considered.

#### **7-5. Summary**

The chapter presents the results of applying the model presented above to study urban growth in the DFW area and two of its fast-growing counties (Colling County and Denton County). In addition to developing a model for the entire DFW (i.e., using the satellite images for the entire DFW area for model training and validation), two other models are developed. The first model covers the southwest part of Collin County while the second model covers most of Denton County. Several observations can be made based on the obtained results: (1) the amount of growth is proportional to the length of the prediction horizon for all three studied areas, (2) the models are able to determine the boundaries of the developed region(s) within each studied area, (3) unique growth pattern has observed in each study area. For example, DFW area observed more growth occur on

the north side and northeast sides compared to that occurring in the south side of the region. In addition, to validate our developed model, we compared our results of the growth pattern with the growth pattern predicted by North Central Texas Council of Government (NCTCOG). These results illustrate that the approach introduced in this research could be effective in developing UGPMs.

**MODEL APPLICATION FOR THE MIDDLE EAST AND NORTH AFRICA  
(MENA) REGION**

**8-1. Introduction**

Many urban areas around the globe have reported significant growth rates over the past few decades. The average urbanization rate is estimated to reach more than 50% in most cities by 2050 (Zhou and Chen, 2018). This high rate of urbanization presents substantial stresses to these cities' ecological and financial resources as well as the overall well-being of their residents. Therefore, there are increasing calls to study urban growth, especially in developing countries where this growth is less controlled and could be associated with many undesirable consequences including the formation of slums, high unemployment rates, lack of infrastructure services (e.g., clean water, sewage, transportation, etc.), and vulnerability to epidemic diseases, to name a few.

This chapter presents the application of the UGPM presented in Chapter 4 for five MENA cities. As mentioned earlier, the purpose of urban growth studies is to identify locations and directions of potential growth, assess infrastructure and public service needs, and ensure the integration of new developments with the existing city structure. In addition, urban growth has been studied for deriving effective policies that help achieve sustainable and economically-sound growth patterns.

The model is applied to predict the urban growth of five MENA cities including Dubai (United Arab Emirates (UAE)), Cairo (Egypt), Doha (Qatar), Casablanca (Morocco), and Riyadh (Kingdom of Saudi Arabia (KSA)). These selected cities vary in terms of their size, population, historical heritage, level of control applied to their growth, geographical locations, complexity of their structure, and socio-economic characteristics.

For example, Cairo is one of the oldest and largest cities in the MENA region. Founded in 969 AD, the city is located at the fork of the Nile's Delta which expands over 175 square miles with a total population of about 20.5M. On the other side of the spectrum, the City of Doha is located on the Gulf coast, which was founded in 1820 and declared as Qatar's capital in 1971, and has an area of 51 square miles with a population that is close to 0.65M. Egypt and Qatar differ significantly in terms of their GDP. While an average GDP per capita of about \$2,600 is reported for Egypt, Qatar's average GDP per capita is near \$70,400 (Plecher, 2019).

This chapter is organized as follows. Sections 8-2 and 8-3 provides an overview of the MENA region and the list of cities selected for this study. Section 8-4 reviews the urban growth studies for selected MENA cities. The application of the model to predict the growth pattern for the selected MENA cities is then presented in Section 8-5. Finally, Section 8-6 concludes with a discussion on best practices to achieve sustainable urban growth for the MENA region.

## **8-2. Urban Growth Acceleration in the MENA Region**

The Middle East and North Africa (MENA) is one particular region that is characterized by significant urban growth during the past few decades (Gouda et al., 2016).

MENA's total population has grown from around 100 million in 1950 to nearly 578 million in 2018, with around 70% of this population concentrated in urban areas ([Statista Research Department, 2020](#)).

Several factors have contributed to this expedited urban growth in the MENA region. For example, most MENA countries very high birth rates compared to the rest of the world. The birth rates of most MENA countries are in the upper 20s per 1000 capita, compared to less than 10 births per 1000 capita in most western European countries. In addition, intensive migration from rural to urban areas has occurred in most MENA cities over the years.

The modernization of the agriculture sector has pushed for massive population movement seeking alternative economic opportunities in urban areas. Furthermore, the political instability followed the Arab Spring events in 2011 have also forced migration from war zones in countries like Iraq, Syria, Libya and Yemen to safer cities in the region. For example, the City of Amman, Jordan is estimated to host about 0.40M refugees from Syria and Iraq in addition to approximately 0.30M Palestinian refugees ([ICMPD, 2018](#)). Finally, since the boom of the oil industry in the early 1970s, cities in the Gulf countries have attracted emigrant workers. It is estimated that the Gulf countries host about 5.0M expatriate workers from other countries including Egypt, Pakistan, India, Philippines and Bangladesh.

With this unrepresented increase in the urban population in the MENA region, local authorities in most MENA cities are struggling to adequately plan for sustainable urban growth and provide efficient infrastructure expansion. Unfortunately, most cities in the

region are suffering many of the above-mentioned undesirable consequences of such uncontrolled and unsustainable growth.

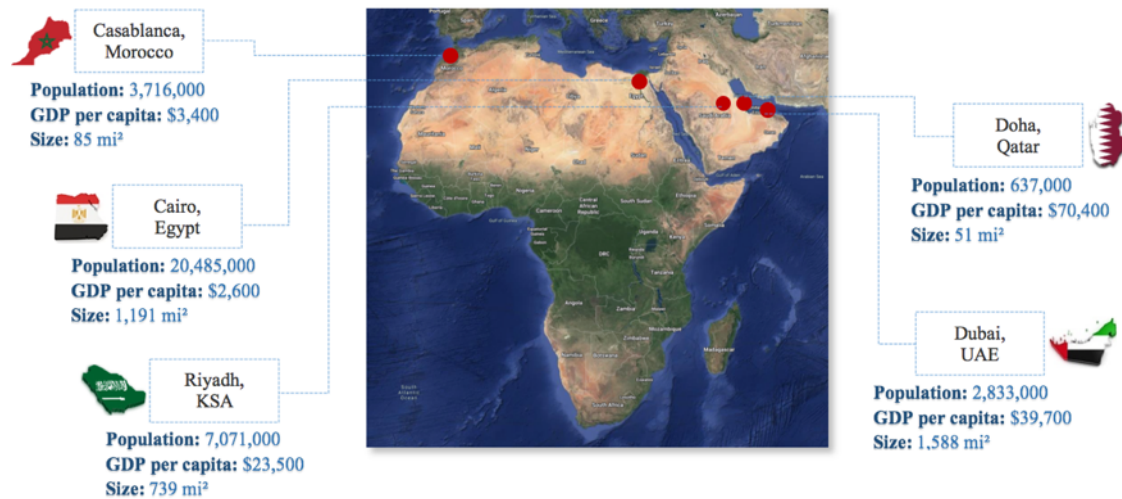
Considerable effort has been devoted to developing sustainable urban growth plans for cities in the MENA Region (e.g., Hashem and Balakrishnan, 2015; Alqurashi et al., 2016; Mallouk et al., 2019; Aldogom et al., 2019; Ibrahim et al., 2019; Altuwaijri et al., 2019). A main requirement for developing these plans is to obtain high-fidelity prediction of the growth pattern in terms of its direction and intensity under different growth management scenarios. While several urban growth prediction models (UGPM) have been developed during the past two decades as presented in Chapter 2, most models are assuming controlled growth environments where strict regulations and enforcement are maintained.

This assumption limits the suitability of these models to study urban growth of most MENA cities characterized by uncontrolled growth. In addition, in order to properly calibrate and validate these models, they require intensive amount of historical land use, biophysical and socioeconomic data that extends over a relatively long horizon. Obtaining such historical data is a challenge in most countries in the MENA region. Therefore, UGPMs adopted to study urban growth in the region should be capable of providing accurate prediction results with minimum data requirements.

### **8-3. Overview of the Selected Cities**

In this section, we provide an overview of the five MENA cities considered in this study. For each city, we present a brief historical background, growth trends and basic demographic and socio-economic data contributing to the growth. Figure 8-1 gives a map

showing the location of these cities in the MENA area along with a summary of their data.



**Figure 8- 1: The five MENA cities considered in this study.**

(Source: multiple resources as given in the text)

### 8-3-1. Dubai, UAE

Located on the coast of the Persian Gulf in the Arabian Peninsula, Dubai is UAE's second-largest city after Abu Dhabi and the most crowded city in UAE (Held and Cummings, 2018). The city was first established in the early years of the nineteenth century (Ulrichsen, 2016). Modern development of the city started with the oil boom in 1960's. The city covers about 1,588 square miles, representing 5.0% of the total area of the UAE. With an average GDP per capita of about \$39,700, the city is one of the richest cities in the region. Dubai is a perfect example of rapidly developing cities. The city's population has grown significantly over the past four decades. In 1984, the total population was only 325,000 persons, and jumped to more than 2.8 million in 2019 see Table 8- 1.



The city was gradually transformed from a small cluster of settlements on the Arabian Gulf into a modern multicultural city with a state-of-the-art infrastructure and commercial hubs. According to [Elessawy \(2017\)](#), the progress of Dubai's urban development could be divided into four different periods: (1) urban origin before 1971, (2) the planned suburban growth from 1971 to 1984, (3) the modern construction of Dubai from 1985 to 2003, and (4) mega city formation starting in 2004.

In the first period, Dubai Municipality was established and started to form the roads and the town center following the city's first master plan. During this period, growth has sprawled incoherently on the outer edges of Dubai specifically along the West roads toward the City of Abu Dhabi and the East roads towards the City of Sharjah. A new master plan was developed for the second period followed by enormous expansion, where the total built-up area increased from 15.44 to 42.08 square miles ([Elessawy, 2017](#)). In the beginning of the third period, a strategic plan was created to guide the development of the city into the 21<sup>st</sup> century. The plan included the construction of mega projects converting the city into a large metropolis with city-of-cities structure, where the city's total built-up area expanded to 377 square miles. The current stage focuses on the upgrade of the city's central business district (CBD) and the construction of new suburbs. Enriching the city's skyline, several hotels, residential and financial tower buildings have been constructed, which contribute significantly to the city's economic and tourism activities. Peripheral growth also continued to occur, connecting the city to adjacent emirates such as Sharjah and Ajman to the east and Abu Dhabi to the west.

### **8-3-2. Cairo, Egypt**

Cairo is Egypt's capital and considered the most significant urban center in Africa due to its long history and large population. The city is located at the fork of the Nile's Delta north of Egypt. The city covers about 1,191 square miles on the east and west banks of the River Nile and is surrounded by desert hills to the east and west (Robaa, 2003). As one of the most crowded cities in the world, Cairo's current population is estimated at about 21M with a current growth rate close to 2%. Modern Cairo was founded as a capital by the Fatimid dynasty in 969 CE, and since then the city has undertaken several stages towards urbanization (AlSayyad, 2013).

The urban development of Cairo was based on the idea of asserting its significance of the city and developing a highly accessible capital. As such, the construction of highways and bridges in the city center allowed smooth connection between the new housing areas and the city's commercial center. In addition, new highways were constructed along the east-west axis which serve the city's central business district and connect the airport to the pyramids of Giza.

To accommodate the significant increase in the population, a plan was envisioned to develop new societies in the dessert surrounding the old city. The government established several new towns in the desert to facilitate urban growth outside Cairo and its agricultural periphery. However, some of these towns failed to attract considerable population because they lacked the necessary services and infrastructure. In the last two decades, private developers were handed over the business of new residential developments in Cairo and the new surroundings towns. However, private developers

focused on building new compounds that serve mainly the high-income sector which represents a small percentage of the population. Most recently, the government started the construction of a new administrative capital in the desert east of Cairo. The new city is expected to host the government offices and most of the professional and financial services. The dynamics of Cairo in light of the interaction between the old and the new capitals are to be revealed in the coming years.

### **8-3-3. Doha, Qatar**

Since the establishment of the State of Qatar in 1971, Doha was declared as the country's capital and quickly became the center of most its economic and cultural activities. The city occupies about 51 square miles on the east coast of Qatar Peninsula. It has gradually transformed from a small pearling and fishing settlement to a modern urban center. Doha's population has grown significantly over the past few decades reaching near 0.65 million capita in 2019, compared to about 50,000 in 1971. The city is also the destination of a significant number of foreign workers, representing about 40% of the total population.

In the early stages of the city, Doha's urban development was based on transit-oriented development supported by a streetcar and railway system (Zaina et al., 2016). With the boom of the oil and gas industry, more dependence on the private car has been observed, resulting in significant sprawl to accommodate the high rate of population growth. The country's strong economy enabled the construction of new shopping malls, neighborhoods, and other facilities that have entirely reshaped Doha into a modern

capital (Azzali and Tomba, 2018). Mega infrastructure projects are undergoing as the country is scheduled to host the FIFA's World Cup activities in 2022.

#### **8-3-4. Casablanca, Morocco**

A coastal city located on the Atlantic Ocean, Casablanca is one of the oldest cities in North Africa. The city occupies about 85 square miles in western Morocco with a population that is close to 3.8 million capita. The city is known as Morocco's second capital and a significant tourist attraction. For several decades, the city continued to operate as a small-sized harbor with the population gradually stretching due to the improved residential homes and increased economic opportunities.

The first master plan for promoting the urban development of the city was developed soon after the French occupation in 1907 (Folkers and Buiten, 2019). The plan consisted of two main phases. The first phase focuses on reestablishing the city as a great port situated near its traditional core. The later phase suggested establishing a modern city to be developed around the city core. In the past few decades, the city has experience significant population growth resulting mainly from migration from surrounding farming areas.

With an estimated average GDP per capita of about \$3,400 by the end of 2020, the government has been struggling to develop the city to cope with this significant population increase. Despite effort to maintain controlled zoning practice to prevent undesirable growth patterns, the City of Casablanca has seen the formation of several slum areas occupied mainly by migrated agricultural labor from the mountains area. In recent years, the government has attempted to stop further growth of these slums by constructing large-

scale social housing projects, offered to the residents of these slums and other low-income groups. In addition, the private sector started to become involved in the city development with several ongoing projects to remodernize the traditional city core by adding affordable apartment complexes.

### **8-3-5. Riyadh, KSA**

Riyadh, the capital of KSA, is located in the middle of the Arabian Peninsula. Similar to most cities in the rich gulf countries, Riyadh is one of the few cities in the world whose urban developments have transformed significantly over a short period. The city evolved from a small desert village in the beginning of the 19<sup>th</sup> century to a large metropolitan area with more than seven million residents. Since the establishment of the Kingdom as an independent state in 1932, the city has been used as the government headquarters and declared as the Kingdom's new capital.

Taking advantage of the country's oil-trading wealth, the government has implemented significant projects to modernize the city, focusing on infrastructure development. In early stages, the city was growing in all directions with expedited establishment of neighborhoods of single-family houses. A master plan was later developed for the city suggesting the establishing a north-south axis to allow for future growth (Elsheshtawy, 2019). The plan did not consider public transportation, assuming full dependence on private vehicles as the sole mode of transportation. The city continued to grow in all directions, suffering from an uncontrolled urban sprawl pattern. With the increasing traffic congestion problem, the city pushed for more investment in public

transportation. Projects are underway to construct the city's metro network to reduce dependence on the private car and the associated congestion problem.

Table 8- 1: The Statistical information for the five MENA cities

No.	City	Year													
		1984	1985	1986	1987	1988	1989	1990	1991	1992	1993	1994	1995	1996	
1	Dubai, UAE	GDP per capita	\$39,700												
		Area	1,588 mi <sup>2</sup>												
		Population	325	345	366	391	416	444	473	504	537	572	610	650	694
			1997	1998	1999	2000	2001	2002	2003	2004	2005	2006	2007	2008	2009
		Population	742	793	848	907	970	1,037	1,109	1,186	1,268	1,365	1,478	1,600	1,732
			2010	2011	2012	2013	2014	2015	2016	2017	2018	2019			
		Population	1,875	1,970	2,070	2,175	2,285	2,401	2,523	2,651	2,785	2,833			
			1984	1985	1986	1987	1988	1989	1990	1991	1992	1993	1994	1995	1996
2	Cairo, Egypt	GDP per capita	\$2,600												
		Area	1,191 mi <sup>2</sup>												
		Population	8,123	8,328	8,539	8,826	9,169	9,523	9,892	10,275	10,674	11,087	11,516	11,962	12,426
			1997	1998	1999	2000	2001	2002	2003	2004	2005	2006	2007	2008	2009
		Population	12,773	13,051	13,335	13,626	13,922	14,225	14,534	14,851	15,174	15,504	15,842	16,187	16,539
			2010	2011	2012	2013	2014	2015	2016	2017	2018	2019			
		Population	16,899	17,267	17,643	18,027	18,419	18,820	19,230	19,648	20,076	20,485			
			1984	1985	1986	1987	1988	1989	1990	1991	1992	1993	1994	1995	1996
3	Doha, Qatar	GDP per capita	\$70,400												
		Area	50.97 mi <sup>2</sup>												
		Population	196	208	218	222	226	230	235	239	243	247	252	256	261
			1997	1998	1999	2000	2001	2002	2003	2004	2005	2006	2007	2008	2009
		Population	267	277	287	298	309	320	332	348	373	400	429	460	493
			2010	2011	2012	2013	2014	2015	2016	2017	2018	2019			
		Population	524	536	549	562	576	590	604	619	633	637			
			1984	1985	1986	1987	1988	1989	1990	1991	1992	1993	1994	1995	1996
4	Casablanca, Morocco	GDP per capita	\$3,400												
		Area	84.94 mi <sup>2</sup>												
		Population	2,355	2,406	2,459	2,513	2,568	2,624	2,682	2,741	2,801	2,862	2,925	2,963	2,997
			1997	1998	1999	2000	2001	2002	2003	2004	2005	2006	2007	2008	2009
		Population	3,031	3,065	3,099	3,134	3,170	3,205	3,242	3,278	3,307	3,335	3,362	3,391	3,419
			2010	2011	2012	2013	2014	2015	2016	2017	2018	2019			
		Population	3,447	3,476	3,505	3,534	3,563	3,593	3,623	3,653	3,684	3,716			
			1984	1985	1986	1987	1988	1989	1990	1991	1992	1993	1994	1995	1996
5	Riyadh, KSA	GDP per capita	\$23,500												
		Area	739 mi <sup>2</sup>												
		Population	1,447	1,566	1,695	1,834	1,985	2,149	2,325	2,517	2,724	2,845	2,938	3,035	3,135
			1997	1998	1999	2000	2001	2002	2003	2004	2005	2006	2007	2008	2009
		Population	3,238	3,344	3,454	3,567	3,684	3,806	3,931	4,060	4,252	4,471	4,700	4,868	5,041
			2010	2011	2012	2013	2014	2015	2016	2017	2018	2019			
		Population	5,220	5,406	5,599	5,798	6,004	6,218	6,440	6,669	6,907	7,071			
			1984	1985	1986	1987	1988	1989	1990	1991	1992	1993	1994	1995	1996

#### **8-4. A Review of Urban Growth Studies Conducted for the Selected MENA Cities**

**Dubai:** Several recent studies have focused on studying the progression of the City of Dubai. These studies incorporate both remote sensing (RS) and GIS (Alghais, 2018). For example, Khalil et al. (2017) adopted a technique to assess the city's infrastructural growth by analyzing a sequence of satellite images. Elmahdy and Mohamed (2018) proposed a low-cost remote sensing (RS) approach to analyze the land use and land cover (LULC) changes. Their methodology adopted an image difference procedure to improve the categorization of maps and aid the process of growth monitoring and evaluation. The study predicted a considerable reduction in the vegetation cover in the city as a result of urbanization.

Adopting a methodology similar to the one presented in Khalil et al. (2017), Aldogom et al. (2019) employed multiple time series Landsat images to discover and evaluate the city's development profile. The methodology consists of three main steps. The first step involved classification algorithms in conjunction with variation detection, segmentation, and extraction to achieve LULC footprints. In the second step, Shannon's entropy is used to predict if the city is compacting or sprawling. In the third step, the CA-Markov approach was applied to simulate the city's future expansion. The study reported a significant evolution in the urban fabric of the city, estimating a three percent expansion by 2030 at the expense of green areas and open spaces. Similar results were reported in the model adopted by Abulibdeh et al. (2019).

**Cairo:** Several studies have focused on studying Cairo's growth focusing on developing sustainable growth plans for the city. The work of Abdalmalak et al.

(2016) and Midekisa et al. (2017) discuss the drivers of uncontrolled growth in Cairo and the need to address them for sustaining and protecting surrounding farming spaces. Osman et al. (2016) evaluated policies to preserve agricultural space on the north and the south borders of the city. They employed the SLEUTH model to analyze the influence of the policies on land use. The model provided two conclusions: a) a compact growth approach could pose minimal effect on the agricultural space, and b) the city will continue to grow considering its historical expansion trends.

In a subsequent effort, Osman et al. (2019) developed a modeling framework that integrates Markov Chain (MC), CA, and Logistic Regression (LR). The framework aimed at enhancing the value of spatiotemporal models and extrapolations of urban sprawl and land utilization variations. The framework predicted a continuous loss of agricultural land, and the development of future urban settlement along major roads.

Ibrahim et al. (2019) developed PredictSLUMS, an ML-based model developed to identify and forecast the expansion of unofficial settlements in Cairo. PredictSLUMS integrates Multinomial Logistic Regression (MLR) and ANN techniques. The model displayed a high legitimacy and precision in identifying and forecasting informal growth within Cairo.

**Doha:** Several models have been developed to study the process of urbanization and inform sustainable land use management and policymaking for the City of Doha. These studies emphasized that the expedited logistic and infrastructure projects within the city significantly affected its urban fabric as a result of poor realization of master plans and land utilization strategies (Mansour et al., 2020; Verbeek, 2017). Shandas et al.



(2017) developed a model to evaluate the opportunities for sustainable growth based on remote sensing data. They examined the pace, quality, and behavior of expansion. The outcome of their study suggested that the development patterns of Doha were equivalent to that of western cities. As such, urban planners need to evaluate if this growth pattern can be sustainable.

The model developed by Makido et al. (2020), which is based on a mixture of spatial analysis, predicted that more than 20000 hectares of open space will experience urban developments. The study suggested that this scenario could significantly change the land utilization patterns and impact the overall environment quality of the city. Hashem and Balakrishnan (2015) proposed a model that is based on Markov process integrated with GIS and remote sensing to generate different scenarios of future LULC change in the city. The model predicted that the built-up areas will increase by about 20%, occurring in the urbanized open space within and around the city.

**Casablanca:** Concerned by the city's ongoing uncontrolled growth, several models have been developed to enable informed decision making by policymakers and planners (Kadhim et al., 2016; Buğday and Buğday, 2019). For example, Mallouk et al. (2019) developed an urban growth prediction model that is based on SLEUTH. The approach entails calibrating the model using satellite imagery. The result of the study predicted an increase in the urbanized space as a result of expanding the city's port infrastructure.

Saadani et al. (2020) developed a CA-based Markov Chain (CA-MC) approach to simulate the growth of Moroccan cities. The model combined CA-MC with Landsat images

to forecast LULC. The study reported that rapid urban growth did replace the agricultural spaces. The prediction outcome calls for the institution of novel environmental protection measures and the promotion of sustainable growth.

**Riyadh:** Several models have been used to explain the growth pattern of the City of Riyadh. For instance, [Al-Ahmadi et al. \(2016\)](#) presented an improved CA-based model referred to as Fuzzy Cellular Urban Growth Model (FCUGM) that incorporated a genetic algorithm (GA), parallel simulated annealing (PSA), and expert knowledge (EK). The outcome of this study suggested that a combination of GA and EK enhances the model's prediction performance.

[Alqurashi et al. \(2016\)](#) used a simulation model that integrates the CA and MC techniques to predict the urban growth at years 2024 and 2034, respectively. Their model is claimed to offer a fundamental comprehension of historical, present, and future patterns of urban sprawl in the city. [Al-Ahmadi \(2018\)](#) modeled the expansion pattern and the drivers of urbanization in the City of Riyadh by incorporating GIS and Fuzzy sets. The results obtained by the model are intended to simulate the decision-making process utilized for zoning and defining land use structures.

The study conducted by [Altuwajri et al. \(2019\)](#) focused on predicting the growth of the city to year 2040 using the CA-MC model supported by GIS platform. The study predicted 38% increase in urban spaces during the next three decades. Finally, [Alghamdi and Cummings \(2019\)](#) used the high-resolution SPOT 5 images and developed a framework that integrates maximum likelihood and object-oriented categorization to assess land use variation between years 2004 and 2014.

## 8-5. Urban Growth Prediction for the Selected MENA Cities: Model Application

This section presents the results of applying the ML-based urban growth prediction model described in Chapter 4 for the five selected MENA cities. We adopted the same model structure and hyperparameter values used for the DFW model (i.e., autoencoder with five convolution and five deconvolution layers, RMSprop optimizer, 2000 epochs, and 64 batch size).

The model is trained using a dataset obtained for each of the five cities. In other words, a separate model is developed for each city using its satellite imagery dataset. To prepare the dataset for each city, a series of historical satellite images for that city is first collected. High resolution images became available starting in 1984 with the launching of Landsat 5 (U.S. Geological Survey, 2020). Thus, a past horizon that extends from 1985 to 2019 is considered. The clearest image in each quarter of each year is obtained. In cases where there are no clear images (i.e., cloudy conditions) available for a quarter, an image from the next or previous quarters is borrowed for that quarter.

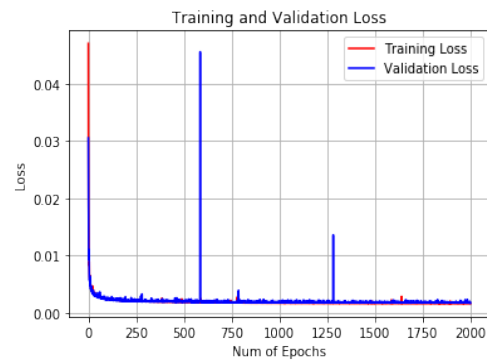
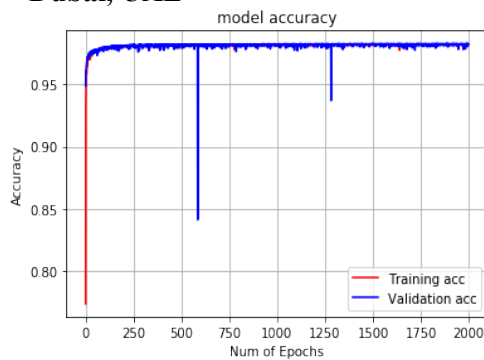
Thus, four different streams of satellite images are obtained for each area. Each stream includes 35 images that represent the area's year-to-year growth. Each stream resulted in 765 data records (i.e., combinations of  $I_x$ ,  $I_y$ ,  $\Delta t$ ). Combining the four streams together, a total of 3060 data records are obtained for each city. This dataset is used for model training and validation with 80%-20% split. A high-performance computing (HPC) cluster with graphics processing capabilities is used to train the model. The cluster includes 36 cores of NVIDIA P100 GPUs with 256 GB memory.

It is worth mentioning that the downloaded satellite images have a resolution of about 15,000x12,000. However, these high-resolution images could not be used directly considering the limited memory of the used HPC platform. The downsizing of the images is conducted in an iterative way. After several trials to examine the highest resolution that can be used, the resolution of the original images was reduced to 512x512.

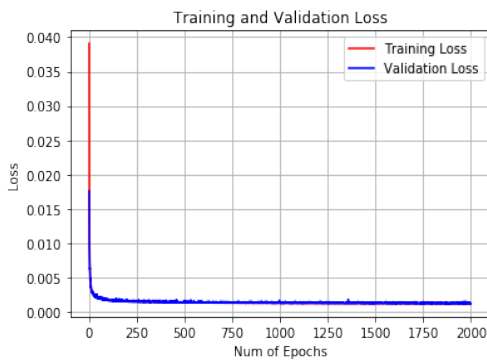
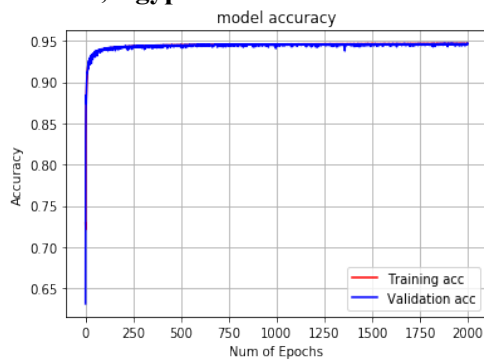
**Table 8- 2: The model prediction performance for the five MENA cities**

MENA Cities	Training		Validation	
	Accuracy	Loss	Accuracy	Loss
Dubai, UAE	0.9814	0.0016	0.9820	0.0017
Cairo, Egypt	0.9467	0.0012	0.9468	0.0012
Doha, Qatar	0.9663	0.0017	0.9665	0.0020
Casablanca, Morocco	0.9419	0.0019	0.9382	0.0019
Riyadh, KSA	0.9939	0.0010	0.9938	0.0010

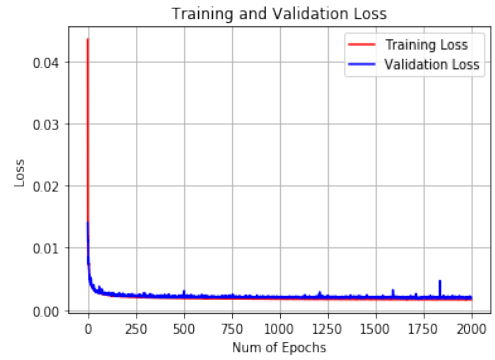
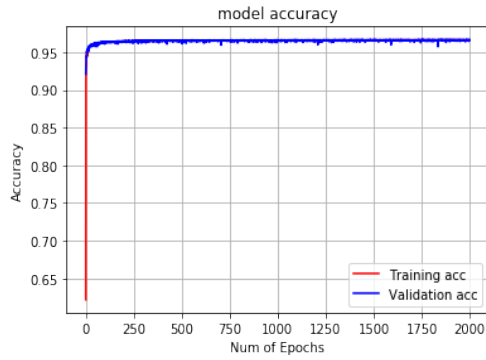
### Dubai, UAE



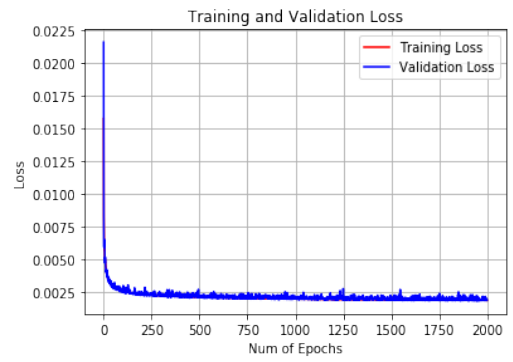
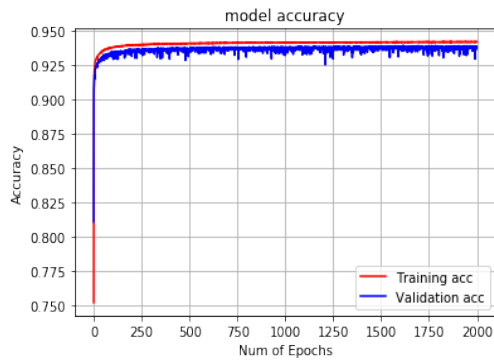
### Cairo, Egypt



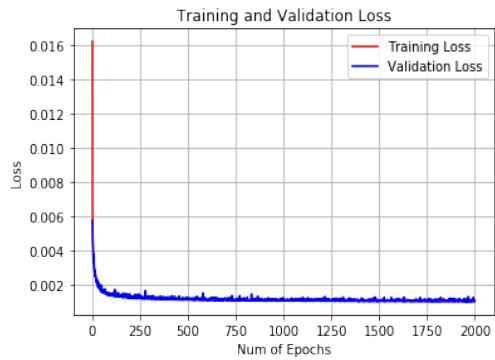
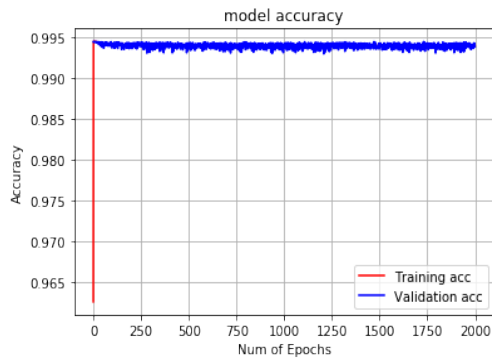
### Doha, Qatar



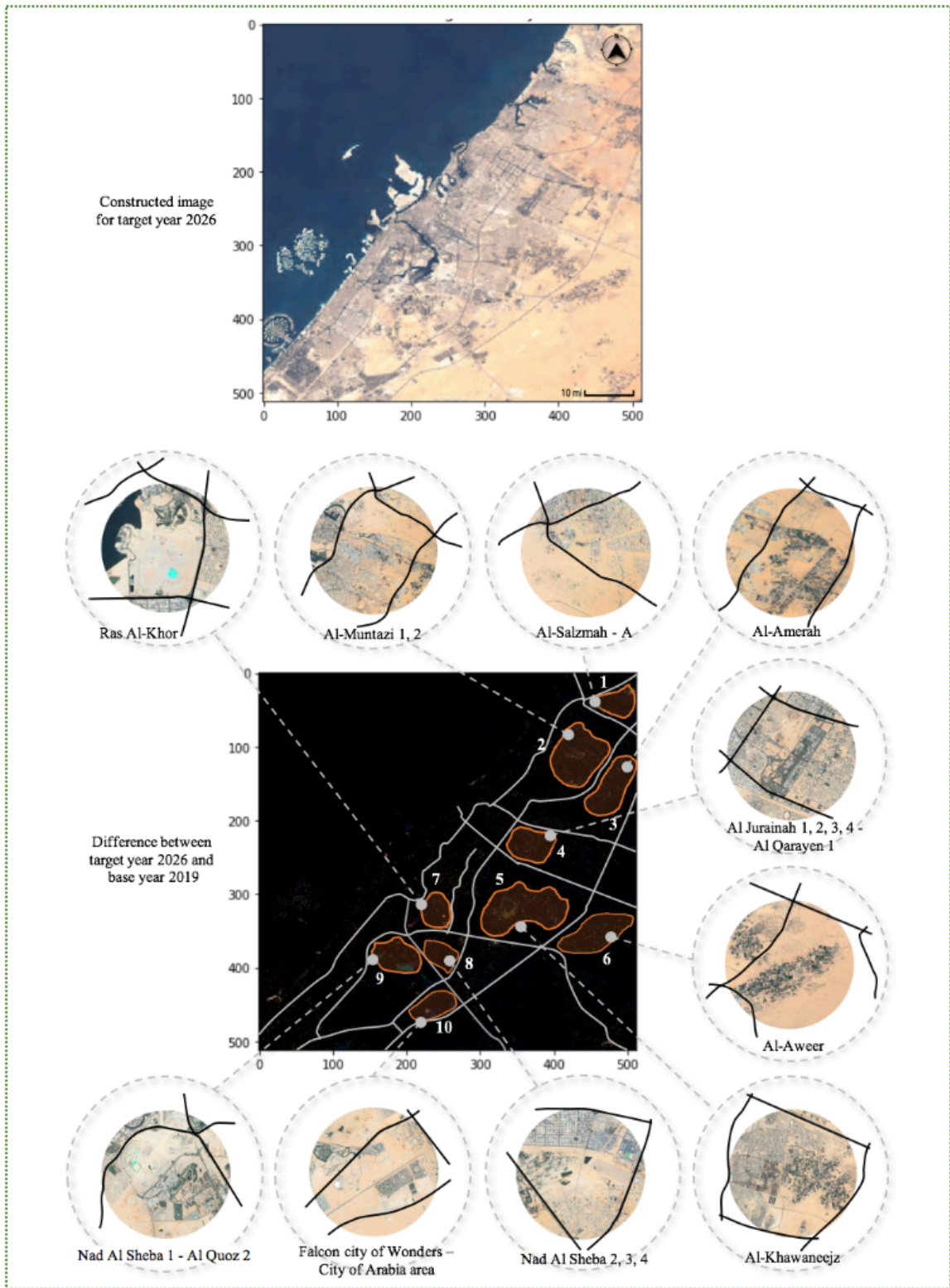
### Casablanca, Morocco



### Riyadh, KSA



**Figure 8- 2: The convergence pattern of the accuracy (left) and loss functions (right) of the model's training and validation processes for the five MENA cities considered in this study.**



**Figure 8- 3: Predicted urban growth of the City of Dubai for year 2026.**

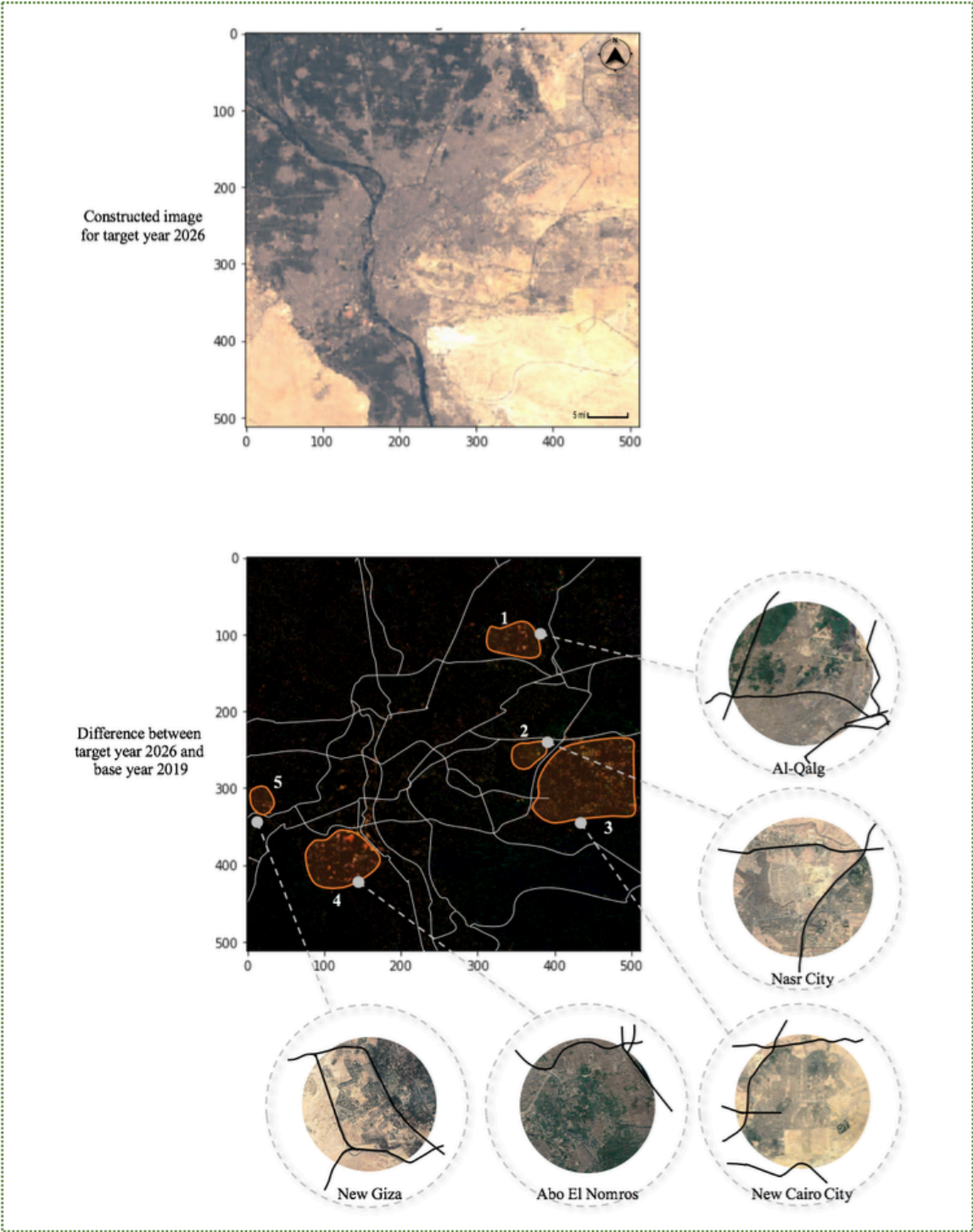


Figure 8- 4: Predicted urban growth of the City of Cairo for year 2026.

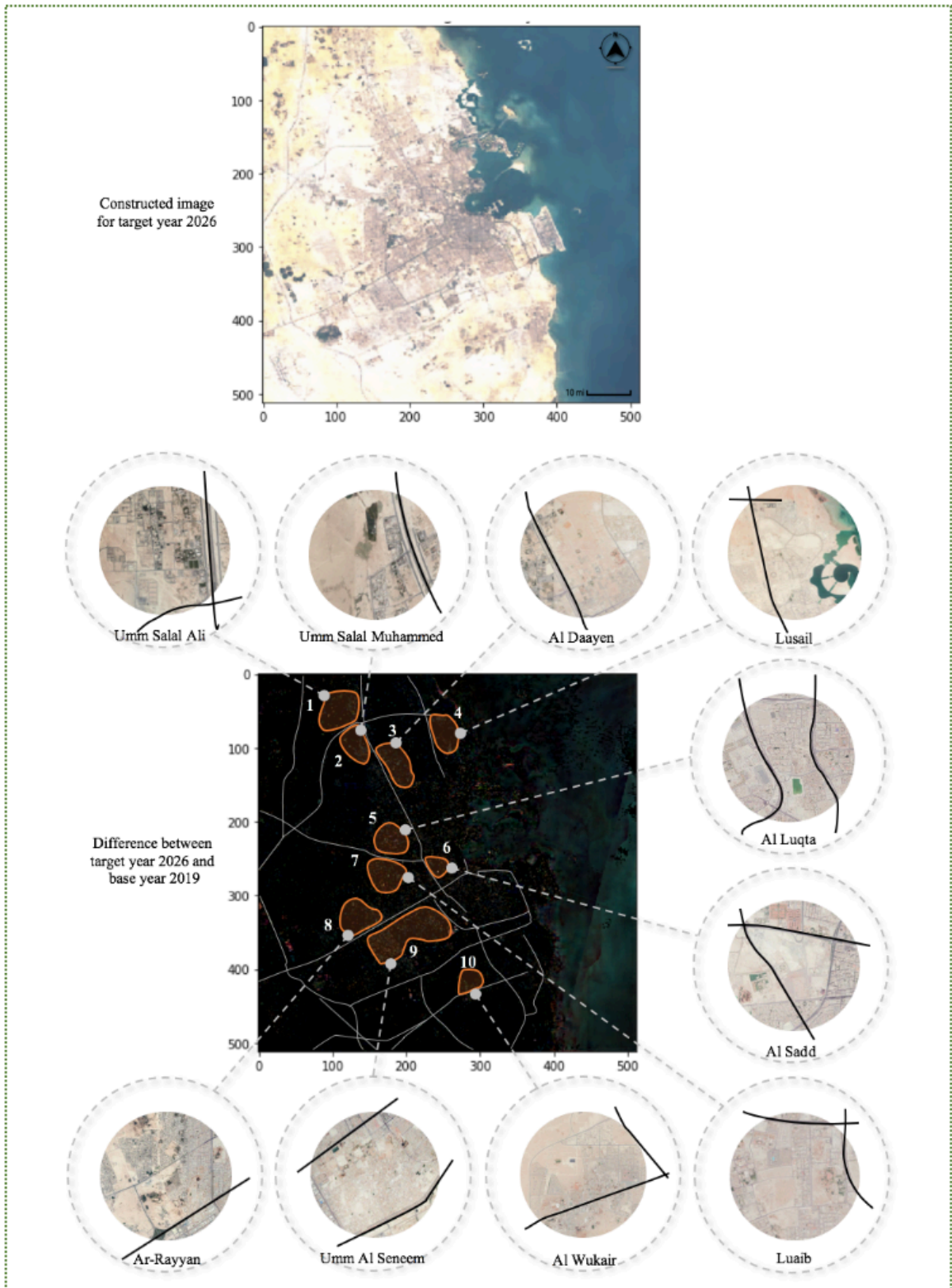
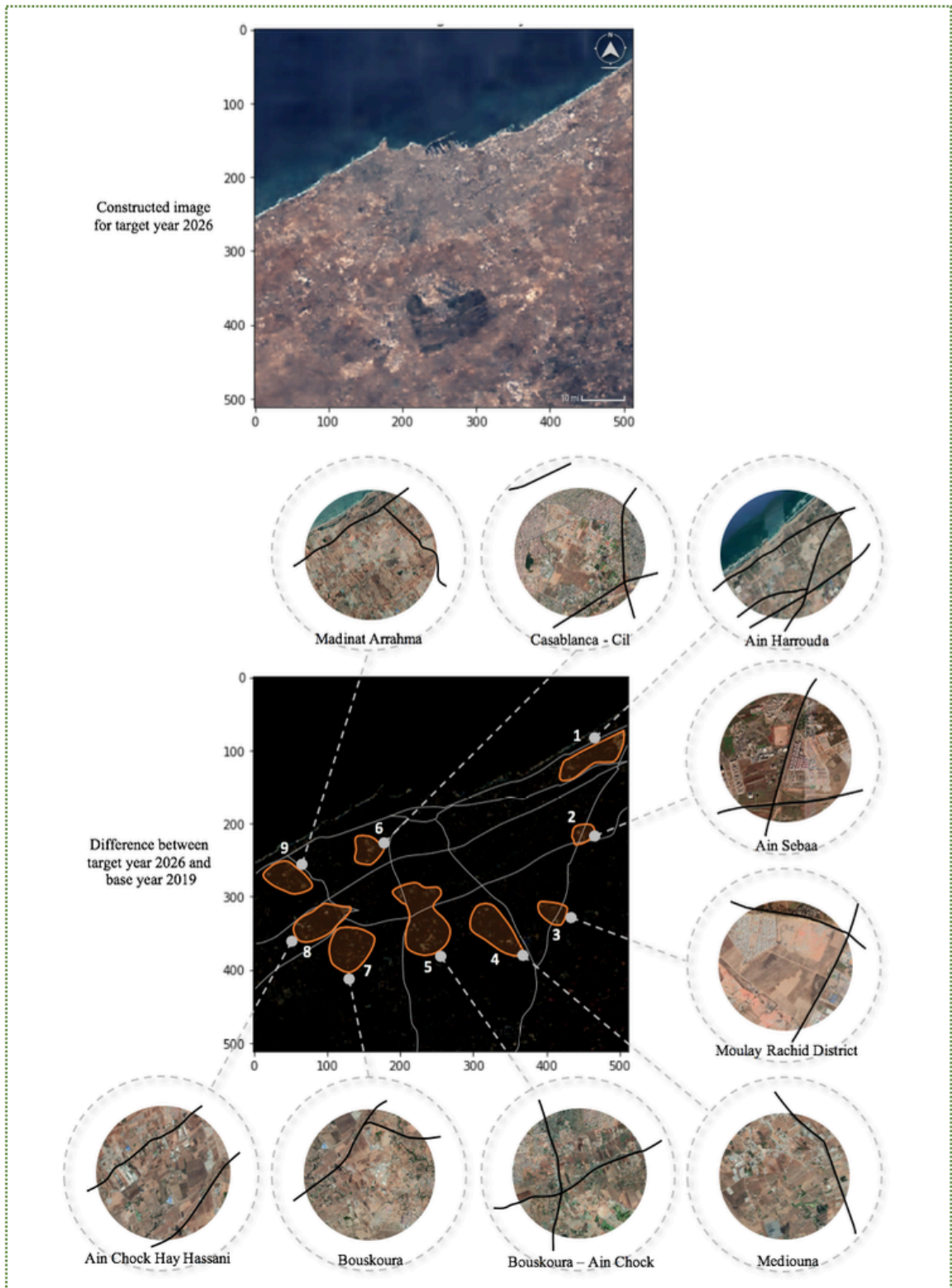
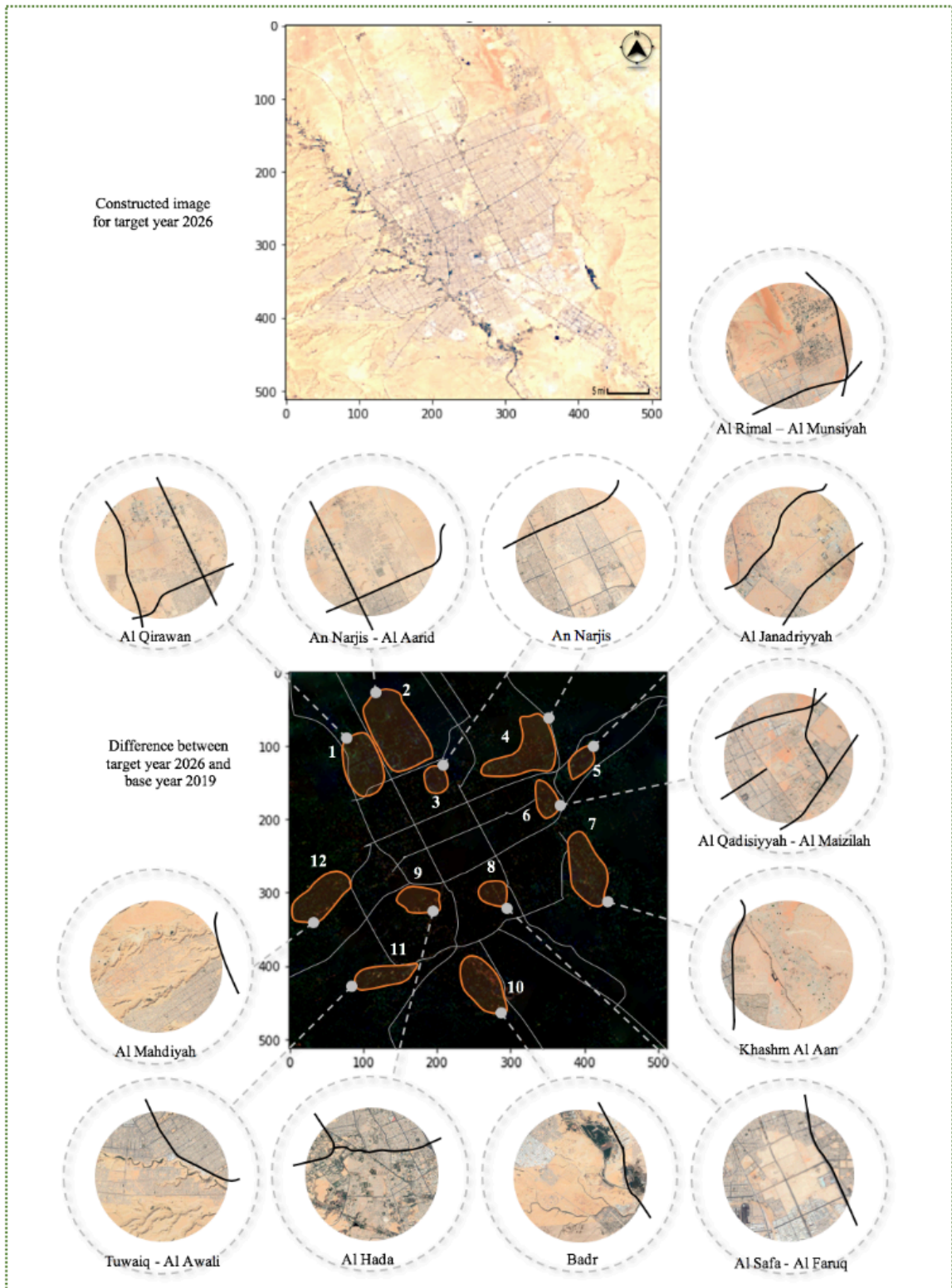


Figure 8- 5: Predicted urban growth of the City of Doha for year 2026.





**Figure 8- 6: Predicted urban growth of the City of Casablanca for year 2026.**



**Figure 8- 7: Predicted urban growth of the City of Riyadh for year 2026.**

Figure 8-2 illustrates the convergence pattern of the accuracy and loss functions for the training and validation processes of the model developed for each city. As illustrated in the figure, all five models showed systematic convergence patterns of their accuracy and loss functions. A summary of the values of these functions at convergence is also given in Table 8- 2. As shown in the table, all models converge at accuracy values higher than 94.00% and loss value that are less than 0.002. For example, the City of Riyadh recorded the highest accuracy value at 99.39%, and the lowest loss value at 0.001. On the other hand, the City of Casablanca recorded the lowest accuracy value at 94.19%, and the highest loss value at 0.0019.

Considering year 2019 as the base year, the model is used to predict the growth patterns for the five MENA cities in the target year 2026, respectively. The prediction is obtained in the form of a model-constructed satellite image showing the city growth in the target year. Figure 8-3 to 8-7 present the obtained prediction results for the five cities. In each figure, the constructed satellite image is given for the target year. In addition, the difference between the target year's image and the base year's image is provided. This difference image highlights all the zones predicted to include significant growth activities (i.e., zones with significant difference between the predicted and the base images). To validate the obtained prediction results, each figure included a zoom-in view of each identified growth zone showing its current state of development. Examining these zoom-in views shows that these zones are either an extension of existing developments located at the city boundaries, or a fill of an open space surrounded by already developed areas. In all cases, these identified zones are located near major roadways that facilitate their access.

The following subsections provide an analysis of the results obtained for each city by comparing them with results obtained from previous urban growth studies conducted for these cities. Of course, one should not expect a perfect match between the future growth pattern produced by the model and those obtained from other studies, which themselves are predictions that need to be verified. Nonetheless, the analysis presented here is intended to generally examine the level of agreement between the different modeling approaches.

#### **8-5-1. Dubai, UAE**

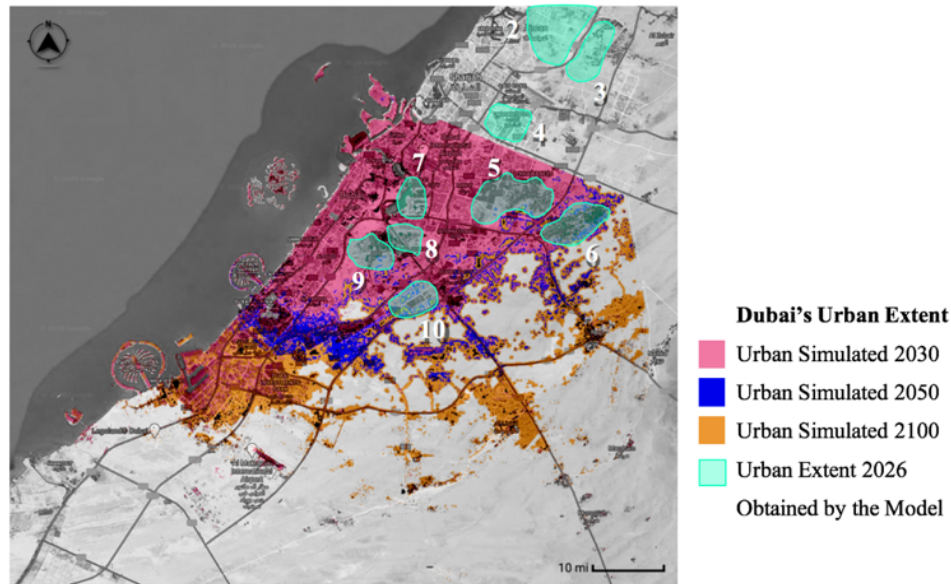
As shown in Figure 8-3, the model predicts 10 zones with active development in the target year. The development of these zones is expected to further convert the cities of Dubai, Sharjah and Ajman into one large metropolitan area and to further expand its size. These 10 zones are a combination of peripheral zones as well as inner zones that were skipped in previous development stages. Zones 1, 6, 9 and 10 are examples of peripheral zones that expand the size of Dubai's metropolitan area.

For example, Zone 1 shows a future growth in Al-Salamah and Al-Abrab located on the north and northeast boundaries (i.e., north east of Ajman). Similarly, Zone 9 and Zone 10, are located at the south boundaries of Dubai known by Nad Al Sheba 1, MBR city, Al Quoz 2, and City of Arabia area. Inner zones are partially developed areas with vacant land that is ready for further development as shown in Zones 4, 5 and 7, respectively. The zones representing Al-Jurainah, Al-Khawaneej and Al-Khor areas will experience development to fill their vacant lands. One observation is that all identified growth zones are accessible through the existing roadway network.

This pattern demonstrates the strong correlation between transportation accessibility and urban growth. In addition, it is clear from the zoom-in views provided in Figure 8-3 that the identified growth zones are surrounded or close to areas that are already developed. New developments that is not connected to the existing fabric of the city has not been observed.

The results in Figure 8-3 are compared against those reported by [Aldogom et al. \(2019\)](#). Unfortunately, this benchmarking study was limited only to the Emirate of Dubai excluding its neighboring cities: Sharjah and Ajman. In addition, the study was also limited to defining the new boundaries of the city without identifying density changes within these boundaries. As mentioned earlier, [Aldogom et al. \(2019\)](#) implemented a methodology that integrates classification algorithms and CA-Markov approach to simulate the city's future expansion for years 2030, 2050, and 2100, respectively. The CA-Markov approach creates a transition probability matrix to evaluate the changes in each pixel in the map over time, and a transition area matrix to illustrate the number of these changed pixels.

The results of the benchmarking study are summarized in Figure 8-8, which presents the predicted growth for the three considered target years. The predicted growth zones obtained by our model which, indicated by a light green color are superimposed on that figure. The Figure shows that the growth zones identified within the borders of the Emirate of Dubai (Zones 5 to 10) are falling within the 2030 city growth reported by [Aldogom et al. \(2019\)](#). The agreement between the two models encourages the adoption of remote sensing and video prediction-based UGPM to provide the City of Dubai's authorities and urban planners with adequate tools to predict the city's growth with limited data requirements.



**Figure 8- 8: Model validation and urban expansion of the City of Dubai.**

(Source: Aldogom et al., 2019)

### 8-5-2. Cairo, Egypt

The growth prediction results for the City of Cairo are presented in Figure 8-4. The model predicts a steady growth towards the east and the west deserts as well as the disappearance of several agricultural pockets in the Nile’s Delta. The growth in the east side of the city, identified by Zone 2 and Zone 3, extends Cairo’s boundaries through a new development in the east known as New Cairo. This growth is supported by the accessibility provided by two main highways, namely, the Suez road and the Ain El Sokhna road.

It is worth mentioning that Egypt’s government has recently announced the start of a mega-project to develop a New Administrative Capital (NAC) further east of New Cairo, which is planned as a modern city with a target population of 5.0 to 6.5M people (Loewert and Steiner, 2019). This new administrative city is expected to expedite the growth on the east side of old Cairo predicted by the model. The model also predicts a similar growth in

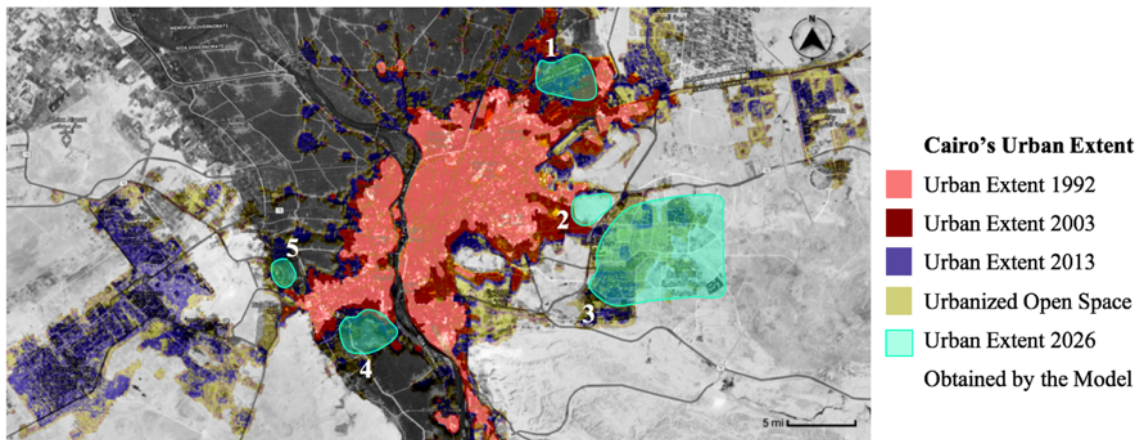
the western boundaries of Greater Cairo as depicted by Zone 5. This zone presents the development in New Giza, a new development west of the old Giza City (the western part of the Greater Cairo Metropolitan Area). This western growth is also promoted by the ongoing developments in the Sheikh Zayed City and the 6th of October City, which are relatively new cities located 30 miles from Cairo's downtown in the west desert, and the transportation infrastructure developed to connect the two cities to Cairo (e.g., Cairo's Ring road and Alexandria's Desert road).

The other two zones (Zone 1 and Zone 4) predict new developments on agricultural lands in the north and the south of the Nile's Delta. The growth of the City of Cairo on the expense of agricultural land is a trend that has been observed during the past few decades. The model predicts the disappearance of the agricultural lands in Al-Qalg area in Qalyubia (Zone 1), and Abo Al-Nomros area in Giza (Zone 4). Both zones include agricultural lands surrounded by very high-density residential areas that were also built on an agricultural land in the past two decades.

We compared the obtained prediction results with a previous study that reported the change in urban extent of Cairo Metropolitan. The study gives a prediction of open space for future urbanization, as given in Figure 8-9 (Angel et al., 2012). This benchmarking study is based on a collaboration between the Urban Expansion Program at New York University, the United Nations Human Settlements Program (UN-Habitat), and the Lincoln Institute of Land Policy.

The study is applied to a global sample of 200 cities (e.g., New York, Sydney, Montreal, Wuhan, Cairo, Riyadh) to map the spatial changes and urban expansion. The

study adopts a data intensive approach, using data that were extracted from satellite images and land use surveys to predict the urban expansion of the city beyond 2013 with no specific target year. We superimposed the five growth zones predicted by the model on top of the urban expansion map reported in [Angel et al. \(2012\)](#). As shown in the Figure, all these growth zones are coinciding with the predicted urban extent for the metropolitan area (indicated by the yellow color). As the benchmarking study does not define a specific target year, one would expect the results of this study to show urban expansion that is not identified by our model which, limits its prediction to year 2026.



**Figure 8- 9: Model validation and urban expansion of the City of Cairo.**

(Source: [Angel et al., 2012](#))

### 8-5-3. Doha, Qatar

Similar to the results presented above, Figure 8-5 gives the constructed satellite image for the City of Doha in the target year. The Figure also shows the difference between this constructed image and the base year's image, highlighting zones with predicted significant growth activities. As shown in the Figure, ten growth zones are identified by the model. Most of these zones are falling in semi-urbanized space near the city's current

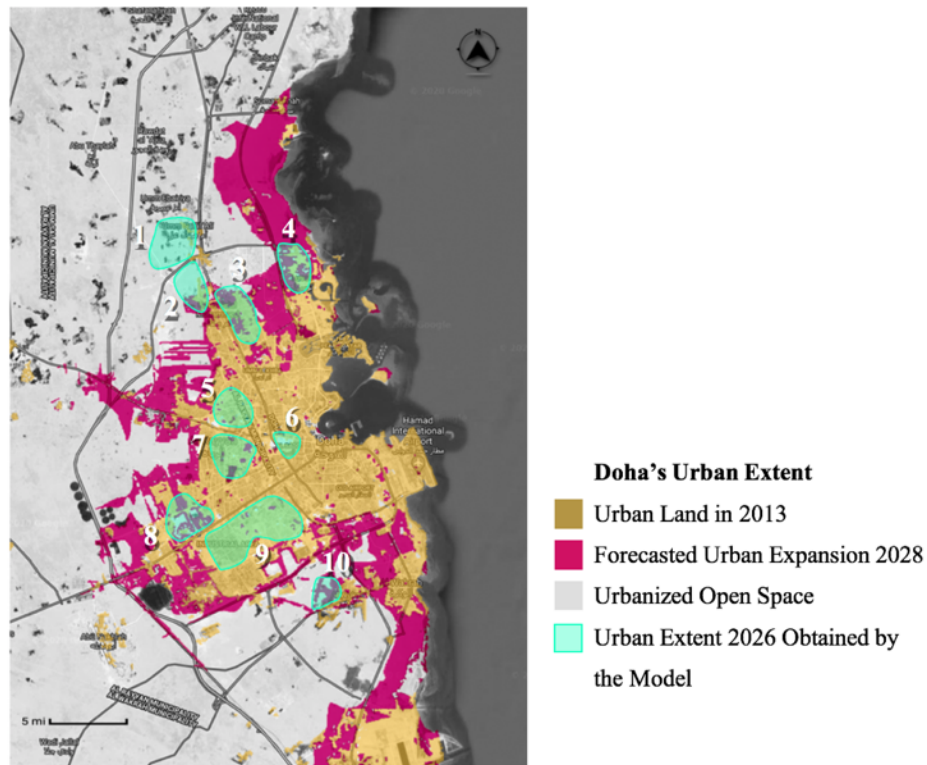


boundaries. These predicted growth zones are well connected through a strong highway system.

For example, a growth is predicted to occur toward the north side of the city as indicated by Zones 1 to 4, namely Umm Salal Ali, Umm Salal Muhammed, and Al-Daayen. These zones are located near main roadways in the city such as Wadi Al-Wasah road and the Doha Expressway. Growth is also expected to occur on the west side as illustrated by Zones 5 to 9 in Al-Luqta, Luaib, Al-Rayyan, and Umm Al-Seneem areas. These areas can also be accessed by major roads that connect the city in the north-south and east-west directions such as the Doha Expressway, Al-Rayyan road and Salwa road. Finally, the model predicts growth in Zone 10, which is known as Al Wukair area and is located on the south side of the city. This zone extends the west side of the City of Al-Wakrah, predicting its merge with the City of Doha to form a large multi-city metropolitan area.

Further investigating the locations of these zones and their surrounding environments, most are found to be located near mega commercial, entertainment, sport and education projects that are currently planned or under construction including Lusall, the Pearl, Katara, West Bay Area, Souq Wagif, Education City, and the Aspire Zone (Azzali, 2017). These results are compared against the growth pattern predicted by Makido et al. (2020). The approach adopted by Makido et al. (2020) is an empirical land-use change model that merges GIS with ANN to predict urban growth based on a set of representative variables (e.g., distance to roads, distance to previously developed areas, distance to urban center, and distance to the coast).

The results of their model are presented in Figure 8-10, which illustrates the urban growth predicted for target year 2028. The results obtained from our UGPM adopted is overlaid on that figure. On the north side, the growth predicted in Zones 2, 3 and 4 seems to agree with that predicted by Makido et al. (2020). However, the two models disagree with respect to the coastal growth on the north side of the city. Makido et al. (2020) predicted an expedited coastal growth on the north side that might not be realistic for target year 2028. On the south side, the two models agree in terms of the predicted growth for Zones 8 and 10, respectively. Model predictions in other zones (Zones 5-7 and 9) suggest an increase in the development density within the current boundaries of the city, which their model did not predict.



**Figure 8- 10: Model validation and urban expansion of the City of Doha.**

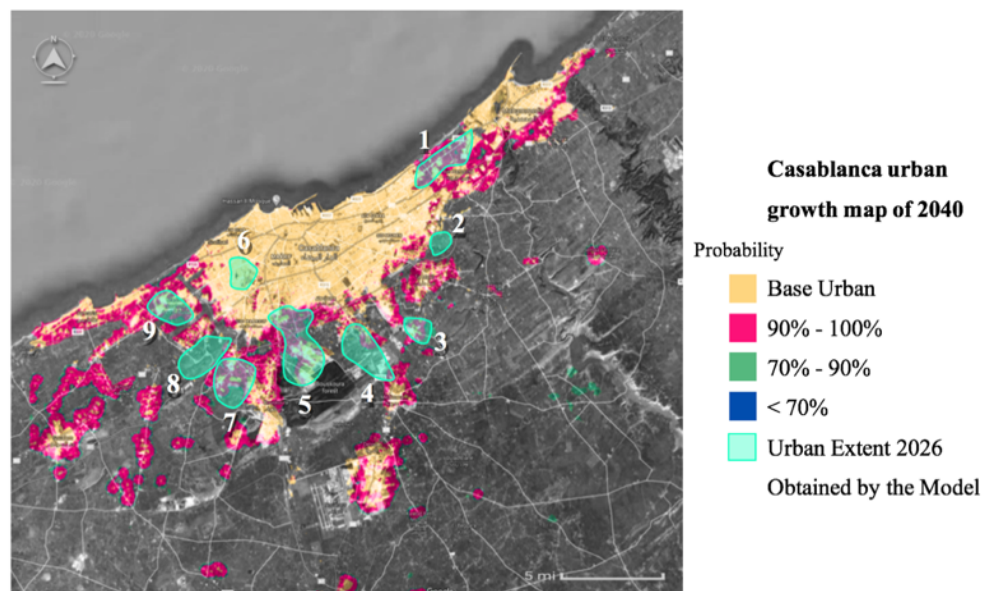
(Source: Makido et al., 2020)

#### **8-5-4. Casablanca, Morocco**

The prediction results for the City of Casablanca are provided in Figure 8-6. Similar to Dubai and Doha, the predicted growth is happening mostly inland and along the coast. However, two observations differentiate Casablanca from these two cities. First, all predicted growth zones are located at the city's current boundaries. Such a pattern is expected as Casablanca is an older city that is highly developed with limited vacant land available inside the city's current boundaries. Second, the predicted peripheral growth is almost uniformly distributed around the city. The city's high population growth rates combined with the intensive labor migration from its surrounding farms could explain this predicted uniform peripheral growth (Mallouk et al., 2019). The increase in the population from inside the city and the migrating population from its surrounding farms are naturally meeting at the city's current boundaries and expediting its growth along these boundaries.

As shown in the Figure, the model identifies nine growth zones. For example, Zone 1 shows growth northeast of the city in Ain Harrouda, which is an ocean front area between the City of Casablanca and the City of Mohemmedia. Zones 2 and 3 are located on the east side of Casablanca (Ain Sebaa, and Moulay Rachid District). These zones are supported by strong highway connectivity, including A1 and N9 highways. Similarly, the model predicts that Zones 4 and 5 known as Mediouna, Bouskoura, and Ain Chock will grow on the south side along highways R315 and N1, respectively. A significant growth is also predicted on the west side of the city (Zones 6-9) in the Casablanca-Cil, Bouskoura, Ain Chock Hay Hassani, and Madinat Arrahma areas, respectively.

Next, we compared our results against the growth pattern reported by [Mallouk et al. \(2019\)](#), which gives the probability of growth in year 2040 beyond the city’s current boundaries, as illustrated in Figure 8-11. This benchmarking study adopts the SLEUTH cellular automaton model [Chaudhuri and Clarke \(2013\)](#), which is calibrated using satellite images from 1984 and 2018. As shown in this figure, the two models agree in their predictions in most cases, especially in the northeast and the southwest sides of the city along the ocean front.



**Figure 8- 11: Model validation and urban expansion of the City of Casablanca.**

(Source: [Mallouk et al., 2019](#))

#### **8-5-5. Riyadh, KSA**

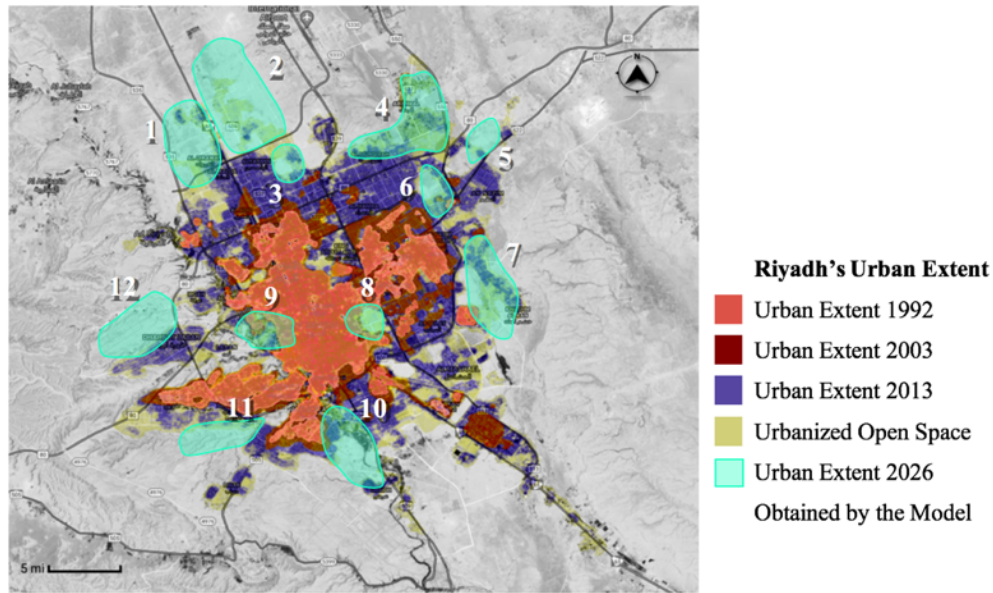
The growth prediction results obtained by the model for the City of Riyadh are presented in Figure 8-7. Based on these results, the city is predicted to grow from all directions. Twelve growth zones are depicted in the figure. One can expect this growth pattern considering the following factors: (1) this peripheral growth pattern matches the

historical growth pattern observed for the city during the past few decades; (2) the city continues to experience high population growth with a strong cultural preference of single-family dwellings pushing for new developments outside the city limits where the land is generally cheaper; and (3) the city is characterized by flat topography in the surrounding desert which promotes such a growth pattern.

For example, Zones 1 to 3 are the result of urban sprawl occurring on the north side of the city in the An-Narjis and Al-Aarid divisions. Such growth is also supported by their proximity to King Fahd road and King Salman road. Zone 4, located on the northeast side of Al-Rimal and Al-Munsiyah divisions, which is another area with significant predicted growth. The growth in this zone is supported by its proximity to Al-Janadriyah road in the east and Dammam road in the south. Another example is Zone 12, which is located on the west side of the city in the Al Mahdiyah area. This zone extends a fully developed area, Dhahrat Laban, further to the north.

Finally, we compared the prediction results with those of a previous study that predicts the change in the urban extent of the City of Riyadh, as given in Figure 8-12 ([Angel et al., 2012](#)). Similar to the City of Cairo, this benchmarking study is a collaboration between the Urban Expansion Program at New York University, the United Nations Human Settlements Program (UN-Habitat), and the Lincoln Institute of Land Policy. It adopts a data intensive approach extracted from satellite images and land-use surveys to predict the urban expansion of the city beyond 2013 with no specific target year. In most cases, the growth zones predicted by our model match the city's reported urban extent in the benchmarking study. This match in the prediction results is more obvious on the north

and east sides of the city, where all predicted growth zones are falling in urbanized open spaces.



**Figure 8- 12: Model validation and urban expansion of the City of Riyadh.**

(Source: Angel et al., 2012)

## 8-6. Discussion and Conclusion

Cities in the Middle East and North Africa (MENA) region have experienced significant population increase over the past few decades. As such, most urban areas in the region have expanded significantly to accommodate such population increase. Unfortunately, the expedited urbanization observed in most cities in the region presents substantial stresses to their ecological and financial resources, as well as to the overall well-being of their residents. To ensure long-term sustainability and eliminate the risk of uncontrolled growth in these cities, there have been increasing calls for adequate urban growth prediction studies that can be used as a foundation to develop sustainable growth plans for these cities.

This chapter studies the urban growth pattern in five major cities in the MENA region including Dubai (United Arab Emirates (UAE)), Cairo (Egypt), Doha (Qatar), Casablanca (Morocco), and Riyadh (Kingdom of Saudi Arabia (KSA)). These cities represent a representative sample of cities in the region that differ in terms of their size, population density, historical heritage, level of control applied to growth, geographical locations, complexity of their structure, and economic strength. The study adopts a machine learning (ML)-based modeling framework developed by the authors in a previous effort (Jaad and Abdelghany, 2020). The model integrates remote sensing and computer vision technologies to generate high-fidelity urban growth prediction with limited data requirements. The prediction results obtained by the model are compared against the results collected from other urban growth studies conducted for the selected cities. These results illustrate the potential of the presented approach to develop UGPMs with high fidelity.

Based on the results obtained for these MENA cities, several recommendations can be derived to assist the region's city planners and policy makers on their mission to develop sustainable urban growth plans for their cities. First, a strong correlation is observed between the roadway network and the predicted growth in all studied cities. Land developers usually give priority to vacant areas that are accessible by the existing roadway system. As such, the integration of the urban and transportation planning processes for urban areas is critical for ensuring their sustainable growth. In addition, while ring roads have been constructed to ease traffic congestion inside cities and to set rigid boundaries to curb growth, they have been shown to be ineffective in defining city boundaries and preventing its urban sprawl. For example, the City of Cairo continued to grow beyond its recently constructed ring road from almost all directions.

Second, careful attention needs to be given to the planning of mega projects in urban areas. As these projects usually represent major attractions, they could result in significant changes in their surrounding areas, either in terms of new developments or a change in the current land-use. For example, most urban developments predicted in the City of Doha are triggered by nearby new mega projects planned in the city.

Third, there is always considerable benefits in diversifying housing options within the city to prevent urban sprawl. These housing options include apartment buildings and townhomes which create high density residential areas near business districts and transit services (e.g., transit-oriented developments). For example, the expedited urban sprawl observed in the City of Riyadh is primarily contributed to the high preference of most households to live in a single-family home, even in the case of small family sizes. Housing policies and incentives that encourage small households to live in apartment buildings and townhomes could help in curbing the sprawl observed in the city.

Fourth, most cities in the region are suffering heavy migration from surrounding rural areas. This migration is mainly due to increasing agricultural automation and the lack of alternative job opportunities for the traditional agricultural labor. As observed in the cities of Cairo and Casablanca, the migration of poor labor to nearby cities has resulted in the creation of slums and neighborhoods with no adequate services. As such, adequate economic investment is needed to create viable economic opportunities in the surrounding rural areas to reduce this migration and prevent its adverse consequences.

Finally, urban growth could occur at the expense of valuable natural resources within or surrounding the city. For example, the City of Cairo has been growing at the



expense of high-value agricultural land on the north and the south boundaries. Similarly, the growth in Dubai and Doha is reported to be occurring at the expense of green space within these cities. As such, strict regulations and incentives are required to prevent such a growth pattern to ensure that valuable natural resources are preserved.

## SUMMARY AND FUTURE WORK

### 9-1. Summary

A machine learning-based model for urban growth prediction is presented. The model adopts the concept of VP in which successive historical satellite images are treated as a video for which future frames are predicted. Each future frame is a construction of a satellite image that predicts the urban growth for a specific targeted year.

An architecture in the form of CAE with time input is adopted for developing the model. The CAE is trained and validated using a dataset in which each record is a triplet of (a) base year satellite image for the area under study; b) target year satellite image for the same area; and (c) the time horizon between the two satellite images.

A sensitivity analysis is conducted to determine the model's optimal settings and values of its hyperparameters including number of layers in the CAE architecture, optimizer, data size, number of epochs and batch size. The model recorded the highest performance when the RMSprop optimizer with 2,000 epochs and 64 batch size is used considering CAE with five convolution layers and five deconvolution layers.

The developed model is applied to predict the urban growth for DFW and two of its fast-growing counties. The prediction results obtained by the model are compared against NCTCOG's growth prediction. These results illustrate the potentiality of the

presented approach to develop UGPMs with high fidelity. In addition, the developed model also applied to five MENA cities including Dubai (United Arab Emirates (UAE)), Cairo (Egypt), Doha (Qatar), Casablanca (Morocco), and Riyadh (Kingdom of Saudi Arabia (KSA)). These selected cities vary in terms of their size, population, historical heritage, level of control applied to their growth, geographical locations, complexity of their structure, and socio-economic characteristics. A framework is presented to validate the model by comparing its results with data collected from other urban growth studies conducted for these cities. Based on the obtained results and their analysis, some recommendations for sustainable urban growth in the MENA region are provided.

## **9-2. Further Research Extensions**

Several research extensions could be considered for the research work presented in this dissertation. For example, the adopted TDED architecture can be extended to include other input (e.g., population and socioeconomic data) that can be used to enhance the model predictability. For example, as the model is trained using information on the change in the image pixels, it can also be trained using the change in the major disruptions, such as natural disasters or economic downturns.

In addition, the model architecture presented in this research can be extended to answer policy-related questions related to, for example, the planning of the transportation and other infrastructure systems and employment allocation in the region. To achieve this goal, the architecture will be extended to include input variables, in addition to the satellite images, such as population/employment density and infrastructure configuration.

Finally, due to limited computational resources, the resolution of the satellite images was reduced in the presented case studies. Using more advanced computational platforms to take advantage of the high resolution of the satellite images could be investigated.

## BIBLIOGRAPHY

- Abdalmalak, K. A., & Gonzalez-Serrano, F. J. (2016). Forecasting of Cairo population using ARMA model. *The Egyptian International Journal of Engineering Sciences & Technology*, 19(2), 346-352.
- Abulibdeh, A., Al-Awadhi, T., & Al-Barwani, M. (2019). Comparative analysis of the driving forces and spatiotemporal patterns of urbanization in Muscat, Doha, and Dubai. *Development in Practice*, 29(5), 606-618.
- Acharya, U. R., Oh, S. L., Hagiwara, Y., Tan, J. H., & Adeli, H. (2018). Deep convolutional neural network for the automated detection and diagnosis of seizure using EEG signals. *Computers in biology and medicine*, 100, 270-278.
- Al-Ahmadi, K. (2018). Modeling driving forces of urban growth with fuzzy sets and GIS. In *Spatial Analysis, Modelling and Planning*. IntechOpen.
- Al-Ahmadi, K., Alahmadi, M., & Alahmadi, S. (2016). Spatial optimization of urban cellular automata model. *Applications of Spatial Statistics*. InTech, 61-94.
- Alberti, M., Mazluff, J. M., Shulenberger, E., Bradley, G., Ryan, C., & Zumbrunnen, C. (2003). Integrating humans into ecology: opportunities and challenges for studying urban ecosystems. *BioScience*, 53(12), 1169-1179.
- Albeverio, S., Andrey, D., Giordano, P., & Vancheri, A. (Eds.). (2007). *The dynamics of complex urban systems: An interdisciplinary approach*. Springer Science & Business Media.
- Aldogom, D., Aburaed, N., Al-Saad, M., Al Mansoori, S., Al Shamsi, M. R., & Al Maazmi, A. A. (2019, October). Multi-temporal satellite images for growth detection and urban sprawl analysis; Dubai City, UAE. In *Remote Sensing Technologies and Applications in Urban Environments IV* (Vol. 11157, p. 111570). International Society for Optics and Photonics.
- Alghais, N. (2018). Developing urban models to address population growth impacts and assisting with future urban planning in Kuwait and other Arabian Gulf countries.
- Alghamdi, A., & Cummings, A. R. (2019). Assessing Riyadh's urban change utilizing high-resolution imagery. *Land*, 8(12), 193.
- Alqurashi, A. F., Kumar, L., & Sinha, P. (2016). Urban land cover change modeling using time-series satellite images: A case study of urban growth in five cities of Saudi Arabia. *Remote Sensing*, 8(10), 838.

- AlSayyad, N. (2013). *Cairo: Histories of a City*. The Belknap Press of Harvard University Press, Cambridge, Massachusetts, USA.
- Altuwaijri, H. A., Alotaibi, M. H., Almudlaj, A. M., & Almalki, F. M. (2019). Predicting urban growth of Arriyadh city, capital of the Kingdom of Saudi Arabia, using Markov cellular automata in TerrSet geospatial system. *Arabian Journal of Geosciences*, 12(4), 135.
- Angel, S., J. Parent, D. L. Civco, and A. M. Blei. (2012). *Atlas of urban expansion*, Cambridge MA: Lincoln Institute of Land Policy. [www.lincolninst.edu/subcenters/atlas-urban-expansion](http://www.lincolninst.edu/subcenters/atlas-urban-expansion).
- Ayazli, I. E., Gul, F. K., Yakup, A. E., & Kotay, D. (2019). Extracting an Urban Growth Model's Land Cover Layer from Spatio-Temporal Cadastral Database and Simulation Application. *Polish Journal of Environmental Studies*, 28(3).
- Azzali, S. (2017). Mega-events and urban planning: Doha as a case study. *Urban Design International*, 22(1), 3-12.
- Azzali, S. & Tomba, M. (2018). Urban development and planning practice in Doha. *Mei Insight*, 180, 1-13.
- Bagan, H., & Yamagata, Y. (2015). Analysis of urban growth and estimating population density using satellite images of nighttime lights and land-use and population data. *GIScience & Remote Sensing*, 52(6), 765-780.
- Bang, S., Park, S., Kim, H., & Kim, H. (2019). Encoder–decoder network for pixel-level road crack detection in black-box images. *Computer-Aided Civil and Infrastructure Engineering*.
- Batty, M. (2013). *The new science of cities*. MIT press.
- Batty, M., Longley, P., and Fotheringham, S. (1989). Urban growth and form: scaling, fractal geometry, and diffusion-limited aggregation. *Environment and Planning A*, 21(11), 1447-1472.
- Beleites, C., Neugebauer, U., Bocklitz, T., Krafft, C., & Popp, J. (2013). Sample size planning for classification models. *Analytica chimica acta*, 760, 25-33.
- Berling-Wolff, S., & Wu, J. (2004). Modeling urban landscape dynamics: a case study in Phoenix, USA. *Urban ecosystems*, 7(3), 215-240.
- Black, K. M., Law, H., Aldouhki, A., Deng, J., & Ghani, K. R. (2020). Deep learning computer vision algorithm for detecting kidney stone composition. *BJU international*.

- Bonabeau, E. (2002). Agent-based modeling: Methods and techniques for simulating human systems. *Proceedings of the national academy of sciences*, 99(suppl 3), 7280-7287.
- Brown, D. G., and Duh, J. D. (2004). Spatial simulation for translating from land use to land cover. *International Journal of Geographical Information Science*, 18(1), 35-60.
- Brownlee, J. (2016). *Deep learning with Python: develop deep learning models on Theano and TensorFlow using Keras*. Machine Learning Mastery.
- Buğday, E., & Buğday, S. E. (2019). Modeling and simulating land use/cover change using artificial neural network from remotely sensing data. *Cerne*, 25(2), 246-254.
- Capelo, L. (2018). *Beginning Application Development with TensorFlow and Keras: Learn to design, develop, train, and deploy TensorFlow and Keras models as real-world applications*. Packt Publishing Ltd.
- Cha, Y. J., Choi, W., Suh, G., Mahmoudkhani, S., & Büyüköztürk, O. (2018). Autonomous structural visual inspection using region-based deep learning for detecting multiple damage types. *Computer-Aided Civil and Infrastructure Engineering*, 33(9), 731-747.
- Chan, C. W., & Chiu, M. L. (2000). A Simulation Study of Urban Growth Patterns with Fractal Geometry. *CAADRIA 2000, Proceedings of the Fifth Conference on Computer Aided Architectural Design Research in Asia*, Singapore, pp. 55-64.
- Chan, J. C. W., Chan, K. P., & Yeh, A. G. O. (2001). Detecting the nature of change in an urban environment: A comparison of machine learning algorithms. *Photogrammetric Engineering and Remote Sensing*, 67(2), 213-226.
- Chao, Y. W., Yang, J., Price, B., Cohen, S., & Deng, J. (2017). Forecasting human dynamics from static images. In *Proceedings of the IEEE Conference on Computer Vision and Pattern Recognition* (pp. 548-556).
- Chaudhuri, G., & Clarke, K. (2013). The SLEUTH land use change model: A review. *Environmental Resources Research*, 1(1), 88-105.
- Chauvin, Y., & Rumelhart, D. E. (2013). *Backpropagation: Theory, architectures, and applications*. Oxfordshire, England: Psychology Press.
- Chen, S., Leng, Y., & Labi, S. (2020). A deep learning algorithm for simulating autonomous driving considering prior knowledge and temporal information. *Computer-Aided Civil and Infrastructure Engineering*, 35(4), 305-321.
- Cheng, J. (2003). *Modelling spatial and temporal urban growth*. Utrecht University.

- Cheng, J., Masser, I., & Ottens, H. (2003). Understanding urban growth system: Theories and methods. In 8th international conference on computers in urban planning and urban management, Sendai City, Japan.
- Chiappa, S., Racaniere, S., Wierstra, D., & Mohamed, S. (2017). Recurrent environment simulators. arXiv preprint arXiv:1704.02254.
- Cho, C., Park, J., & Sakhakarmi, S. (2019). Emergency response: effect of human detection resolution on risks during indoor mass shooting events. *Safety science*, 114, 160-170.
- Choi, J., & Dyke, S. J. (2020). CrowdLIM: Crowdsourcing to enable lifecycle infrastructure management. *Computers in Industry*, 115, 103185.
- Clarke, K. C., & Gaydos, L. J. (1998). Loose coupling a cellular automaton model and GIS: Long-term urban growth prediction for San Francisco and Washington/Baltimore. *International Journal of Geographical Information Science*, 12(7), 699–714.
- Couclelis, H. (2002). Modeling frameworks, paradigms, and approaches. *Geographic Information Systems and Environmental Modelling*, Prentice Hall, London.
- D’Autilia, R., & Hetman, J. (2018). Complex Buildings and Cellular Automata—A Cellular Automaton Model for the Centquatre-Paris. *Urban Science*, 2(2), 50.
- Debnath, R., & Amin, A. N. (2016). A geographic information system-based logical urban growth model for predicting spatial growth of an urban area. *Environment and Planning B: Planning and Design*, 43(3), 580-597.
- Defferrard, M., Bresson, X., & Vandergheynst, P. (2016). Convolutional neural networks on graphs with fast localized spectral filtering. In *Advances in neural information processing systems* (pp. 3844-3852).
- Deng, L., Hinton, G., & Kingsbury, B. (2013, May). New types of deep neural network learning for speech recognition and related applications: An overview. In *2013 IEEE International Conference on Acoustics, Speech and Signal Processing* (pp. 8599-8603). IEEE.
- El Garouani, A., Mulla, D. J., El Garouani, S., & Knight, J. (2017). Analysis of urban growth and sprawl from remote sensing data: Case of Fez, Morocco. *International Journal of Sustainable Built Environment*, 6(1), 160-169.
- Elessawy, F. (2017). The boom: Population and urban growth of Dubai City. *Horizons Hum. Soc. Sci*, 2, 26-41.
- Elmahdy, S. I., & Mohamed, M. M. (2018). Monitoring and analyzing the Emirate of Dubai's land use/land cover changes: An integrated, low-cost remote sensing approach. *International Journal of Digital Earth*, 11(11), 1132-1150.



- Elsheshtawy, Y. (2019, April 17). Transforming Riyadh: A new urban paradigm? The Arab Gulf States Institute in Washington. Retrieved from <https://agsiw.org/>
- Engelen, G. (1988). The theory of self-organization and modelling complex urban systems. *European Journal of Operational Research*, 37(1), 42-57.
- Finn, C., Goodfellow, I., & Levine, S. (2016). Unsupervised learning for physical interaction through video prediction. In *Advances in neural information processing systems* (pp. 64-72).
- Folkers, A. S., & Buiten, B. (2019). *Modern architecture in Africa: Practical encounters with intricate African modernity*. Cham, Switzerland: Springer Nature.
- Fotheringham, A. S., Batty, M., and Longley, P. A. (1989, December). Diffusion-limited aggregation and the fractal nature of urban growth. In *Papers of the Regional Science Association* (Vol. 67, No. 1, pp. 55-69). Springer-Verlag.
- Frankhauser, P. (2008). Fractal geometry for measuring and modelling urban patterns. In *The dynamics of complex urban systems* (pp. 213-243). Physica-Verlag HD.
- Friedl, M. A., Brodley, C. E., & Strahler, A. H. (1999). Maximizing land cover classification accuracies produced by decision trees at continental to global scales. *IEEE Transactions on Geoscience and Remote Sensing*, 37(2), 969-977.
- Fukushima, K. (1980). Neocognitron: A self-organizing neural network model for a mechanism of pattern recognition unaffected by shift in position. *Biological cybernetics*, 36(4), 193-202.
- Gao, Y., & Mosalam, K. M. (2018). Deep transfer learning for image-based structural damage recognition. *Computer-Aided Civil and Infrastructure Engineering*, 33(9), 748-768.
- Gerasimović, M., Bugarić, U., & Božić, M. (2016). Enrollment management: Development of prediction model based on logistic regression. *FME Transactions*, 44(1), 92-98.
- Giovanis, E. (2012). Using Decision Trees for Prediction of US Economic Recessions. Available at SSRN 2186185.
- Gómez, J. A., Patiño, J. E., Duque, J. C., & Passos, S. (2020). Spatiotemporal Modeling of Urban Growth Using Machine Learning. *Remote Sensing*, 12(1), 109.
- Gouda, A. A., Hosseini, M., & Masoumi, H. E. (2016). The status of urban and suburban sprawl in Egypt and Iran. *GeoScape*, 10(1), 1-15.
- Han, Y., & Jia, H. (2017). Simulating the spatial dynamics of urban growth with an integrated modeling approach: A case study of Foshan, China. *Ecological modelling*, 353, 107-116.

- Han, Y., & Jia, H. (2017). Simulating the spatial dynamics of urban growth with an integrated modeling approach: A case study of Foshan, China. *Ecological Modelling*, 353, 107–116.
- Hansen, M. C., DeFries, R. S., Townshend, J. R., & Sohlberg, R. (2000). Global land cover classification at 1 km spatial resolution using a classification tree approach. *International journal of remote sensing*, 21(6-7), 1331-1364.
- Hashem, N., & Balakrishnan, P. (2015). Change analysis of land use/land cover and modelling urban growth in Greater Doha, Qatar. *Annals of GIS*, 21(3), 233-247.
- Hashemi, H., & Abdelghany, K. (2018). End-to-end deep learning methodology for real-time traffic network management. *Computer-Aided Civil and Infrastructure Engineering*, 33(10), 849–863.
- He, C., Okada, N., Zhang, Q., Shi, P., & Zhang, J. (2006). Modeling urban expansion scenarios by coupling cellular automata model and system dynamic model in Beijing, China. *Applied Geography*, 26(3-4), 323-345.
- He, K., Zhang, X., Ren, S., & Sun, J. (2016). Deep residual learning for image recognition. *Proceedings of the IEEE conference on computer vision and pattern recognition* (pp. 770–778). Piscataway, NJ: Institute of Electrical and Electronics Engineers Inc.
- Held, C. C., & Cummings, J. T. (2018). *Middle East Patterns, Student Economy Edition: Places, People, and Politics* (Sixth edition). Routledge.
- Hu, Z., & Lo, C. P. (2007). Modeling urban growth in Atlanta using logistic regression. *Computers, Environment and Urban Systems*, 31(6), 667-688.
- Hubel, D. H., & Wiesel, T. N. (1968). Receptive fields and functional architecture of monkey striate cortex. *The Journal of physiology*, 195(1), 215-243.
- Husodo, A. Y., Jati, G., Alfiany, N., & Jatmiko, W. (2019, August). Intruder Drone Localization Based on 2D Image and Area Expansion Principle for Supporting Military Defence System. In *2019 IEEE International Conference on Communication, Networks and Satellite (Comnetsat)* (pp. 35-40). IEEE.
- Ibrahim, M. R., Titheridge, H., Cheng, T., & Haworth, J. (2019). predictSLUMS: A new model for identifying and predicting informal settlements and slums in cities from street intersections using machine learning. *Computers, Environment and Urban Systems*, 76, 31-56.
- International Centre for Migration Policy Development (ICMPD) (2018). *City Migration Profile Amman -Executive Summary*,

[https://www.icmpd.org/fileadmin/1\\_2018/MC2CM/City\\_Migration\\_Profile\\_Aman\\_EN.pdf](https://www.icmpd.org/fileadmin/1_2018/MC2CM/City_Migration_Profile_Aman_EN.pdf): Access Date April, 2020.

- Izbassarova, A., Duisembay, A., & James, A. P. (2020). Speech Recognition Application Using Deep Learning Neural Network. In *Deep Learning Classifiers with Memristive Networks* (pp. 69-79). Springer, Cham.
- Jaad, A., & Abdelghany, K. (2020). Modeling urban growth using video prediction technology: A time-dependent convolutional encoder–decoder architecture. *Computer-Aided Civil and Infrastructure Engineering*, 35:430–447.
- Joubert, N., Reid, T. G., & Noble, F. (2020). Developments in Modern GNSS and Its Impact on Autonomous Vehicle Architectures. *arXiv preprint arXiv:2002.00339*.
- Kadhim, N., Mourshed, M., & Bray, M. (2016). Advances in remote sensing applications for urban sustainability. *Euro-Mediterranean Journal for Environmental Integration*, 1(1), 7.
- Kalchbrenner, N., van den Oord, A., Simonyan, K., Danihelka, I., Vinyals, O., Graves, A., & Kavukcuoglu, K. (2017, August). Video pixel networks. In *Proceedings of the 34th International Conference on Machine Learning-Volume 70*, 1771-1779. JMLR. org.
- Kalinin, A. A., Igloukov, V. I., Rakhlin, A., & Shvets, A. A. (2020). Medical Image Segmentation Using Deep Neural Networks with Pre-trained Encoders. In *Deep Learning Applications* (pp. 39-52). Springer, Singapore.
- Kang, D., & Cha, Y. J. (2018). Autonomous UAVs for structural health monitoring using deep learning and an ultrasonic beacon system with geo-tagging. *Computer-Aided Civil and Infrastructure Engineering*, 33(10), 885–902.
- Kang, J. H., Kim, K. W., & Kim, S. M. (2014). Development of the U-turn accident model at signalized intersections in urban areas by logistic regression analysis. *Journal of the Korean Society of Civil Engineers*, 34(4), 1279-1287.
- Karpathy, A., Toderici, G., Shetty, S., Leung, T., Sukthankar, R., & Fei-Fei, L. (2014). Large-scale video classification with convolutional neural networks. In *Proceedings of the IEEE conference on Computer Vision and Pattern Recognition* (pp. 1725-1732).
- Kaur, P., & Khosla, P. K. (2020). Artificial Intelligence Based Glaucoma Detection. In *Advancement of Machine Intelligence in Interactive Medical Image Analysis* (pp. 283-305). Springer, Singapore.

- Ke, X., Qi, L., & Zeng, C. (2016). A partitioned and asynchronous cellular automata model for urban growth simulation. *International Journal of Geographical Information Science*, 30(4), 637-659.
- Khalil, M. A., Al-Ruzouq, R., Hamad, K., & Shanableh, A. (2017). Multi-temporal satellite imagery for infrastructure growth assessment of Dubai City, UAE. In *MATEC Web of Conferences* (Vol. 120, p. 09006). EDP Sciences.
- Leao, S., Bishop, I., & Evans, D. (2004). Simulating urban growth in a developing nation's region using a cellular automata-based model. *Journal of urban planning and development*, 130(3), 145-158.
- LeCun, Y., Bengio, Y., & Hinton, G. (2015). Deep learning. *Nature*, 521(7553), 436–444.
- Li, J., Wang, C., Kang, X., & Zhao, Q. (2019). Camera localization for augmented reality and indoor positioning: A vision-based 3D feature database approach. *International Journal of Digital Earth*, 1-15.
- Li, S., Zhao, X., & Zhou, G. (2019). Automatic pixel-level multiple damage detection of concrete structure using fully convolutional network. *Computer-Aided Civil and Infrastructure Engineering*, 34(7), 616-634.
- Li, X., & Gar-On Yeh, A. (2004). Data mining of cellular automata's transition rules. *International Journal of Geographical Information Science*, 18(8), 723-744.
- Li, X., Liu, X., & Yu, L. (2014). A systematic sensitivity analysis of constrained cellular automata model for urban growth simulation based on different transition rules. *International Journal of Geographical Information Science*, 28(7), 1317-1335.
- Liang, Y., Liu, L., & Huang, J. (2020). Modeling Urban Growth with CA Model at Regional Scale. In *Integrated Modelling of Ecosystem Services and Land-Use Change* (pp. 19-38). Springer, Singapore.
- Liberati, A., Altman, D. G., Tetzlaff, J., Mulrow, C., Gøtzsche, P. C., Ioannidis, J. P., ... & Moher, D. (2009). The PRISMA statement for reporting systematic reviews and meta-analyses of studies that evaluate health care interventions: explanation and elaboration. *PLoS medicine*, 6(7), e1000100.
- Lin, Y. P., Chu, H. J., Wu, C. F., & Verburg, P. H. (2011). Predictive ability of logistic regression, auto-logistic regression and neural network models in empirical land-use change modeling—a case study. *International Journal of Geographical Information Science*, 25(1), 65-87.
- Lintas, A., Rovetta, S., Verschure, P. F., and Villa, A. E. (2017). Artificial neural networks and machine learning - ICANN 2017: 26th International Conference on Artificial

- Neural Networks, Alghero, Italy, September 11-14, 2017, proceedings. Cham, Switzerland: Springer.
- Liu, W., & Seto, K. C. (2008). Using the ART-MMAP neural network to model and predict urban growth: a spatiotemporal data mining approach. *Environment and Planning B: Planning and Design*, 35(2), 296-317.
- Liu, Z., Yeh, R. A., Tang, X., Liu, Y., & Agarwala, A. (2017). Video frame synthesis using deep voxel flow. In *Proceedings of the IEEE International Conference on Computer Vision* (pp. 4463-4471).
- Loewert, P., & Steiner, C. (2019). The New Administrative Capital in Egypt: The Political Economy of the Production of Urban Spaces in Cairo. *Middle East-Topics & Arguments*, 12, 66-75.
- Longley, P. A., & Mesev, V. (2000). On the measurement and generalisation of urban form. *Environment and Planning A*, 32(3), 473-488.
- Lubell, M., Feiock, R. C., & De La Cruz, E. E. R. (2009). Local institutions and the politics of urban growth. *American Journal of Political Science*, 53(3), 649-665.
- Maeda, H., Sekimoto, Y., Seto, T., Kashiwama, T., & Omata, H. (2018). Road damage detection and classification using deep neural networks with smartphone images. *Computer-Aided Civil and Infrastructure Engineering*, 33, 1127–1141.
- Makido, Y., Shandas, V., & Ferwati, S. (2020). Predicting urban growth. In *Urban Adaptation to Climate Change* (pp. 75-92). Springer, Cham.
- Mallouk, A., Elhadrahi, H., Malaainine, M. E. I., Rhinane, H., & des Travaux Publics, E. H. (2019). Using the SLEUTH urban growth model coupled with a GIS to simulate and predict the future urban expansion of Casablanca region, Morocco. *International Archives of the Photogrammetry, Remote Sensing and Spatial Information Sciences*, 42(4/W12).
- Mandelbrot, B. B. (1983). *The fractal geometry of nature* (Vol. 173, p. 51). New York: WH freeman.
- Mansour, S., Al-Belushi, M., & Al-Awadhi, T. (2020). Monitoring land use and land cover changes in the mountainous cities of Oman using GIS and CA-Markov modeling techniques. *Land Use Policy*, 91, 104414.
- Masek, J. G., Lindsay, F. E., & Goward, S. N. (2000). Dynamics of urban growth in the Washington DC metropolitan area, 1973-1996, from Landsat observations. *International Journal of Remote Sensing*, 21(18), 3473-3486.

- Masi, I., Trần, A. T., Hassner, T., Leksut, J. T., & Medioni, G. (2016, October). Do we really need to collect millions of faces for effective face recognition?. In *European Conference on Computer Vision* (pp. 579-596). Springer, Cham.
- Michalski, V., Memisevic, R., & Konda, K. (2014). Modeling deep temporal dependencies with recurrent grammar cells". In *Advances in neural information processing systems* (pp. 1925-1933).
- Midekisa, A., Holl, F., Savory, D. J., Andrade-Pacheco, R., Gething, P. W., Bennett, A., & Sturrock, H. J. (2017). Mapping land cover change over continental Africa using Landsat and Google Earth Engine cloud computing. *PloS One*, 12(9).
- Molina-Cabello, M. A., Luque-Baena, R. M., López-Rubio, E., & Thurnhofer-Hemsi, K. (2018). Vehicle type detection by ensembles of convolutional neural networks operating on super resolved images. *Integrated Computer-Aided Engineering*, 25(4), 321–333.
- Mustafa, A., Cools, M., Saadi, I., & Teller, J. (2017). Coupling agentbased, cellular automata and logistic regression into a hybrid urban expansion model (HUEM). *Land Use Policy*, 69, 529–540.
- Myint, S. W. (2003). Fractal approaches in texture analysis and classification of remotely sensed data: Comparisons with spatial autocorrelation techniques and simple descriptive statistics. *International Journal of Remote Sensing*, 24(9), 1925-1947.
- Nabian, M. A., & Meidani, H. (2018). Deep learning for accelerated reliability analysis of transportation networks. *Computer-Aided Civil and Infrastructure Engineering*, 33(6), 459–480.
- Oh, J., Guo, X., Lee, H., Lewis, R. L., & Singh, S. (2015). Action-conditional video prediction using deep networks in atari games. In *Advances in neural information processing systems* (pp. 2863-2871).
- Osman, T., Divigalpitiya, P., & Arima, T. (2016). Using the SLEUTH urban growth model to simulate the impacts of future policy scenarios on land use in the Giza Governorate, Greater Cairo metropolitan region. *International Journal of Urban Sciences*, 20(3), 407-426.
- Osman, T., Shaw, D., & Kenawy, E. (2019). An integrated land-use change model to simulate and predict the future of greater Cairo metropolitan region. *Journal of Land Use Science*, 13(6), 565-584.
- Patraucean, V., Handa, A., & Cipolla, R. (2015). Spatio-temporal video autoencoder with differentiable memory. *arXiv preprint arXiv:1511.06309*.

- Pelánek, R. (2015). Metrics for evaluation of student models. *Journal of Educational Data Mining*, 7(2), 1-19.
- Pijanowski, B. C., Brown, D. G., Shellito, B. A., & Manik, G. A. (2002). Using neural networks and GIS to forecast land use changes: a land transformation model. *Computers, environment and urban systems*, 26(6), 553-575.
- Pijanowski, B. C., Pithadia, S., Shellito, B. A., & Alexandridis, K. (2005). Calibrating a neural network-based urban change model for two metropolitan areas of the Upper Midwest of the United States. *International Journal of Geographical Information Science*, 19(2), 197-215.
- Pintea, S. L., van Gemert, J. C., & Smeulders, A. W. (2014, September). Déjà vu. In *European Conference on Computer Vision* (pp. 172-187). Springer, Cham.
- Plecher, H. (2019). International. Retrieved from <https://www.statista.com/markets/422/international/>
- Pratt, L. Y. (1993). Discriminability-based transfer between neural networks. In *Advances in neural information processing systems* (pp. 204-211).
- Qiu, S., Liu, Q., Zhou, S., & Wu, C. (2019). Review of artificial intelligence adversarial attack and defense technologies. *Applied Sciences*, 9(5), 909.
- Rafiei, M. H., & Adeli, H. (2017). A novel machine learning-based algorithm to detect damage in high-rise building structures. *The Structural Design of Tall and Special Buildings*, 26(18), e1400.
- Rafiei, M. H., & Adeli, H. (2018). A novel unsupervised deep learning model for global and local health condition assessment of structures. *Engineering Structures*, 156, 598-607.
- Rafiei, M. H., Khushefati, W. H., Demirboga, R., & Adeli, H. (2017). Supervised deep restricted Boltzmann machine for estimation of concrete. *ACI Materials Journal*, 114(2), 237–244.
- Renieblas, G. P., Nogués, A. T., González, A. M., León, N. G., & del Castillo, E. G. (2017). Structural similarity index family for image quality assessment in radiological images. *Journal of Medical Imaging*, 4(3), 035501.
- Robaa, S. M. (2003). Urban-suburban/rural differences over Greater Cairo, Egypt. *Atmósfera*, 16(3), 157-171.
- Roy, P. K., Singh, J. P., & Banerjee, S. (2020). Deep learning to filter SMS Spam. *Future Generation Computer Systems*, 102, 524-533.

- Saadani, S., Laajaj, R., Maanan, M., Rhinane, H., & Aaroud, A. (2020). Simulating spatial-temporal urban growth of a Moroccan metropolitan using CA–Markov model. *Spatial Information Research*, 1-13.
- Sanders, L., Pumain, D., Mathian, H., Guérin-Pace, F., and Bura, S. (1997). SIMPOP: a multiagent system for the study of urbanism. *Environment and Planning B: Planning and design*, 24(2), 287-305.
- Schmidhuber, J. (2015). Deep learning in neural networks: An overview. *Neural Networks*, 61, 85–117.
- Schneider, A., Friedl, M. A., McIver, D. K., & Woodcock, C. E. (2003). Mapping urban areas by fusing multiple sources of coarse resolution remotely sensed data. *Photogrammetric Engineering & Remote Sensing*, 69(12), 1377-1386.
- Shafizadeh-Moghadam, H., Asghari, A., Tayyebi, A., & Taleai, M. (2017). Coupling machine learning, tree-based and statistical models with cellular automata to simulate urban growth. *Computers, Environment and Urban Systems*, 64, 297-308.
- Shandas, V., Makido, Y., & Ferwati, S. (2017). Rapid urban growth and land use patterns in Doha, Qatar: Opportunities for sustainability? *European Journal of Sustainable Development Research*, 1(11), 1-14. doi: 10.20897/ejosdr.201711.
- Shanmugamani, R. (2018). *Deep Learning for Computer Vision: Expert techniques to train advanced neural networks using TensorFlow and Keras*. Packt Publishing Ltd.
- Shen, J., Xiong, X., Xue, Z., & Bian, Y. (2019). A convolutional neural-network-based pedestrian counting model for various crowded scenes. *Computer-Aided Civil and Infrastructure Engineering*.
- Simonyan, K., & Zisserman, A. (2014). Two-stream convolutional networks for action recognition in videos. In *Advances in neural information processing systems*, pp. 568-576.
- Sohn, K., Lee, H., & Yan, X. (2015). Learning structured output representation using deep conditional generative models. In *Advances in neural information processing systems*, 3483-3491.
- Srivastava, N., Mansimov, E., & Salakhudinov, R. (2015, June). Unsupervised learning of video representations using lstms. In *International conference on machine learning*, 843-852.
- Stallkamp, J., Schlipsing, M., Salmen, J., and Igel, C. (2012). Man vs. computer: Benchmarking machine learning algorithms for traffic sign recognition. *Neural networks*, 32, 323-332.



- Stanilov, K., & Batty, M. (2011). Exploring the historical determinants of urban growth patterns through cellular automata. *Transactions in GIS*, 15(3), 253-271.
- Statista Research Department. (2020, March 9). MENA: total population 2100. Retrieved from <https://www.statista.com/statistics/978535/mena-total-population/#statisticContainer>.
- Stokes, J. M., Yang, K., Swanson, K., Jin, W., Cubillos-Ruiz, A., Donghia, N. M., ... & Tran, V. M. (2020). A deep learning approach to antibiotic discovery. *Cell*, 180(4), 688-702.
- Tatarchenko, M., Dosovitskiy, A., & Brox, T. (2016, October). Multi-view 3d models from single images with a convolutional network. In *European Conference on Computer Vision* (pp. 322-337). Springer, Cham.
- Tayyebi, A. H., Tayyebi, A., & Khanna, N. (2014). Assessing uncertainty dimensions in land-use change models: using swap and multiplicative error models for injecting attribute and positional errors in spatial data. *International journal of remote sensing*, 35(1), 149-170.
- Tayyebi, A., & Pijanowski, B. C. (2014). Modeling multiple land use changes using ANN, CART and MARS: Comparing tradeoffs in goodness of fit and explanatory power of data mining tools. *International Journal of Applied Earth Observation and Geoinformation*, 28, 102-116.
- Tayyebi, A., Pijanowski, B. C., & Tayyebi, A. H. (2011). An urban growth boundary model using neural networks, GIS and radial parameterization: An application to Tehran, Iran. *Landscape and Urban Planning*, 100(1-2), 35-44.
- Thakurdesai, H. M., & Aghav, J. V. (2020). Computer Vision Based Position and Speed Estimation for Accident Avoidance in Driverless Cars. In *ICT Systems and Sustainability* (pp. 435-443). Springer, Singapore.
- Thapa, R., & Murayama, Y. (2009). Examining spatiotemporal urbanization patterns in Kathmandu Valley, Nepal: Remote sensing and spatial metrics approaches. *Remote Sensing*, 1(3), 534-556.
- The G-LUM Model. (2009). Predicting future spatial distributions of employment and households. Retrieved from [http://www.ce.utexas.edu/prof/kockelman/G-LUM\\_Website/homepage.htm](http://www.ce.utexas.edu/prof/kockelman/G-LUM_Website/homepage.htm).
- The UPLAN Model and Data. (2001). A detailed description of the UPLAN model. Retrieved from <http://www.des.ucdavis.edu/faculty/johnston/pub7.htm>.

- Tooke, T. R., Coops, N. C., Goodwin, N. R., & Voogt, J. A. (2009). Extracting urban vegetation characteristics using spectral mixture analysis and decision tree classifications. *Remote Sensing of Environment*, 113(2), 398-407.
- Torres, J. F., Galicia, A., Troncoso, A., & Martínez-Álvarez, F. (2018). A scalable approach based on deep learning for big data time series forecasting. *Integrated Computer-Aided Engineering*, 25(4), 335–348.
- Torrey, L., & Shavlik, J. (2010). Transfer learning. In *Handbook of Research on Machine Learning Applications and Trends: Algorithms, Methods, and Techniques* (pp. 242-264). IGI Global.
- Tran, D., Ray, J., Shou, Z., Chang, S. F., & Paluri, M. (2017). Convnet architecture search for spatiotemporal feature learning. arXiv preprint arXiv:1708.05038.
- Triantakou, D., & Mountrakis, G. (2012). Urban growth prediction: A review of computational models and human perceptions. *Journal of Geographic Information System*, 4(6), 555–587.
- U.S. Geological Survey. (2020, April 8). Landsat-Earth Observation Satellites. Retrieved from <https://pubs.er.usgs.gov/publication/fs20153081>
- Ulrichsen, K. C. (2016). *The United Arab Emirates: power, politics and policy making*. Taylor & Francis.
- US Census Bureau. (2018). Dallas-Fort Worth-Arlington Has Largest Growth in the U.S. Retrieved from <https://www.census.gov/newsroom/press-releases/2018/popest-metro-county.html>
- Van Amersfoort, J., Kannan, A., Ranzato, M. A., Szlam, A., Tran, D., and Chintala, S. (2017). Transformation-based models of video sequences. arXiv preprint arXiv:1701.08435.
- Van Vliet, J., White, R., & Dragicevic, S. (2009). Modeling urban growth using a variable grid cellular automaton. *Computers, Environment and Urban Systems*, 33(1), 35-43.
- Verbeek, W. (2017). *Estimating the impacts of urban growth on future flood risk: A comparative study*. CRC Press.
- Victor Ge. “A Survey on Deep Video Prediction”. In: *learning* 59, 68-75.
- Vondrick, C., Pirsiavash, H., & Torralba, A. (2016). Generating videos with scene dynamics. In *Advances In Neural Information Processing Systems* (pp. 613-621).
- Vukotić, V., Pintea, S. L., Raymond, C., Gravier, G., & van Gemert, J. C. (2017). One-step time-dependent future video frame prediction with a convolutional encoder-

- decoder neural network. In *International Conference on Image Analysis and Processing* (pp. 140-151). Springer, Cham.
- Waddell, P. (2002). UrbanSim: Modeling urban development for land use, transportation, and environmental planning. *Journal of the American planning association*, 68(3), 297-314.
- Walker, J., Doersch, C., Gupta, A., & Hebert, M. (2016, October). An uncertain future: Forecasting from static images using variational autoencoders. In *European Conference on Computer Vision* (pp. 835-851). Springer, Cham.
- Wang, C., Dai, Y., Zhou, W., & Geng, Y. (2020). A Vision-Based Video Crash Detection Framework for Mixed Traffic Flow Environment Considering Low-Visibility Condition. *Journal of Advanced Transportation*, 2020.
- Wang, P., & Bai, X. (2018). Regional parallel structure based CNN for thermal infrared face identification. *Integrated Computer-Aided Engineering*, 25(3), 247-260.
- Wang, Z., & Bovik, A. C. (2009). Mean squared error: Love it or leave it? A new look at signal fidelity measures. *IEEE signal processing magazine*, 26(1), 98-117.
- Wang, Z., Bovik, A. C., Sheik, H. R., & Simoncelli, E. P. (2004). Image quality assessment: From error visibility to structural similarity. *IEEE Transactions on Image Processing*, 13(4), 1-14.
- Watter, M., Springenberg, J., Boedeker, J., and Riedmiller, M. (2015). Embed to control: A locally linear latent dynamics model for control from raw images. In *Advances in neural information processing systems* (pp. 2746-2754).
- Weng, Q. (2002). Land use change analysis in the Zhujiang Delta of China using satellite remote sensing, GIS and stochastic modelling. *Journal of environmental management*, 64(3), 273-284.
- Witten Jr, T. A., & Sander, L. M. (1981). Diffusion-limited aggregation, a kinetic critical phenomenon. *Physical review letters*, 47(19), 1400.
- Woodworth, R. S., & Thorndike, E. L. (1901). The influence of improvement in one mental function upon the efficiency of other functions.(I). *Psychological review*, 8(3), 247.
- Wu, F., & Webster, C. J. (1998). Simulation of land development through the integration of cellular automata and multicriteria evaluation. *Environment and Planning B: Planning and design*, 25(1), 103-126.
- Wu, J. (2014). Urban ecology and sustainability: The state-of-the-science and future directions. *Landscape and Urban Planning*, 125, 209-221.

- Xia, C., Zhang, A., Wang, H., & Yeh, A. G. (2019). Predicting the expansion of urban boundary using space syntax and multivariate regression model. *Habitat International*, 86, 126-134.
- Xue, T., Wu, J., Bouman, K., & Freeman, B. (2016). Visual dynamics: Probabilistic future frame synthesis via cross convolutional networks. In *Advances in neural information processing systems*, 91-99.
- Xue, Y. D., & Li, Y. C. (2018). A fast detection method via region-based fully convolutional neural networks for shield tunnel lining defects. *Computer-Aided Civil and Infrastructure Engineering*, 33(8), 638654.
- Yan, X., Yang, J., Sohn, K., & Lee, H. (2016). Attribute2image: Conditional image generation from visual attributes. In *European Conference on Computer Vision* (pp. 776-791). Springer, Cham.
- Yang, X., Li, H., Yu, Y., Luo, X., Huang, T., & Yang, X. (2018). Automatic pixel-level crack detection and measurement using fully convolutional network. *Computer-Aided Civil and Infrastructure Engineering*, 33(12), 1090–1109.
- Yang, Y., Zhou, X., & Wu, B. (2011). Urban expansion prediction for Zhangzhou city based on GIS and spatiotemporal logistic regression model. *Journal of Geo-Information Science*, 13(3), 374-382.
- Ye, X. W., Jin, T., & Ang, P. P. (2020). Computer Vision-Based Monitoring of Ship Navigation for Bridge Collision Risk Assessment. In *Machine Vision and Navigation* (pp. 787-807). Springer, Cham.
- Zafar, I., Tzanidou, G., and Burton, R. (2018). *Hands-on convolutional neural networks with TensorFlow: Solve computer vision problems with modeling in TensorFlow and Python*. Birmingham, UK: PACKT Publishing Limited.
- Zaina, S., Zaina, S., & Furlan, R. (2016). Urban planning in Qatar: strategies and vision for the development of transit villages in Doha. *Australian Planner*, 1-18. doi: 10.1080/07293682.2016.1259245
- Zhang, H., Zeng, Y., Bian, L., and Yu, X. (2010). Modelling urban expansion using a multi agent-based model in the city of Changsha. *Journal of Geographical Sciences*, 20(4), 540-556.
- Zhang, W., & Goh, A. T. (2016). Multivariate adaptive regression splines and neural network models for prediction of pile drivability. *Geoscience Frontiers*, 7(1), 45–52.

- Zhang, X., Waller, S. T., & Jiang, P. (2019). An ensemble machine learning-based modeling framework for analysis of traffic crash frequency. *Computer-Aided Civil and Infrastructure Engineering*. <https://doi.org/10.1111/mice.12485>.
- Zhavoronkov, A., Aladinskiy, V., Zhebrak, A., Zagribelnyy, B., Terentiev, V., Bezrukov, D. S., ... & Yan, Y. (2020). Potential COVID-2019 3C-like protease inhibitors designed using generative deep learning approaches. *Insilico Medicine Hong Kong Ltd A*, 307, E1.
- Zhou, S. K., Greenspan, H., and Shen, D. (2017). *Deep learning for medical image analysis*. London: Academic Press.
- Zhou, X., & Chen, H. (2018). Impact of urbanization-related land use land cover changes and urban morphology changes on the urban heat island phenomenon. *Science of the Total Environment*, 635, 1467-1476.